Diffusion of fluorescent molecules in micro- and nanostructured environments

DISSERTATION

zur Erlangung des akademischen Grades
doctor rerum naturalium
(Dr. rer. nat.)
im Fach Physik

eingereicht am
Fachbereich Physik der
Universität Dortmund
im Juni 2007

von
Herrn Dipl.-Phys. Thorsten Pieper
geboren am 20.7.1975 in Münster

Gutachter:

1. Professor Dr. Dieter Suter
2. Dr. Harald P. Mathis

Zusammenfassung

Thema der Arbeit ist die experimentelle Untersuchung von molekularer Diffusion in flüssigen Umgebungen. Die Untersuchung von diffundierenden Molekülen liefert Informationen über die Moleküle selbst, als auch über die Struktur des umgebenden Mediums. Diese Arbeit befasst sich mit Diffusionsphänomenen auf Größenskalen unterhalb von $100\,\mu\mathrm{m}$. Die flüssige Phase besteht aus Wasser oder binären Wasser/Tensid-Mischungen. Die Mikrostrukturen sind Flüssigkeitskanäle, die in Rohlinge aus kristallinem Silizium geätzt werden. In diesen Kanälen wird die diffusionsbeschränkte Durchmischung an einer Flüssigkeitsgrenzfläche untersucht. Diese Experimente fanden im stationären Fluss statt. Umgebungen in der Größenordnung von Nanometern werden aus Wasser/Tensid-Mischungen hergestellt, die aufgrund von Selbstorganisation supramolekulare Ordnungen ausbilden. Von den möglichen Ordnungen werden speziell die mizellare Phase und die lamellare Phase untersucht. Der Einfluss von Cholesterin auf die Mobilität von Fluoreszenzmolekülen in der lamellaren Phase steht im Mittelpunkt des Interesses. Als experimentelle Methode wird in erster Linie die Fluoreszenzkorrelationsspektroskopie (FCS) eingesetzt. Desweiteren werden Grundlagen zur Verfolgung von Molekülen gelegt, indem Videoaufnahmen von Fluoreszenzpartikeln ausgewertet werden. In dieser Arbeit werden tiefergehende Erkenntnisse in die Natur der Brownschen Bewegung in nahezu idealen Systemen erarbeitet. Aus den Experimenten lassen sich Schlussfolgerungen für Untersuchungen in natürlichen Umgebungen ziehen, wie sie zum Beispiel in eukaryotischen Zellen vorliegen.

Abstract

The thesis deals with phenomena of molecular diffusion in liquid environments. The examination of diffusing molecules provides information about the molecules themselves, and also about the structure of the surrounding media. This work deals with diffusion phenomena on length scales below $100\,\mu\mathrm{m}$. The liquid phase consists of water or water/surfactant emulsions. The microstructures are fluidic channels etched in wafers of crystalline silicon. In these channels, diffusion-limited mixing at a liquid boundary is examined. These experiments took place in a stationary liquid flow. Environments on the nanoscale are made of binary liquids forming supramolecular orders by self-assembly. From these structures, the micellar and the lamellar structure are examined in particular. The focus is on the influence of cholesterol on the mobility of probe molecules in the lamellar phase. The main experimental method is Fluorescence Correlation Spectroscopy (FCS). Additionally, fundamentals for the tracking of single molecules are established by analyzing video recordings of fluorescing particles. The thesis provides advanced insight into the nature of molecular motion in nearly ideal systems. Further conclusions for investigations in natural environments, as they exist in eukaryotic cells, can be drawn from the experiments.

Contents

List of Figures

Acknowledgments

The main part of this work was done in the *Fraunhofer* BioMOS research group in Sankt Augustin. As my scientific advisor, I especially thank Dr. Harald P. Mathis for his continuous mentoring. He introduced me into a new and interesting field and contributed greatly to successful collaborations with other institutions.

Special thanks goes to Professor Dieter Suter from the University of Dortmund who supervised the progress of my work during three years. The chapter about bilayer systems is based on his idea. I thank him for giving me the chance to present my results in several seminars and on conferences. From the same group, I thank Svetlana Markova for her engagement in our common project.

I express my gratitude towards Professor Masataka Kinjo from the Hokkaido University for his generous invitation to his laboratory. I am grateful that I was allowed to gain insight into research and life in Japan. The time in Sapporo was highly instructional for me. From the laboratory, I especially thank Dr. Goro Nishimura who gave me important advice for the experiments with microemulsions. For all situations when life became difficult I thank Yu Ohsugi who has become a good friend. He, and all other lab members, have left constant memories. I look back with joy and hope to meet you again in the future. For the financial support, I thank the Japan Society for the Promotion of Science (grant PE05567).

I also thank Professor Günter Wagner for his supervision of our students and his insights into microengineering. He always kept clear sight even in times of trouble.

Dr. Jörg Ackermann was and still is helping with difficult theoretical questions. He had a main part in developing the computer simulation.

From Dr. Thomas Kirner I received good advice about how to improve microfluidic devices.

The CFD simulations were carried out in close cooperation with Dr. Barbara Steckel at *Fraunhofer SCAI*. I thank Dipl.-Math. Andrea Wagner for her support in questions of hydrodynamics. She modeled the simulation grid and managed the computations using the FLUENT software package.

Benjamin Greiner is my friend. All questions concerning our common work were discussed with him in a close and trustful atmosphere. I also thank him for proofreading.

The following students contributed to this work with all their time and energy. Volker Inden characterized the nanopositioning unit. Kai Lueghausen did a great job in setting up the real time image processing devices. Embarek Belhadj constructed a temperature control unit with high

precision. Christian Müller offered his help and experience for the experiments with enzymatic reactions.
Erwin Rambow is the number one person to ask when electrical and mechanical setups have to be realized quickly.
I would also like to thank some former members of the BioMOS group. These are Dipl.-Ing. Martina Jünger and Dipl.-Ing. Thomas Palutke who were responsible for fabricating the microfluidic devices.
Last not least, I thank Dr. Antonia Delago for her encouragement and proofreading.

Introduction

To date the principles of molecular organization during the life cycle of a cell are widely unknown. Understanding cellular mechanisms contributes to the development of new drugs as well as medical devices for diagnosis and therapy. Recent progress in microscope technology now enables us to access critical questions concerning these applications. Particularly fluorescence methods have developed quickly and have become an important tool for visualizing processes in cells. This has also influenced some related fields, such as Biophysics, Microengineering, and Material science. Present activities aim at improving the optical resolution, and extending the information yield from measurements [1, 2, 3].

While physics has succeeded in describing observations on the macroscopic and on the atomistic level, intermediate systems represent still a borderline between microscopic and nanoscopic world. Because of the large number of molecules involved, new approaches are necessary to describe the observed phenomena adequately.

Biological cells combine a vast number of functional molecules, structures and interaction processes. For a principle understanding of cellular functions, it is thus useful to simplify the regarded system. This can be achieved by transferring the system of interest to an in vitro environment. In vitro experiments are essential to reduce the complexity and the number of unknown parameters. Many biomedical applications require the implementation of biochemical assays in small devices. For diagnostic applications, for example, in vitro assays are usually the preferred choice. They can be standardized easily, so that the time for each test can be minimized. Moreover, practical reasons demand devices that are hygienic, disposable, and small. Because the majority of applications is based on testing human body fluids (blood, urine, sweat, etc.), there are often liquid specimen involved. For certain purposes, e. g. for blood examinations, it is also desirable that these devices work continuously. This is one reason, why it is necessary to design continuous flow reaction chambers.

The handling of liquids on the micrometer scale gives rise to many unsolved problems. The current work focuses on certain issues dealing with molecular diffusion in artificial environments. These environments include silicon based microchannels and lipid/water microemulsions showing supramolecular order. These structures have length scales reaching from $100\,\mu\mathrm{m}$ down to the

nanometer range. The transition from the micrometer to the nanometer scale is interesting in so far as fundamental changes in the diffusion behavior can be observed.
The first objective of this thesis is to characterize a particular microfluidic channel geometry in its laminar flow behavior. As a next step, the properties of the channel for diffusive mixing are examined using fluorescent molecules in very low concentrations. Numerical simulations and experiments using Fluorescence Correlation Spectroscopy (FCS) as the method of analysis are combined to give a detailed description of the mixing device. The channels are test environments for realizing enzymatic reactions inside microfluidic channels. The necessity for continuous flow systems in assay technology has been noted by a number of researchers [4].
FCS is a microscopy method basically used to determine low concentrations and diffusion coefficients. In its simplest form, FCS does not provide image resolution.
A different set of experiment was performed using a newly developed image detection microscope. By analyzing images of fluorescing particles, it is shown, how specific information about a single particle can be extracted from such images. The experiment and instrument setup are part of a bigger project on a new fluorescence detection system for tracking single molecule motion. By characterizing the optical properties of the system, first steps towards Single Molecule Detection (SMD) are undertaken successfully.
As a second objective, diffusion in lamellar bilayers is studied using a surfactant/water model system, which exhibits some fundamental properties of biological membranes. These systems show characteristic features of nanostructured environments. Again, FCS was used as the method of choice. A computer simulation, which is developed in chapter 2, is applied for testing a new FCS model used to describe the measurement data. The experiments were carried out entirely in vitro. No biological cells were examined.
The thesis is structured as follows: Chapter 1 gives a short overview about the mathematical background of diffusion and fluorescence. Chapter 2 explaines the development of the computer simulation for FCS. In chapter 3, the techniqual equipment which was used for the experiments is described. Three different microscope setups were used. In chapter 4, experimental measurements in microfluidic channels are presented. The results are analyzed and interpreted for the desired application. In the second part, the trajectory of a single fluorescing particle is recorded and analyzed. Chapter 5 is a separate study dealing with diffusion in model membranes. The simulation from chapter 2 is applied to evaluate a new model equation for FCS. In the conclusion (chapter 6), the results are reviewed and evaluated in the present context of research. Possible consequences for investigating diffusion in natural environments are given.

Chapter 1

Diffusion and fluorescence

Molecular motion is often based on stochastic behavior [5]. The observation that thermal fluctuations in liquids exist, were first described by Brown in 1827 [6]. He discovered the effect in a light microscope when he saw a characteristic tremor on swimming pollen. Hence, this phenomenon is generally referred to as Brownian motion.
In this chapter, the microscopic description of molecular motion is outlined in section 1.1. The general concept of Brownian motion is valid for liquids, gas phases, and also solids. Here, only the liquid phase is of importance. In the presented stochastic theory, the molecules in a solution are represented by discrete objects on an imaginary lattice. Transition probabilites between the lattice sites are defined according to the mobility properties of the molecules. The observed macroscopic phenomena can be derived from the microscopic theory. The time course of a concentration gradient of a dissolved substance is described by Fick's laws. They are discussed in section 1.1.3. With respect to the conducted experiments, the special case of diffusion in a confined vessel is pointed out.
Light emission due to fluorescence is the essential attribute to make the visual observation of molecules possible. The term fluorescence, which subsumes the physical effects of electronic excitation and photon emission, is explained in section 1.2. The three-state model of electronic states in a fluorescent molecule is cited. It allows to give a relation between the local excitation intensity and the photon emission rate of a single molecule.
As the main experimental technique, the principle of confocal microscopy is illustrated in section 1.3. In confocal microscopy, a beam of laser light is focused into the liquid specimen. The size of the observation volume is given by the diffraction limited spot of the incident light. The fluorescence intensity trace as the outcome of a confocal fluorescence experiment is utilized. There are different ways to analyze the intensity traces and extract relevant information from it. Here, Fluorescence Correlation Spectroscopy (FCS) is mainly used throughout chapters 2-5. Important equations for analyzing the correlation curves are derived from basic assumptions.

For small observation volumes, as they appear in FCS, the local fluctuations of the solute molecules become significant. It is therefore suggestive to begin with the definition of the concentration of a substance in solution.

1.1 Molecular motion in liquids

The fluid state of aggregation is characterized by the fact, that the force driven by thermal energy is almost equal to the intermolecular forces which can be described by the Lennard-Jones potential. In contrast to the solid state, the molecules are able to exchange their position with their neighbors. During a melting transition from solid to liquid state, the density is usually slightly reduced. Water is a well-known exception from this rule. A correct description of liquids requires a combined approach of classical and quantum mechanical physics [7]. Gases and liquids can be regarded as continuous media in many experiments. This means, on macroscopic length scales all properties like density, pressure or velocity can be treated as continuous variables. These quantities are a result from averaging over a large ensemble of particles [8]. But, because matter consists of molecules and atoms, a lower limit for the continuum assumption exists. The smaller the observed structures are, the higher the natural fluctuations of macroscopically defined quantities become. For the mathematical treatment of diffusion the microscopic and the macroscopic description are distinguished.

1.1.1 Concentration fluctuations

The concentration C of a substance in a volume (of a gas or solvent) is defined by the ratio of the total particle number N_{total} and the total volume V_{total}

$$C = \frac{N_{total}}{V_{total}} \tag{1.1}$$

Usually, the true concentration C is not determined by counting all particles in the total volume, but by measuring the average number of particles N in a smaller subvolume V. Implicitly, it is assumed that this concentration $\tilde{C}$ is equal in each subvolume, which is equivalent to $\tilde{C} = C$. This is true, if the system is in equilibrium, and the subvolume still contains a number of particles $n \gg 1$. When going to very small subvolumes, this assumption is not valid anymore. Due to spatial fluctuations, statistical fluctuations arise (Fig. 1-1). The distribution of the real particle number N in different subvolumes V then follows a Poissonian distribution with a parameter $\mu = N$, which is equal to the average number of particles [9]

$$P(n \mid \mu = N) = \frac{N^n}{n!} e^{-N}. \tag{1.2}$$

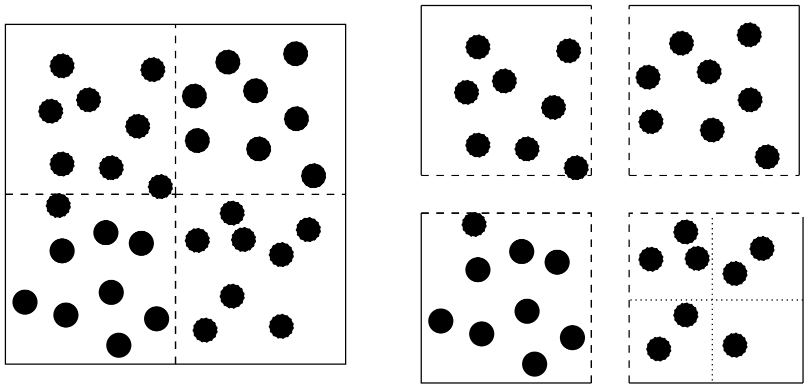

Figure 1-1. *Illustration of the difference between macroscopic concentration and local concentration. While there are almost equal numbers of particles in the four squares of side length $L/2$, in those with length $L/4$ fluctuations become evident.*

If the number of particles is represented by a random variable X, the fluctuations are given by the variance $Var(X)$ of X. Poisson distributions are characterized by the fact that the variance is equal to the mean number of particles

$$\mathrm{Var}(X) \;=\; N. \tag{1.3}$$

The relative fluctuation of a number counting experiment is given by

$$\frac{\Delta N}{N} \;=\; \frac{\sqrt{\mathrm{Var}(X)}}{N} \;=\; \frac{1}{\sqrt{N}}. \tag{1.4}$$

In Fig. 1-2 three Poisson distributions with different parameters are shown.

Remarks

The Poisson distribution becomes a Gaussian distribution for large N according to the central limit theorem (see e. g., [10]).

Concentrations are given in units of 1 mol. The molar concentration c is the number of particles expressed by multiples of Avogadro's number N_A

$$c \;=\; \frac{N}{V\,N_A}. \tag{1.5}$$

The determination of a concentration requires that a number of molecules is related to a volume. If the volume is small, the measurement error is governed by the statistical number fluctuation. To reach a relative error of $10\,\%$ in the concentration measurement an average of 100 molecules must be present in the volume. A higher precision can be reached when the measurement is extended

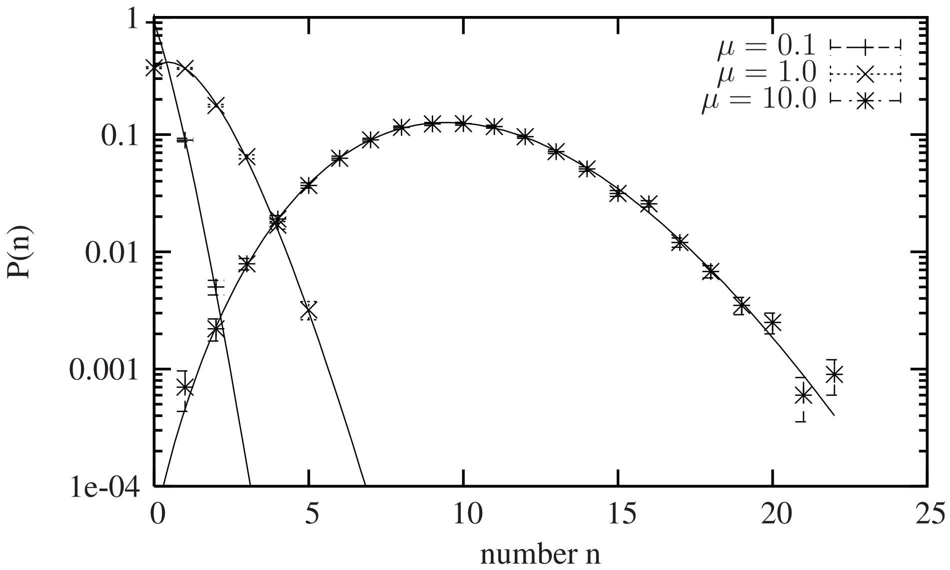

Figure 1-2. *Simulated Poissonian distributions of particles in 10^4 subvolumes. Uniform distributions of 10^3, 10^4 and 10^5 particles in the total volume underly the data points. The theoretical functions (solid lines) result from Eq. 1.2, with the factorial being replaced by the gamma function $\Gamma(n)$. μ is the average number of particles in a subvolume.*

over time. Then, temporal fluctuations (e. g., due to Brownian motion) contribute to an increased precision. This principle is availed in Fluorescence Correlation Spectroscopy.

1.1.2 Diffusion and Brownian motion

In correlation spectroscopy, the fluctuations in a small observation volume are utilized to determine the concentration and the diffusion coefficient. When resting particles are observed over a period of time, number fluctuations do not exist. Particle motion, on the other hand, leads to a varying particle number inside the observation volume and in the adjacent volumes. This fluctuation implicates a temporal and spatial correlation of the particle number. The correlation time is the characteristic resident time for a particle inside the observation volume. If the number of particles is determined in time intervals much larger than the correlation time, then the measurements are uncorrelated and statistically independent.

The term *diffusion* is ambigious. It is used for the microscopic process of Brownian motion, and also for the way to equilibrium in a concentration gradient. In the first case, the microscopic motion is meant. The second case implies the macroscopic consequences of the stochastic molecular motion. It is often visualized as a vessel of two different substances which are separated by a wall (Fig. 1-3). After removing the wall, the system tends to equalize the concentration gradient. This effect can be traced back to the molecular Brownian motion. When pollen, smaller particles, or molecules frequently collide momentum is transferred between them. This leads to a change in direction of motion which stays linear until the following collision. The frequency of collisions can be calculated from the mean free pathlength $\bar{\lambda}$ of the molecules and their average velocity $\bar{v}$ [11]

$$f_{coll} = \frac{\bar{v}}{\bar{\lambda}} \quad . \tag{1.6}$$

When the term Brownian motion is used in the sense of migration of the *same molecule type* within the molecular order, the process is called self-diffusion. Water molecules at normal conditions[1] with $\bar{v} \simeq 1\,\mathrm{m/s}$ and $\bar{\lambda} \simeq 1\,\mathrm{pm}$ [7] collide at a frequency of $f_{coll} = 10^{12}$/second. Brownian motion cannot be observed on bigger particles in a liquid because the mass of the particle grows faster than the total momentum due to collisions with the surrounding molecules.
As a result, there is no net force on the particle. A classical solution for the problem of molecular motion is therefore impossible to obtain. Assuming discrete collisions, the trajectory of a molecule is continuous, but not differentiable. Of course, strictly, the idea of molecules as rigid bodies is not justified.
The motion of a diffusing molecule can be formally discretized by dividing the motion path into intervals. This gives rise to the concept of the *Random Walk*.

Random Walk

A Random Walk (RW) is a path between discrete sites. At each end point, the next step is chosen randomly from a set of sites. The Random Walk can be generalized leading to the formalism of Markov chains. In the limit of infinitely small steps, the path becomes a continuous curve (Wiener process). Some restrictions can be imposed on a Random Walk to simplify the computational realization, e. g.

- The sites are represented by the cross points of a rectangular lattice.
- The distance ϵ between steps and the length of the time interval Δt are constant. This implies that the following position is chosen from the neighboring sites.
- The probability for staying at the present position is zero.

The simple RW is appropriate to simulate Brownian motion with finite precision given by the lattice parameter ϵ. The RW is symmetric, which means that the transition probabilities $P_+ = P_-$ are independent from the direction of movement. Fig. 1-5 shows three particle distributions after a 1D Random Walk of duration $q\Delta t$. If the origin is the starting point of all molecules, the resulting distribution follows a Gaussian normal distribution. An asymmetric RW with transition

[1] using the definition: $101.325\,\mathrm{kPa}$, 25°C

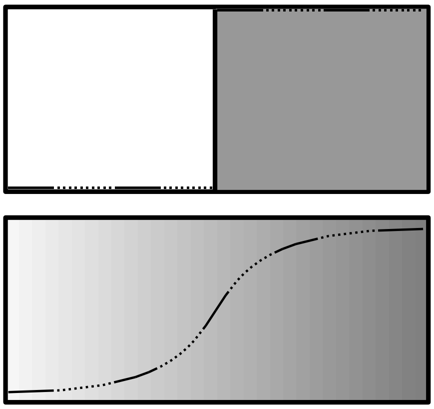

Figure 1-3. *Schematic display of a concentration gradient in a vessel before and after removing the separating wall (solid line). The concentration is shown in a gray scale and as a function of x (solid-dotted line).*

probabilities $P_+ > P_-$ generates a net drift with velocity v in the positive x-direction

$$\begin{aligned} P_+ &= \frac{1}{2} + \frac{v\,\Delta t}{2\,\epsilon} \\ P_- &= \frac{1}{2} - \frac{v\,\Delta t}{2\,\epsilon}. \end{aligned} \tag{1.7}$$

1.1.3 Concentration gradients

The macroscopic view of diffusion is based on the observation that the concentration of a substance tends to equalize. Fig. 1-3 shows schematically how a concentration gradient levels off when the separating wall is removed. The effect is a result of particle fluctuations. Mathematically, it is described by the flow rate F which is defined as the particle number or the mass/(time $\times$ area). The flow rate of a diffusing substance through the unit area is proportional to the concentration gradient perpendicular to this area [12]

$$\vec{F} \;=\; -D\,\vec{\nabla} C(\vec{r}, t). \tag{1.8}$$

The proportionality constant D is the diffusion coefficient. D has the unit area/time. Fick's second law [5] can be derived from Eq. 1.8 by multiplying it with the divergence operator. Subsequent inserting of the continuity equation leads to

$$\frac{\partial C(\vec{r}, t)}{\partial t} \;=\; D\,\Delta C(\vec{r}, t). \tag{1.9}$$

The diffusion equation describes the temporal and spatial propagation of a concentration distribution. The integration of Eq. 1.9 gives the concentration as a function of position and time. Assuming an initial point-like distribution of molecules, which is equivalent to $C(x, t_0) = \delta(x - x_0)$, the solution of the diffusion [12] equation is given by

$$C = \frac{N}{2\sqrt{\pi D t}}\, e^{-\frac{x^2}{4Dt}}. \tag{1.10}$$

where N is the total number of molecules. In two and three dimensions, the following identities hold

$$\begin{aligned} C &= \frac{N}{4\pi D t}\, e^{-\frac{r^2}{4Dt}} \\ C &= \frac{N}{8(\pi D t)^{3/2}}\, e^{-\frac{r^2}{4Dt}}. \end{aligned} \tag{1.11}$$

With different initial and boundary conditions, the analytic solutions to Eq. 1.9 can become complex. In the special case of a step-like initial condition in one dimension, the solution of the diffusion equation is [12]

$$c(x,t) = \frac{1}{2}\, c_0 \left[\mathrm{Erf}\left(\frac{x}{\sqrt{4Dt}}\right)\right]. \tag{1.12}$$

Erf denotes the errorfunction [10]. The following function specifies diffusion in a vessel whose walls are in a distance of $-l$ and $+l$ from the origin. The walls are reflecting. The initial distribution of particles $c(x)$ is 1 for $0 \le x < h$ and 0 for $-h \le x < 0$ and the solution becomes [12]

$$c(x,t) = \frac{1}{2}\, c_0 \left[\sum_{n=-\infty}^{\infty} \left(\mathrm{Erf}\left(\frac{n2l + x}{\sqrt{4Dt}}\right) + \mathrm{Erf}\left(\frac{n2l - x - 2h}{\sqrt{4Dt}}\right)\right)\right]. \tag{1.13}$$

This relation is visualized in Fig. 1-4 and compared to results from a RW simulation. The computer program simulates the Brownian motion of 1.28×10^6 particles on a one-dimensional lattice with length 256. The influence of reflecting walls becomes significant as soon as the travelled distance is in range of the walls.

Because diffusion is a stochastic process, there is no linear relationship between time and the distance from the starting point of a molecule. No direction is preferred and the average distance $\langle x(t) - x(t_0)\rangle$ is always zero. Rather a linear relationship for the mean square distance holds

$$\langle x^2(t)\rangle = 2\, D\, t. \tag{1.14}$$

This relation is known as Einstein-Smoluchowski equation. The symbol $\langle \ldots \rangle$ is meant as a summation over the position of all molecules. Accordingly, in two and three dimensions it is

$$\begin{aligned} \langle r^2(t)\rangle &= 4\, D\, t, \\ \langle r^2(t)\rangle &= 6\, D\, t. \end{aligned} \tag{1.15}$$

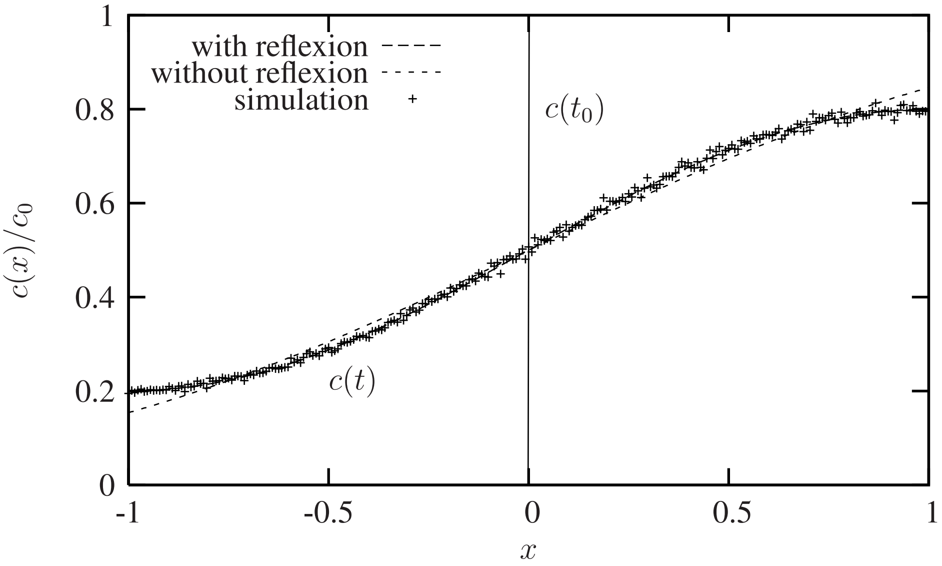

Figure 1-4. *Plot of Eq. 1.13 and Eq. 1.12 compared to simulation data. $c(t_0)$ marks the step-like initial distribution of particles (all particles on the right side). The crosses show their positions after performing a Random Walk of* 10000 *steps.*

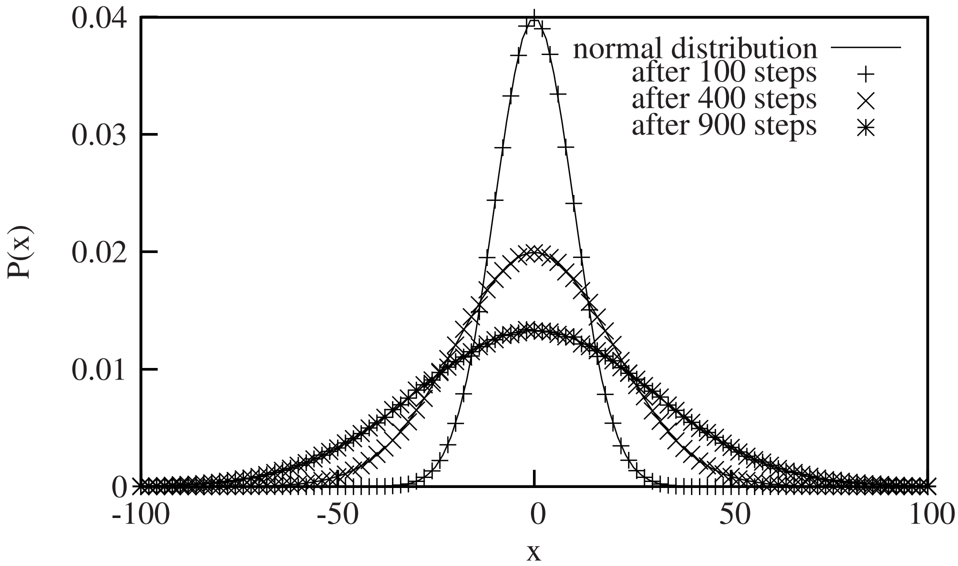

Figure 1-5. *The probability distribution of end points for a 1D Random Walk after q steps follows a normal distribution with width $\sigma = \sqrt{2Dq\Delta t}$. The parameters are $D = 1$ and $\Delta t = 1$. Theoretical normal distribution and simulation data for $q = 100$, 400 and 900 steps.*

The diffusion coefficient D and the size of a particle, or molecule, are correlated by the Stokes-Einstein equation [13]

$$D = \frac{k_B T}{6\,\pi\,\eta\,R_h}. \tag{1.16}$$

which is valid for spherical objects. The relation is frequently used to express the size of molecules by their hydrodynamic radius R_h. R_h is not necessarily equal to the real radius because the molecular shape is rarely spherical. According to Stoke's laws for friction in fluids, the relation depends on the Boltzmann constant k_B, the temperature T, and the viscosity η of the medium. In general, η is a function of the temperature, too. A molecule's mass M is proportional to its volume, and thus $M \propto R_h^3$. Because D is inversely proportional to R_h, it is difficult to distinguish molecules with different weight by their diffusion coefficients. In practice, the diffusion coefficients of two molecules only differ significantly if their mass ratio is greater than ≈ 6. Table 1.1 lists the coefficients of a number of species diffusing in water. For flexible molecules and other geometries Eq. 1.16 must be corrected. The correction for rod-like objects is [14]

$$D = \frac{k_B T\,\ln(2r)}{6\,\pi\,\eta\,a}. \tag{1.17}$$

Here, it is assumed that the diffusing molecule is a prolate ellipsoid with a long axis a and an axis ratio $r \gg 1$.

Another useful relation is the average time between the random arrival of two molecules in a volume of radius a. It can be derived from the diffusion equation 1.9 [15]

$$\bar{t} = (4\,\pi\,D\,a\,C)^{-1} \tag{1.18}$$

For a concentration of one molecule in a femtoliter and a diffusion coefficient of $D = 10^{-10}\,\mathrm{m}^2/\mathrm{s}$, the time to observe 100 molecule transitions is about $T = 128\,\mathrm{ms}$. Slower molecules with $D = 10^{-12}\,\mathrm{m}^2/\mathrm{s}$ need an accordingly longer time, $T = 12.8\,\mathrm{s}$. Here, it is assumed that each molecule is counted. In a real fluorescence measurement, the detection efficiency and photonic fluctuations must be considered as well.

1.1.4 Flow and diffusion in microchannels

Liquid flow on the micrometer scale shows some special properties compared to normal scale systems. For the description of liquid flows in microchannels some basic laws from hydrodynamics are recalled. The volume V of a fluid running through a pipe of radius R and length l is given by *Hagen-Poiseuille*'s law [11]

$$\frac{dV}{dt} = \frac{\pi}{8\,\eta\,l}\,(p_1 - p_2)\,R^4, \tag{1.19}$$

substance & solvent	T [K]	D [m^2/s]
H^+ in H_2O [16]	298	9.31×10^{-9}
Na^+ in H_2O [11]	298	1.25×10^{-9}
Cl^- in H_2O [11]	298	1.78×10^{-9}
ethanol in H_2O [11]	298	1.08×10^{-9}
R6G in H_2O [17]	298	2.8×10^{-10}
hemoglobin in H_2O [18]	293	6.3×10^{-11}
insulin in H_2O [18]	293	8.2×10^{-11}
spherical particle (polystyrol, $\varnothing = 1\,\mu\mathrm{m}$) in H_2O	295	4.45×10^{-13}

Table 1.1. *Experimental diffusion coefficients of some substances in water.*

where the pressure difference between inlet and outlet is $p_1 - p_2$. The value η names the viscosity of the fluid. In fluid dynamics, it is important to distinguish laminar from turbulent flow. Laminar flow is characterized by the fact that the stream lines follow a predictable direction. Vortices can exist, but in general the flow shows a stationary behavior. Turbulence, on the other hand, occurs when the flow velocity exceeds the limit where the friction force at the boundary layer becomes strong. The flow changes from laminar to unstable and chaotic behavior. A local perturbation grows exponentially in contrast to laminar flow where it decays exponentially. The transition from laminar to turbulent flow can be characterized by the dimensionless Reynolds number [5]

$$Re = \frac{\bar{v}\,\rho\,d}{\eta}. \tag{1.20}$$

For applications in microchannels with diameters d smaller than $100\,\mu\mathrm{m}$ and in aqueous solution, the flow velocity has to be greater than $20\,\mathrm{m/s}$ before, at a Reynolds number between 2000 and 3000, a transition to turbulent flow occurs. Hence, the flow in microstructures is laminar.

1.2 Fluorescence

Fluorescence occurs when a molecule emits a photon after it has been electronically excited by light absorption. The excitation of electrons and the emission of photons are stochastic processes. The spectrum of the emitted light is shifted to longer wavelengths (Stokes shift) [19]. The energy difference is transferred to neighboring molecules through collisions. This transmission occurs radiationless by exciting molecular oscillations (vibrational relaxation). Other processes, such as internal conversion, also play a role in the relaxation process. The diagram of electronic states for a fluorescent molecule is depicted in Fig. 1-6. The photon emission probability follows an exponential distribution. The average time between absorption and emission of a photon is typically in the range of nanoseconds. This time is referred to as lifetime $\tau_{10} = k_{10}^{-1}$ of the S_1 electronic state. The reason for the existence of a continuous emission spectrum is, that the density of oscillation

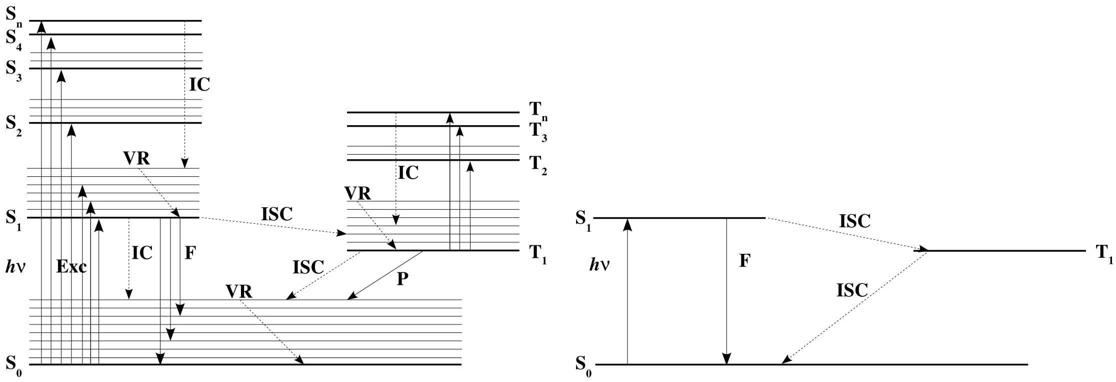

Figure 1-6. *The Jablonski diagram shows possible electronic transitions of a molecule (left). The abbreviations are IC = internal conversion, F = fluorescence, VR = vibrational relaxation, ISC = intersystem crossing, P = phosphorescence. It is often simplified to a ground state S_0, an excited state S_1, and a triplet state T_1 (right). The image was redrawn from [17].*

states is much higher than the one for electronic excitation. There are fluorescence molecules with varying spectra from the UV to the IR. The excitation and emission spectra of a typical dye is shown in Fig. 1-9. The intensity of the excitation light $I_{exc} = P/A$ depends on the photon flux Φ_{exc} and the photon energy $h\,c/\lambda$

$$I_{exc} \;=\; \Phi_{exc}\,\frac{h\,c}{\lambda} \;=\; \frac{\nu}{A\,t}\,\frac{h\,c}{\lambda}, \tag{1.21}$$

where h names Planck's constant, c the speed of light and ν the number of photons with wavelength λ. A stands for the illuminated area. The energy diagram is often simplified to a three state system of a ground state S_0, an excited state S_1 and a triplet state T_1. By setting up the differential equations for the transition rates, the fluorescence emission rate k_f can be related to the excitation intensity I_{exc} [17],

$$k_f \;=\; \frac{\phi_f\,\sigma_{exc}\,I_{exc}}{1 + \tau_{10}\,\sigma_{exc} I_{exc}\;(1 + k_{12}/k_{20})} \tag{1.22}$$

The fluorescence quantum yield ϕ_f, the cross section for excitation σ_{exc}, and the transition rates k_{12}, k_{20} vary among different fluorophores (cp. Tab. 1.2). In case of small intensity the linear approximation holds

$$k_f \;=\; \phi_f\,\sigma_{exc}\,I_{exc} \tag{1.23}$$

Fig. 1-8 shows the emission rate of one Rhodamine 6G molecule plotted against the excitation rate. The emission rate reaches a saturation value. The number of emitted photons ν in a time interval follows a Poisson distribution with a parameter $\mu = k_f \Delta t$

$$P(\nu|\mu) \;=\; \mu^{\nu}\,\frac{e^{-\mu}}{\nu!}. \tag{1.24}$$

In general, μ depends on the local light intensity $I_{exc}(\vec{r})$ via Eq. 1.22.

The Poisson distribution has the feature that the sum of m stochastically independent processes again follows a Poisson distribution with a parameter $\mu = \sum_{k=1}^{m} \mu_k$. The resulting distribution is given by their convolution. In the following, this relation is referred to as *recovering property* [20].

$$P(\nu|\mu) = P(\nu|\mu_1) \otimes \cdots \otimes P(\nu|\mu_m). \tag{1.25}$$

The fluorescence excitation and emission cycle can be interrupted by an electronic transition from the singlet S_1 to the triplet T_1 state (intersystem crossing). This transition corresponds to a (forbidden) inversion of the electron's spin. The inversion is forbidden unless a second molecule participates in the reaction and mirrors the spin difference. For the same reason, the probability for the back transition from $T_1 \rightarrow S_0$ is small. Thus, the triplet state lifetime is much longer than the singlet state lifetime. While a molecule is in the triplet state, it appears dark. The emission of a photon from the triplet state is called phosphorescence to set it apart from fluorescence.

1.2.1 Fluorescence dyes

In the experimental section, two fluorophores are used: Rhodamine 6G (R6G) and octadecyl Rhodamine B (R18). The chemical structures are shown in Fig. 1-7. The molecular properties of Rhodamine 6G and R18 are summarized in Tab. 1.2. R18 and R6G differ in the chemical structure of their side chains. This has an influence on the excitation and emission spectra. R18 is an amphiphilic molecule with a polar head and an unpolar tail. It is useful in lipid environments.

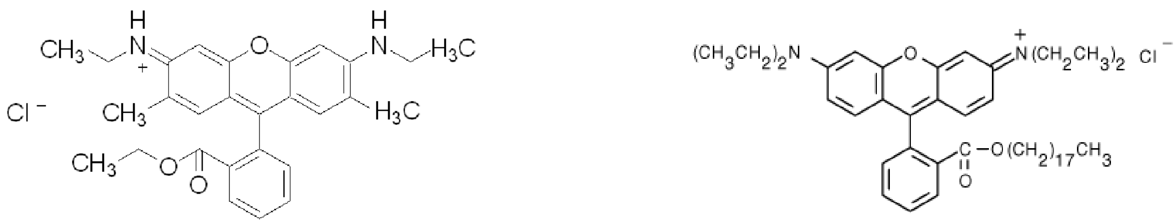

Figure 1-7. *Chemical structures of Rhodamine 6G (left) and octadecyl Rhodamine B (right).*

1.2.2 Photostability

Fluorescent molecules have a limited stability, especially while in the excited state. The loss of the fluorescence property is also called *bleaching* and describes the photo degradation of the

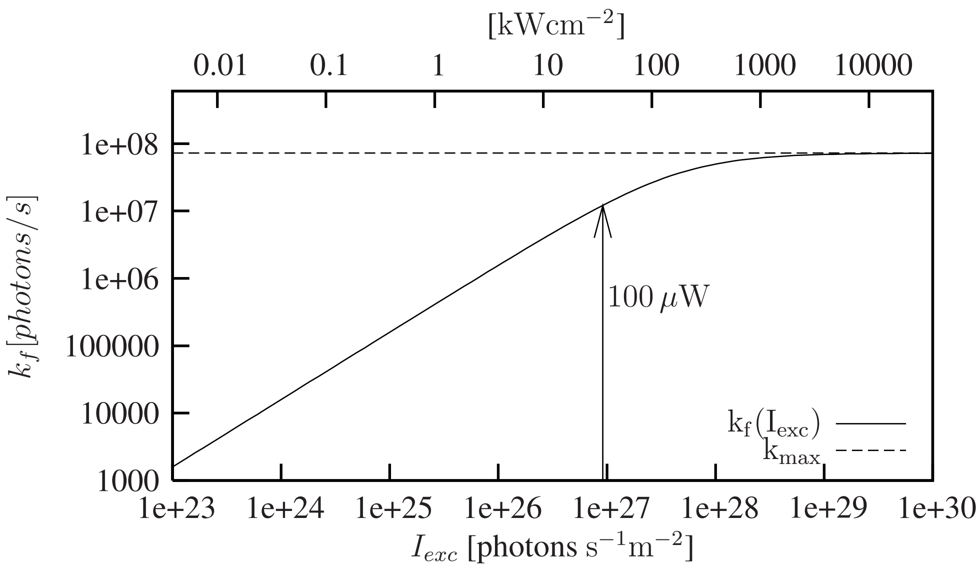

Figure 1-8. *Fluorescence emission rate k_f vs. excitation rate for a molecule with properties from Tab. 1.2. On the top abscissa the excitation rate is converted into an intensity value. The saturation value is $k_{max} = \phi_f k_{20}\,\tau_{10}^{-1}/\,(k_{20} + k_{12})$. The arrow marks a typical experimental value at a laser power of* $100\,\mu$W.

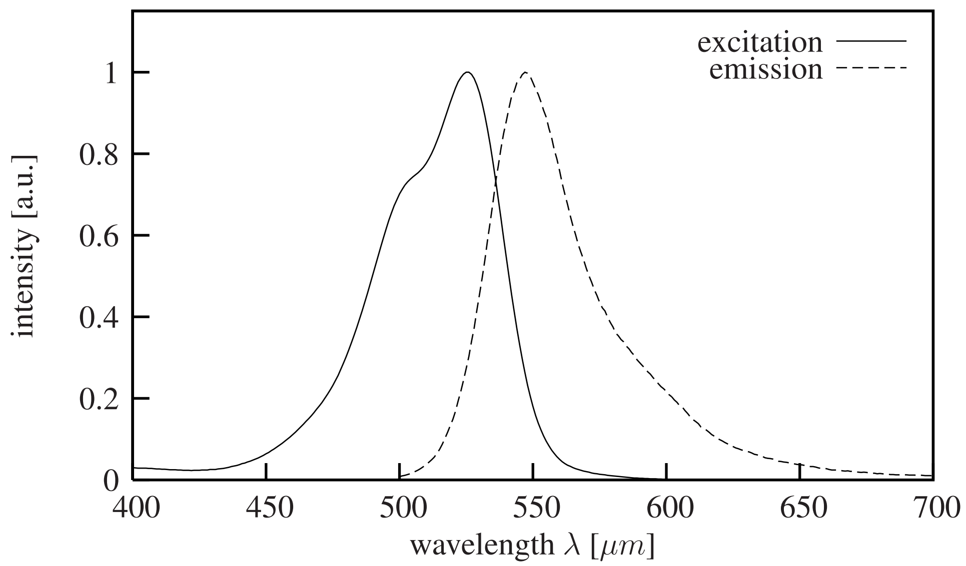

Figure 1-9. *Fluorescence excitation and emission spectrum of Rhodamine 6G (in arbitrary units).*

	symbol	unit	R6G	R18
molecular weight	M		479.02	731.5
excitation cross section	σ_{exc}	m^2	1.7×10^{-20}	n. d.
rate $S_1 \rightarrow T_1$	k_{12}	s^{-1}	1.1×10^6	n. d.
rate $T_1 \rightarrow S_0$	k_{20}	s^{-1}	4.9×10^5	n. d.
lifetime	τ_{10}	ns	4	1.5
quantum yield	ϕ_f		0.936	n. d.
photo bleaching (at $P < 150\,\mathrm{kW/cm^2}$)	ϕ_{bl}		$5e-6$	n. d.
excitation maximum	λ	nm	525	555
emission maximum	λ_{em}	nm	547	578

Table 1.2. *Some properties of Rhodamine 6G (from [17, 21]) and R18 in water. No data (n. d.) was available for some properties of R18.*

molecule. The time until a fluorophore has been bleached is exponentially distributed with a bleaching lifetime of $\tau_{bl} = k_{bl}^{-1}$. The rate k_{bl} can be expressed by the photo bleaching quantum yield [22]

$$\phi_{bl} = k_{bl}\,\tau_{10}. \tag{1.26}$$

It depends on specific properties of the fluorophore and on external influences, such as the oxygen and ion content of the solution [23]. The photostability is an important parameter for single molecule experiments when fluorophores are observed for a longer time.

1.3 Confocal optics

Fluorescence Correlation Spectroscopy is a method basically used to determine low concentrations and molecular diffusion coefficients in liquid environments. The sensitivity in FCS is on the single molecule level and the measurement data directly result from the observation of a small ensemble of molecules. Ensemble averaging is necessary for the standard correlation function approach that was proposed by Magde and Elson [24, 25] in 1974. The key in FCS is the reduction of the observation volume by using a confocal microscope (Fig. 3-1). The confocal principle is a simple way to co-locate the excitation and observation volume of a strongly focused light spot. In the focus center, fluorescent molecules emit photons shifted to longer wavelengths in response to electronic excitation. This light is separated from the excitation light by an optical filter. Background light is suppressed by an aperture (pinhole) placed in the back focal plane. The fluorescence time series $I(t)$ is detected with a photo diode. An example for $I(t)$ is shown in chapter 2, Fig. 2-1. From $I(t)$ the autocorrelation, Eq. 1.30, is computed. The correlation curve contains information about temporally correlated processes in the fluctuating signal. This information can be extracted from the correlation function although the underlying processes are stochastic. The basic parameters of interest are usually the diffusion coefficient and the particle number in the observation volume. To determine the diffusion coefficient, knowledge about the size of the observation volume is required.

1.3.1 Focus calculation

For the analysis of the fluorescence intensity time series, it is necessary to introduce some optical functions which describe the light distribution in the beam path. The molecule detection efficiency $MDE(\vec{r}, z)$ is defined as the product of excitation intensity $I_{exc}(\vec{r}, z)$ and the collection efficiency function $CEF(\vec{r}, z)$ [26]

$$MDE(\vec{r}, z) := CEF(\vec{r}, z)\, I_{exc}(\vec{r}, z) \tag{1.27}$$

The shape of this function can be appoximated by an effectively Gaussian profile along all three axis [27]

$$MDE(\vec{r}, z) \approx W(\vec{r}, z) = W_0 \exp\left(-2\frac{x^2 + y^2}{w_0^2} - 2\frac{z^2}{z_0^2}\right) \tag{1.28}$$

This approximation considerably simplifies the further calculation. The Gaussian parameters w_0 and z_0 correspond to the beam waists, where the effective intensity has decreased to $1/e^2$. A theoretical calculation for them was given by Rigler and Mets [26]

$$\begin{aligned} w_{th} &\geq \frac{\lambda}{n\,\pi\,\tan(\alpha/2)} \\ z_{th} &\approx \frac{e\,s_0}{\tan\alpha} \times 0.72. \end{aligned} \tag{1.29}$$

s_0 is the pinhole radius divided by the magnification. The pinhole size is important with respect to the collection efficiency function. The optimal size is a compromise between collection efficiency and suppression of background light from planes above and below the focal plane. z_{th} must be corrected by a factor depending on $\sin\alpha$. Here, it is 0.72 for $NA = 1.2$. In practice, the theoretical values are hardly reached. The values hold under ideal conditions of a Gaussian beam profile and an optimal aperture position. The finite size of the objective's illuminated rear side puts an upper limit on the focusing half angle $\alpha = \arcsin(NA/n)$. The theoretical focus parameters are given for two chosen configurations in Tab. 1.3. The refractive index n of the specimen is ideal if it matches the one of the immersion medium between the objective and the cover glass. Differences in the refractive index lead to small changes of the focus waist. Microscope objectives are calibrated for a cover glass thickness of $170\,\mu\mathrm{m}$. Even slight variations of $\pm 10\,\mu\mathrm{m}$ result in significant errors and increase the focus waist [28]. Numerical calculations have revealed more optical effects arising in a confocal microscope [27]. Hess's study shows that it is important if the back aperture of the microscope objective is completely, or only partially, illuminated with

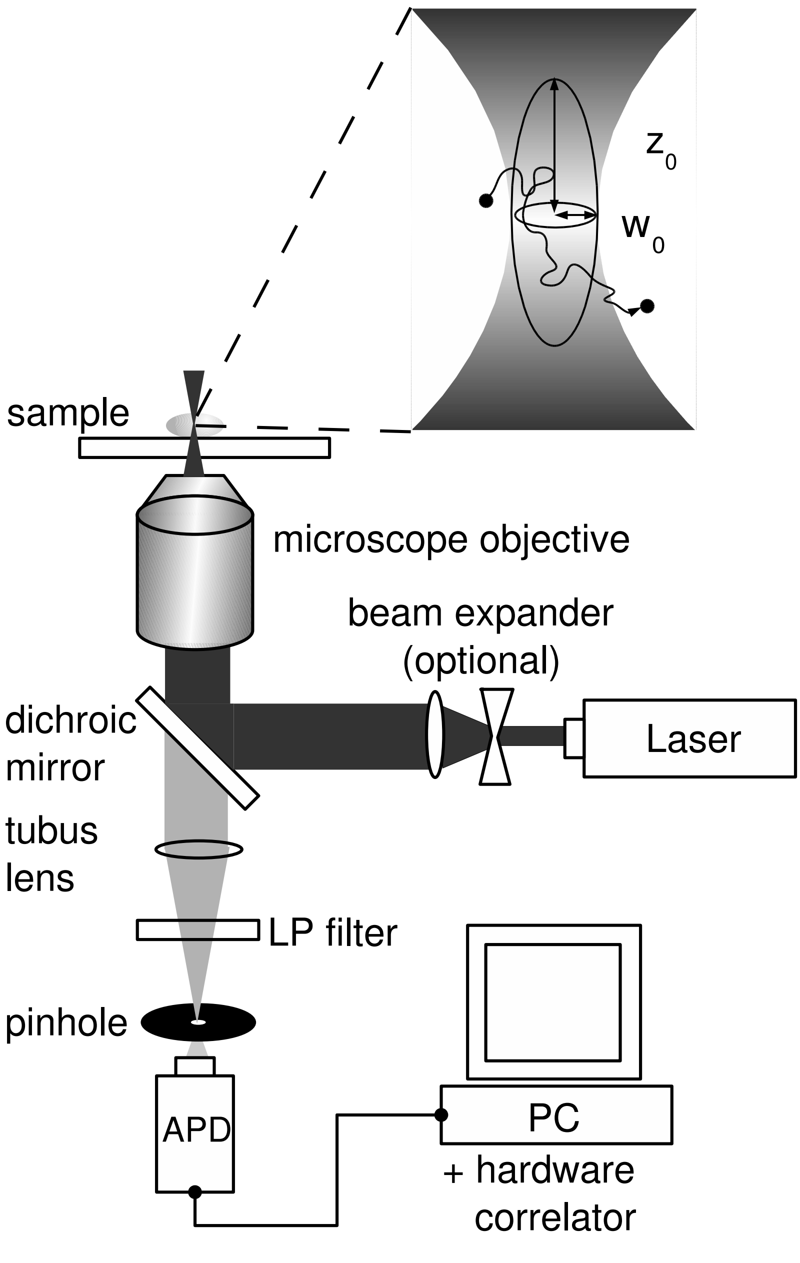

Figure 1-10. *Inverted confocal microscope for FCS and definition of the focus parameters w_0 and z_0 (magnified). See also Fig. 3-1.*

config.	MO	λ	pinhole	w_{th}	z_{th}	V_0
		nm	μm	μm	μm	fl
ConfoCor 2	$40\times$, 1.2 W	543	78	0.206	1.8	0.43
open microscope	$63\times$, 1.2 W	514	50	0.195	0.74	0.16

Table 1.3. *Theoretical focus parameters for two configurations of microscope objectives (MO) obtained by Eq. 1.29. The refractive index was set to* 1.33.

the laser beam. These effects become relevant only at distances $> 1/e^2$ from the beam axis. They should be accounted for in the case that absolute concentrations are determined but can be neglected otherwise.

1.4 Fluorescence Correlation Spectroscopy

From the intensity time series $I(t)$ the autocorrelation function is computed in order to extract the temporal information from the signal. This can be done after the entire signal has been recorded, but usually, it is achieved in real time by special correlation board hardware. The correlation function was first applied to fluorescence measurements by Magde and Elson [24, 25] in 1974, while the mathematical concept of the autocorrelation goes back to Wiener in 1930 [29].

1.4.1 Theory

The theory of FCS is explained following the representation in [17] and [26]. The goal is to find an analytical expression for the correlation curve of diffusing fluorescent molecules in solution. The general approach combines the solution of the diffusion equation with the shape of an effective excitation profile, and subsequently performs an integration over space. Starting point is the definition of the correlation function

$$\begin{aligned} G(\tau) &:= \frac{\langle I(t)I(t+\tau)\rangle}{\langle I\rangle} \\ \text{with} \qquad \langle I\rangle &= \frac{1}{T}\int_0^T I(t). \end{aligned} \tag{1.30}$$

T represents the total measurement time. By setting $\delta I(t) = I(t) - \langle I\rangle$, the correlation function can also be written as the fluctuation around the mean

$$G(\tau) = 1 + \frac{\langle \delta I(t)\delta I(t+\tau)\rangle}{\langle I\rangle}. \tag{1.31}$$

The fluorescence intensity can be written as a sum of all fluorescing molecules in the sample weighted by the excitation profile and the collection efficiency

$$I(t) \;=\; \alpha \int_{\mathbb{R}^3} d^3r\, C(\vec{r},t)\, \overbrace{CEF(\vec{r})\, I_{exc}(\vec{r})}^{Eq.1.28} \;\approx\; \alpha \int_{\mathbb{R}^3} d^3r\, C(\vec{r},t)\, W(\vec{r}). \tag{1.32}$$

The constant α is the number ratio of emitted and detected photons. Absorption of the emitted light can be neglected because the regarded concentrations are low. The effective measurement volume $W(\vec{r})$ is independent of time, and thus, the fluorescence intensity fluctuations $\delta I(t)$ originate mainly from the particle fluctuation $\delta c(\vec{r},t)$. With Eq. 1.32, Eq. 1.31 can be rewritten as

$$G(\tau) \;=\; 1 + \frac{\alpha^2 \int_{\mathbb{R}^3} d^3r \int_{\mathbb{R}'^3} d^3r'\, W(\vec{r})\, W(\vec{r'})\, \Phi(\vec{r},\vec{r'},\tau)}{\left(\alpha\, C \int_{\mathbb{R}^3} d^3r\, W(\vec{r})\right)^2}. \tag{1.33}$$

$C = \langle C(\vec{r},t)\rangle$ is the concentration average in the thermodynamic equilibrium. The term

$$\Phi(\vec{r},\vec{r'},\tau) \;=\; \langle \delta C(\vec{r},t)\delta C(\vec{r'},t+\tau)\rangle \tag{1.34}$$

subsumes the particle fluctuation. The integral in Eq. 1.33 can be evaluated if an expression for $\Phi(\vec{r},\vec{r'},\tau)$ can be found. The fluctuations due to Brownian motion are essential for the FCS method. The time course of a concentration distribution is described by Fick's laws, Eq. 1.8 - 1.9. But in this case, the solution cannot be obtained by direct integration of $\delta C(\vec{r},t)$. Unfortunately, the initial conditions for $\delta C(\vec{r},t)$ are unknown because the microscopic distribution of molecules is random. To solve the problem, the microscopic view from section 1.1.1 is helpful. It is possible to state a relation for the fluctuation between two arbitrary molecules at time lag $\tau = 0$,

$$\Phi(\vec{r},\vec{r'},\tau=0) \;\equiv\; C\,\delta(\vec{r}-\vec{r'},0). \tag{1.35}$$

Taking this as an initial condition for the diffusion equation, the general solution for Φ is found by integration

$$\Phi(\vec{r},\vec{r'},\tau) \;=\; \frac{C}{(4\pi D\tau)^{3/2}} \exp\left[-\frac{\left(\vec{r}-\vec{r'}\right)^2}{4D\tau}\right]. \tag{1.36}$$

Inserting $\Phi(\vec{r}, \vec{r'}, \tau = 0) = C\delta(\vec{r} - \vec{r'}, 0)$ into Eq. 1.33, the $\vec{r'}$ integration can be evaluated immediately. In the limit $\tau \to 0$, the correlation function becomes

$$\begin{aligned}
\lim_{\tau\to 0} G(\tau) &= 1 + \frac{\alpha^2 C \int_{\mathbb{R}^3} d^3r \int_{\mathbb{R}'^3} d^3r' \, W(\vec{r}) \, W(\vec{r'}) \, \delta(\vec{r} - \vec{r'})}{\left(\alpha C \int_{\mathbb{R}^3} d^3r \, W(\vec{r})\right)^2} \\
&= 1 + \frac{1}{C} \frac{\int_{\mathbb{R}^3} d^3r W^2(\vec{r})}{\left(\int_{\mathbb{R}^3} d^3r \, W(\vec{r})\right)^2}.
\end{aligned} \tag{1.37}$$

For $\tau \to 0$, $G(\tau) - 1$ is inversely proportional to the particle concentration C. Identifying the second term with the observation volume, it is justified to write

$$\lim_{\tau\to 0} G(\tau) = 1 + \frac{1}{C} \frac{\int_{\mathbb{R}^3} d^3r W(\vec{r})}{\left(\int_{\mathbb{R}^3} d^3r \, W(\vec{r})\right)^2} = 1 + \frac{1}{C \, V_0} = 1 + \frac{1}{N}. \tag{1.38}$$

N is the average number of molecules in the focus and V_0 is the redefined observation volume of FCS. It can be calculated analytically for the Gaussian approximation in Eq. 1.28

$$V_0 := \frac{\left(\int_{\mathbb{R}^3} d^3r \, W(\vec{r})\right)^2}{\int_{\mathbb{R}^3} d^3r W(\vec{r})} = \pi^{3/2} \, w_0^2 \, z_0. \tag{1.39}$$

The geometry of the focus volume has the shape of an ellipsoid with semi-axes w_0 and z_0.
The time dependence of the correlation function must be calculated by inserting Eq. 1.36 into 1.33. The integration can be done analytically, leading to the final result [17]

$$G(\tau) = 1 + \frac{1}{N} \left(1 + \frac{\tau}{\tau_d}\right)^{-1} \left(1 + \frac{\tau}{K^2 \, \tau_d}\right)^{-0.5}. \tag{1.40}$$

The ratio of the long and short axis of the focus is the so-called structure parameter

$$K := \frac{z_0}{w_0}. \tag{1.41}$$

If diffusion is the dominant process, the value where $G(\tau) - 1$ has decreased to $0.5N^{-1}\sqrt{1 + K^{-2}}$ is the diffusion time

$$\tau_d := \frac{w_0^2}{4 \, D}. \tag{1.42}$$

When τ_d and w_0 are known from an experiment, D can be identified with the coefficient of the diffusing species. The diffusion time is proportional to the average time that a molecule spends inside the focal volume. Examples for correlation functions are given in chapter 2.

Focus calibration

In real experiments, the exact shape of the excitation intensity and the collection efficiency func-

tion are hardly known. They depend strongly on the optical adjustment of the beam path. The theoretical calculation of the focus parameters is not valid exactly. In practice, it is often better to calibrate the values with a standard solution with a well-known diffusion coefficient. Here, Rhodamine 6G solutions in concentrations of $\approx 10^{-8}$ M are used throughout.
After calibrating the focus size, the diffusion coefficient of a different species can be compared to the calibration standard. Thereby, molecular motion can be characterized applying the accordant model equations, for example for free diffusion, or directed motion. Diffusion coefficients can be taken to distinguish molecules by the size, weight, and shape, and also to characterize the viscosity and structure of the surrounding material. Chemical reactions and binding processes can be observed if concentrations or diffusion coefficients are determined repeatedly with respect to the reaction time. Additionally, phenomena of electronic excitation and emission can be studied in detail (e. g., bleaching, fluorescence anisotropy, triplet state processes, molecule rotation, etc.).

Resolution
In Fluorescence Correlation Spectroscopy a microscopic volume is illuminated. The size of this observation volume is governed by the diffraction limit of the excitation light resulting in a volume of approximately $0.5\,\mathrm{fl}$. The extension in axial direction also depends on the pinhole diameter. The time resolution depends on the dead time of the photon detector and the sampling time of the hardware correlator. The diffusion time/molecule is typically between 0.2 and $3\,\mathrm{ms}$. The measurement result for the diffusion time is an ensemble average over time and the number of molecules that have crossed the focal volume on a random path.

1.4.2 Variance of the autocorrelation

In an autocorrelation measurement, variations occur due to the statistical nature of the observed processes. To determine the error of the diffusion coefficient and the concentration value, the variance of the autocorrelation values is needed. It is useful to calculate the variance from known experimental parameters. This also provides insight into the inherent dependencies of the error. The first approximation for the variance of $G(\tau)$ was given by Koppel in 1974 [30].

$$\begin{aligned}\sigma^2_{Koppel}(m\Delta\tau_i) \;=\; & \frac{1}{M\,N^2}\left[\frac{(1+g^2(\Delta\tau_i))\,(1+g^2(m\Delta\tau_i))}{(1-g^2(\Delta\tau_i))} + 2mg^2(m\Delta\tau_i)\right] \\ & + \frac{1}{M}\left[\frac{2\,(1+g^2(m\Delta\tau_i))}{N\langle n\rangle} + \frac{1}{\langle n\rangle^2}\left(1+\frac{g(m\Delta\tau_i)}{N}\right)\right]. \end{aligned} \tag{1.43}$$

For the function $g(\tau)$ the normalized and reduced autocorrelation function for three-dimensional diffusion is inserted

$$g(\tau) \;=\; \left(1+\frac{\tau}{\tau_d}\right)^{-1}\left(1+\frac{\tau}{K^2\,\tau_d}\right)^{-0.5}. \tag{1.44}$$

The parameters are $\langle n \rangle$, the average count rate/correlator channel, and $M = T/\Delta\tau$, the total number of measurement intervals and N the average number of molecules as defined in Eq. 1.38. $m\Delta\tau_i = \tau$ are multiples of the correlation time interval.
The formula was originally derived for a Gaussian fluctuation model with a large number of molecules in the observation volume. Furthermore, a uniform illumination profile, negligible background, and sampling times much smaller than the observed diffusion times were assumed. The function gives an estimate for the error, but systematic deviations occur for longer correlation times [31]. Among other ways to calculate the standard deviation [31, 32, 33], the most useful were given by Saffarian (Eq. 24 in [34]) and Qian [35]. In conclusion, the variance depends on the fluorescence quantum yield, the measurement time and the number fluctuations of particles in the observation volume. In the high concentration range, the signal-to-noise ratio $G(m\Delta\tau_i)/\sigma(m\Delta\tau_i)$ of the correlation function is independent of the concentration [30]. Otherwise, the method improves in signal-to-noise ratio with higher particle fluctuation [24, 36]. It also has to be considered that hardware correlators work with a logarithmic time scale and the interval time is not constant [37].
The easiest way to obtain the variance experimentally is to record a number of correlation curves $G_{1...n}$, and then, calculate the mean $\langle G(m\Delta\tau_i)\rangle$ and the variance for each correlation time according to

$$\sigma^2(m\Delta\tau_i) = \frac{1}{n-1}\sum_{k=1}^{n}\left(G_k(m\Delta\tau_i) - \langle G(m\Delta\tau_i)\rangle\right)^2 . \qquad (1.45)$$

1.4.3 Triplet state

When a molecule undergoes a transition to the triplet state it appears dark until it returns to the excited state. Non-fluorescing molecules reduce the apparent number of molecules in the detection volume. The initial part of the correlation curve rises by a fraction which strongly depends on the excitation intensity. In the correlation function, the triplet fraction p appears as an exponential term in Eq. 1.40 [17]

$$G_{trip}(\tau) = 1 + \frac{1}{N}\left(1+\frac{\tau}{\tau_d}\right)^{-1}\left(1+\frac{\tau}{K^2\,\tau_d}\right)^{-0.5} \times \left[1 + \frac{p}{1-p}\exp\left(-\frac{\tau}{\tau_{trip}}\right)\right] \qquad (1.46)$$

The triplet life time $\tau_{trip} = k_{21}^{-1}$ typically has a value of a few μs. The saturation value in fluorescence emission (Fig. 1-8) is influenced by the triplet lifetime. Systematic errors can occur resulting from this saturation but are neglected in the following chapters [38].

1.4.4 Directed flow

When the observed liquid is not at rest, but drifting in a defined direction, diffusion and stationary flow are concurrent processes. The differential equation 1.9 for this case must be generalized by a term depending on the flow velocity

$$\frac{\partial C(\vec{r},t)}{\partial t} = D\,\Delta C(\vec{r},t) - \vec{v}(\vec{r})\,\vec{\nabla} C(\vec{r},t). \tag{1.47}$$

If the liquid moves in x-direction only, the diffusion equation simplifies to

$$\frac{\partial C(\vec{r},t)}{\partial t} = D\,\frac{\partial^2 C(\vec{r},t)}{\partial x^2} - v_x(\vec{r})\,\frac{\partial C(\vec{r},t)}{\partial x}. \tag{1.48}$$

The solution is obtained by Fourier transformation [39]. With Eq. 1.48, the correlation function has the result [40]

$$G(\tau) = 1 + \frac{1}{N}\left(1+\frac{\tau}{\tau_d}\right)^{-1}\left(1+\frac{\tau}{K^2\,\tau_d}\right)^{-0.5} \times \exp\left[-\left(\frac{\tau}{\tau_{flow}}\right)^2\left(1+\frac{\tau}{\tau_d}\right)^{-1}\right]. \tag{1.49}$$

The average time for a molecule to cross the focus induced by the flow is τ_{flow}. The local flow velocity in x-direction is obtained by

$$v_x(\vec{r}) = \frac{w_0}{\tau_{flow}(\vec{r})}. \tag{1.50}$$

Chapter 2

Simulation of FCS

The conditions for an experiment should usually be chosen as simple as possible to focus on the most relevant question. However, in Fluorescence Correlation Spectroscopy (FCS) practical uncertainties cannot be excluded completely. For example, background fluorescence and noise from detection electronics always lower the signal-to-noise ratio. Another problem is that the exact shape and dimension of the focus are unknown. There is also no possibility to suppress photobleaching of the fluorophores completely. Altogether, the FCS method is good for measuring concentrations and diffusion coefficients relative to a known standard. The necessary effort to improve the setup and analysis to enable absolute measurements is high.
It is generally useful to construct an idealized experiment avoiding these difficulties. For this purpose, computer simulations can be used to simulate experiments and exclude unknown parameters. Several approaches are in use, each of them with advantages and disadvantages. Recently, Molecular Dynamics (MD) simulations gain popularity, especially when details about molecular interaction have to be studied. Still, they require high computational power. Regarding FCS, the Monte Carlo method is well suited for the relevant processes and time scales. This chapter presents an algorithm that is used to simulate FCS experiments on a computer. It starts with the first section 2.1, describing the Brownian motion of molecules. The simple Random Walk algorithm which was introduced in section 1.1.2 is applied to simulate their stochastic behavior. Section 2.2 deals with how the random process of photon emission is implemented. In section 2.3, the simulation results are verfied by comparing them to the theoretical expectations. At the end of the chapter, the special case of two-dimensional diffusion is regarded in particular. The simulation is used to find an FCS model which describes diffusion in bilayer systems (see also chapter 5).

2.1 Brownian motion

The algorithm is based on simulating the two fundamental processes, the Brownian motion of the molecules and the photon emission caused by fluorescence excitation. Both are random processes.

The molecule diffusion is realized by a simple Random Walk (RW) on a three-dimensional lattice with a side length $(L-1)\,\epsilon$. ϵ denotes the distance between two lattice points. The coordinates of the lattice points are $\vec{r}(x,y,z)$, with $x,\ y,\ z\ =\ \{0\ \ldots\ L-1\} \in \mathbb{N}$. The simulation volume then has a total size of

$$V_{sim}\ =\ (L-1)^3\,\epsilon^3. \tag{2.1}$$

The time axis is divided into a series of discrete points in time $\{t_i \in \mathbb{R},\ i \in \mathbb{N}\}$ with $t_{i+1} = t_i + \Delta t$. The interval Δt is given by the Einstein-Smoluchowski relation in three dimensions, Eq. 1.15,

$$\Delta t\ =\ \frac{\epsilon^2}{6\,D}. \tag{2.2}$$

Hence, the smallest time unit is defined by the diffusion coefficient D and the grid constant ϵ. At t_0, a number of N_0 molecules is placed on arbitrary positions of the lattice. Because the number of molecules in a subvolume is Poissonian distributed, the number N_0 is drawn from a Poisson distribution with the parameter $\mu = \bar{N}$. $\bar{N}$ is the average number of molecules in the simulation and determines the average concentration $c = \bar{N}/V_{sim}\,N_A$. After each time step the molecules move along the unit vectors to one of the six neighboring lattice sites with equal probability $1/6$. This means, the new position of the nth molecule is determined from the previous one by

$$\vec{r}_n(t_i)\ =\ \vec{r}_n(t_{i-1}) \pm \epsilon\,\vec{e}_j. \tag{2.3}$$

with the unit vectors $\vec{e}_j$, $j \in \{1,2,3\}$. The probability of a molecule to stay at its present position is 0. The boundary conditions of the simulation follow from the demand that the simulation volume contains a Poissonian distribution of diffusing particles (see section 1.1.2). If a molecules crosses the simulation boundary, which is equal to

$$\begin{aligned} \vec{r}_n(t_i)\ &<\ 0 \\ \vec{r}_n(t_i)\ &>\ L-1, \end{aligned} \tag{2.4}$$

the molecule is deleted from the simulation. To maintain the concentration on the time average, new molecules have to appear at the same rate at which they are deleted. The starting point of a new molecule is on a random position on one of the six faces of the lattice cube. For the rates to enter or leave the volume,

$$k_{out}\ =\ k_{in} \tag{2.5}$$

must be fulfilled. To find an expression for this rate, the individual probabilities for a molecule to exceed the boundary from a) a face b) an edge c) a corner must be summed up

$$P_{in} \;=\; \frac{\bar{N}}{L^3}\left[6\,\frac{1}{6}(L-2)^2 + 12\,\frac{2}{6}(L-2) + 8\,\frac{3}{6}\right] \;=\; \frac{\bar{N}}{L}. \tag{2.6}$$

The generating probability determines the rate at which new molecules enter the simulation volume. The relations above are implemented in the simulation as follows. The RW is realized by a program that generates a random number once every time step Δt. For each molecule a number between one and six is chosen randomly to state its next position. Afterwards, the implemented molecule generating function is called once every time step. Another random number is taken to decide if a new molecule enters the simulation volume. The (pseudo-) random number generator *ran1* suggested by Press is used [41].

2.2 Photon emission

Inside the simulation volume, a local light intensity $W(\vec{r})$ with wavelength λ is allocated to the lattice points. To simulate a focused laser beam, as it appears in FCS applications, the intensity profile is chosen as a three-dimensional Gaussian function (cp. Eq. 1.28),

$$W(\vec{r}) \;=\; \frac{P_0}{2\pi\; w_0^2}\,\exp\left[-2\epsilon^2\left(\frac{x^2+y^2}{w_0^2}+\frac{z^2}{z_0^2}\right)\right]. \tag{2.7}$$

Here, the variable P_0 is the laser's optical power, w_0 and z_0 are the focus semi-axes in radial and axial direction. The z-axis is defined as the laser beam axis. The focus semi-axes should be small in comparison to the side length of the lattice cube and large in comparison to the lattice parameter ϵ. In an experiment, the effective and the real excitation profiles are not identical. The probability to detect a photon depends in the molecules' positions. Here, for simplicity, the collection efficiency function $CEF(\vec{r}) = 1$ is chosen as unity. The simplification is justified as argued in section 1.3. The general validity of the FCS theory is not affected thereby.

The probability $P_i^{(n)}$ that the nth molecule emits ν photons in the time interval Δt between t_i and t_{i-1} is given by the Poisson expression

$$P_i^{(n)}(\nu|\mu) \;=\; \mu^\nu\,\frac{e^{-\mu}}{\nu!}. \tag{2.8}$$

The average value μ is assumed to be proportional to the effective excitation profile $W(\vec{r})$ of the molecule (Eq. 1.23, 1.28)

$$\mu(\vec{r}) \;=\; W(\vec{r})\,\frac{\lambda}{hc}\,\sigma_{exc}. \tag{2.9}$$

The cross section $\sigma_{exc}(\lambda)$ for fluorescence excitation is chosen constant. h and c name Planck's constant and the speed of light. Eq. 1.23 implies that only 2 electronic states exist, S_0 and S_1. The triplet state is neglected. For the purpose of simulating diffusive correlation functions, this assumption is justified because triplet state dynamics, bleaching, or emission saturation are irrelevant, here. In this sense, the simulation is intentionally limited to correlation functions governed by the motion of particles.
The photon distribution from N independent molecules is given by Eq. 1.25. The recovering property of the Poisson process allows to calculate the number of photons emitted by N molecules at time t_i directly:

$$\mu_N = \sum_{n=1}^{N} \mu_n. \tag{2.10}$$

In an experiment, usually a detector (avalanche photo diode or photo multiplier) in combination with a computer board (multichannel scaler) records the photon events within a minimal measurement interval ΔT. This bin time is the interval within that photons are collected. Because Poissonian emission processes from different molecules are independent from each other, the recovering property of the Poisson distribution can be applied again (Eq. 1.25). The sum of all photons within a bin interval also follows a Poisson distribution with the parameter

$$\mu_{\Delta T} = \sum_{i=1}^{m} \mu_N(t_i). \tag{2.11}$$

$m = \Delta T/\Delta t$ is the number of time steps in one measurement interval. $\mu_{\Delta t}$ can be calculated from the molecules' positions and the local intensity. Hence, the number of emitted photons from all molecules in ΔT can be simulated by drawing only one random number. $\mu_{\Delta T}$ is inserted into Eq. 2.8 instead of μ, thus returning the Poisson distributed photon number from N molecules. Thereby, the number of calls of the random number generator can be reduced efficiently.

Remark on the period of the random number generator
The random number period of *ran1* is about 10^9. For certain applications of random numbers the period exhaust turns out to be a problem. This limit is exceeded in the simulation. But, as Wohland pointed out, the period length can be neglected because the simulated particles are deleted before the number sequence repeats [31].

The number of detected photons is smaller than the number of emitted photons. The overall loss results from the optical setup and the detection efficiency of the detector. The constant factor γ subsumes the transmission coefficients θ_{trans} of all optical components along the emission beam path. The fluorescence quantum yield ϕ_f can also be included in this value, resulting in

$$\gamma \,=\, \Omega(NA)\,\theta_{trans}\,\phi_f. \tag{2.12}$$

A microscope objective covers the solid angle Ω which depends in the numerical aperture NA and the refractive index n of the medium

$$\Omega(NA) \,=\, 0.5\,\left[1 - \cos\left(\arcsin\left(NA/n\right)\right)\right]. \tag{2.13}$$

The refractive index is 1.33 for water. Otherwise, the photon emission is assumed to be isotropic in every direction. To account for these effects, the number of emitted photons is multiplied by γ.

Addition of dark counts

Dark counts from noise of the detector electronic, which is anavoidable in most applications, can be included easily. Because photon events from noise are an independent Poissonian process, it is sufficient to add the dark count rate ζ to $k_{\Delta t}$

$$\mu_{\Delta T}(\zeta) \,=\, \mu_{\Delta T} \,+\, \zeta. \tag{2.14}$$

2.3 Tests of the simulation

The result of a simulation run is a series of natural numbers $I(t)$, representing the number of detected photons ν in a measurement interval ΔT. From the simulated intensity signal (example in Fig. 2-1), the correlation function is calculated according to the defining Eq. 1.30.

The computer simulation requires to chose a set of parameters (Tab. 2.1 and Tab. 2.2). In contrast to an experiment, all parameters, including the focus shape and size, are known. These values are classified either as experimental parameters or simulation specific parameters. The values are further distinguished into optical parameters of the setup, and values which describe the specific properties of the fluorophore. In the simulations, some values remained constant throughout, whereas others had to be adjusted. Constant values were the wavelength, the objective's numerical aperture, the lateral focus size, the excitation cross section, the transmission factor, and the quantum yield. The optical parameters were set to values demanding that the overall detection efficiency γ was 4 % (a typical value for an FCS setup is 3 % [42]). The laser power, the vertical focus radius, the diffusion coefficient, and the concentration were altered for different tasks. The lattice parameter and the bin interval were constant while the lattice size and the total simulation time were adapted.

The performance of the simulation was verified by applying a series of tests. Necessary conditions are (A) that the given concentration, and (B) that the given diffusion coefficient, are correctly reproduced. The third test (C) checks for the variance according to Koppel's formula 1.43. The significance of (C) is limited because the calculated variance of the correlation function is only an approximation. Nevertheless, it is important to see if the range of fluctuation is reasonably simulated by the proposed algorithm. The influence of noise was not examined, and the value was set to zero. The simulation parameters are listed in Tab. 2.1 and Tab. 2.2.
A simulated intensity trace is depicted in Fig. 2-1 with the number of photon counts plotted as bars. 1000 intervals are shown. The intervals were re-binned to $0.1\,\mathrm{ms}$ intervals to visualize the photon fluctuation. The resulting correlation functions are analyzed by comparing them to the theoretical functions given in section 1.4.1. The deviations from the theoretical curves are shown as residuals in a separate graph below the actual diagram. The residuals are given in multiples of the standard deviation $\sigma(m\Delta\tau_i)$

$$res(m\Delta\tau_i) = \frac{\langle G_{sim}(m\Delta\tau_i)\rangle - G(m\Delta\tau_i)}{\sigma(m\Delta\tau_i)} \tag{2.15}$$

A correlation curve from the intensity data of 12 simulation runs is displayed in Fig. 2-3. The average correlation from the simulations is plotted as crosses with error bars representing their standard deviation. The expected theoretical function is drawn dashed. The standard deviation was calculated from a number of repeated realizations with Eq. 1.45. The results are:

1. Concentration
   12 realizations with parameters from Tab. 2.2 give an average number of particles of 1.01 ± 0.05. Theoretically, a value of 1.0096 was expected. Theory and simulation are in excellent agreement.

2. Diffusion coefficient
   A range of diffusion coefficients from 1×10^{-11} to $9 \times 10^{-11}\,\mathrm{m}^2/\mathrm{s}$ was simulated. From six realizations with a given diffusion coefficient the correlation functions were calculated and fitted to the standard FCS model with free parameters N and D. Each data point with error bars represents the mean and standard deviation from these six simulation runs. The dashed line marks the identical relation between the theoretical and simulated/fitted diffusion coefficients. Fig. 2-2 shows the correct reproduction of the diffusion coefficient for $D > 2 \times 10^{-11}\,\mathrm{m/s}$. The standard error given by the size of the error bars is about 3 %. The simulations for $D_{th} = 10^{-11}\,\mathrm{m}^2/\mathrm{s}$ show a systematic deviation towards a slower diffusion coefficient. This error is due to the lattice discretization. It can be avoided by chosing a different value for the step size ϵ. In general, the choice of ϵ is connected to the range of diffusion coefficients which shall be simulated.

	parameter	symbol	unit	value
setup	laser power	P	mW	0.2
	wavelength	λ	nm	514.5
	numerical aperture	NA		1.25
	transmission factor	θ_{trans}		0.1355
	noise level	η		0
	focus axis, lateral	w_0	μm	0.3
	focus axis, axial	z_0	μm	0.6
fluorophore	diffusion coefficient	D	m^2/s	$10^{-11}..9 \times 10^{-10}$
	exc. cross section	σ_{exc}	m^2	2×10^{-20}
	em. quantum yield	ϕ_f		0.9
	av. no. of mol. on lattice	N		56
simulation	lattice size	L		512
	lattice parameter	ϵ	nm	5
	simulation time	T	s	1.68
	bin interval	ΔT	μs	1
internal	time step	Δt	ns	$4.63 - 417$
	av. no. of mol. in focus	N		1.0096
	concentration	c	M	5.58×10^{-9}

Table 2.1. *Parameters for the simulation series (A) and (B), D_{sim} vs. D_{th}.*

3. Variance of the correlation
   The variance was determined from 12 realizations of simulated correlation curves with equal parameter settings. The chosen settings are listed in Tab. 2.2. Unlike in (A) and (B), the focus axes are equal forming a spherical profile. The diffusion coefficient was set to a value that is equivalent to six simulation time steps/bin interval. The variance is calculated according to Eq. 1.45 and compared to Koppel's, Qian's, and Saffarian's formulas (see section 1.4.2). Instead of the variance, the standard deviation is displayed in Fig. 2-4. The simulated data and the theoretical approximations agree within the accuracy of their derivation. However, systematic differences are obvious.

The simulation fulfills the tests. In the following section, it will serve as a tool to evaluate an FCS model for diffusion in oriented planes.

2.4 Diffusion in oriented planes

There are environments that show a supramolecular order of two-dimensional layers. In these surroundings, Brownian motion can be restricted to planes. This type of diffusion prevails, for example, in lamellar bilayers and membranes. When the molecules diffuse on a plane, its orientation in relation to the elongated observation volume is important (Fig. 2-5). The resulting correlation

parameter	symbol	unit	value
laser power	P	mW	0.1
focus axis, lateral	w_0	μm	0.2
focus axis, axial	z_0	μm	0.2
diffusion coefficient	D	m^2/s	2.5×10^{-11}
simulation time	T	s	4.19
time step	Δt	ns	166.7
av. no. of mol. in focus	N		0.1496

Table 2.2. *Simulation series (C), variance test, differs from (A) and (B) in these parameters.*

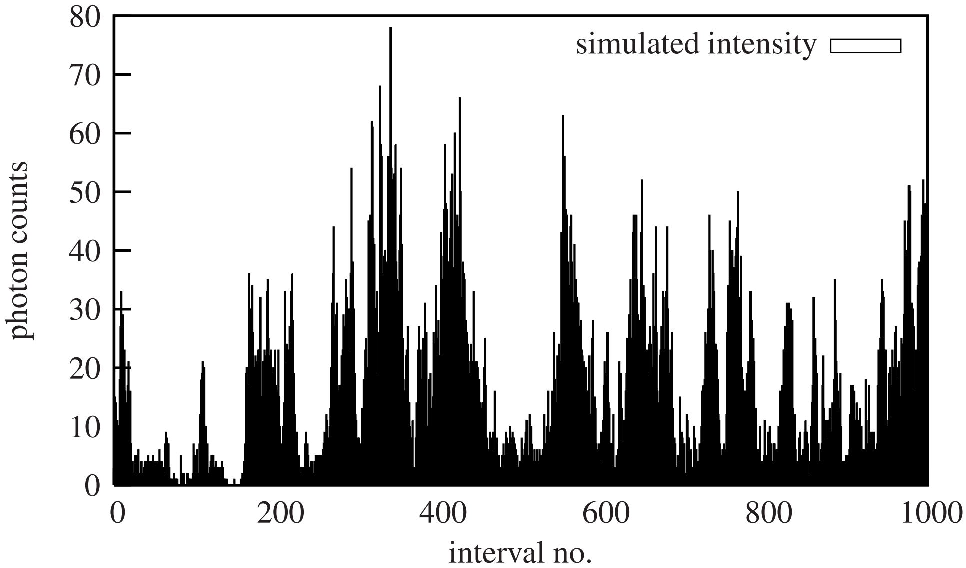

Figure 2-1. *Simulated intensity signal from molecules with the properties in Tab. 2.1. The time intervals were re-binned to 0.1 ms. Average number of molecules in the focus* $N = 1.01$.

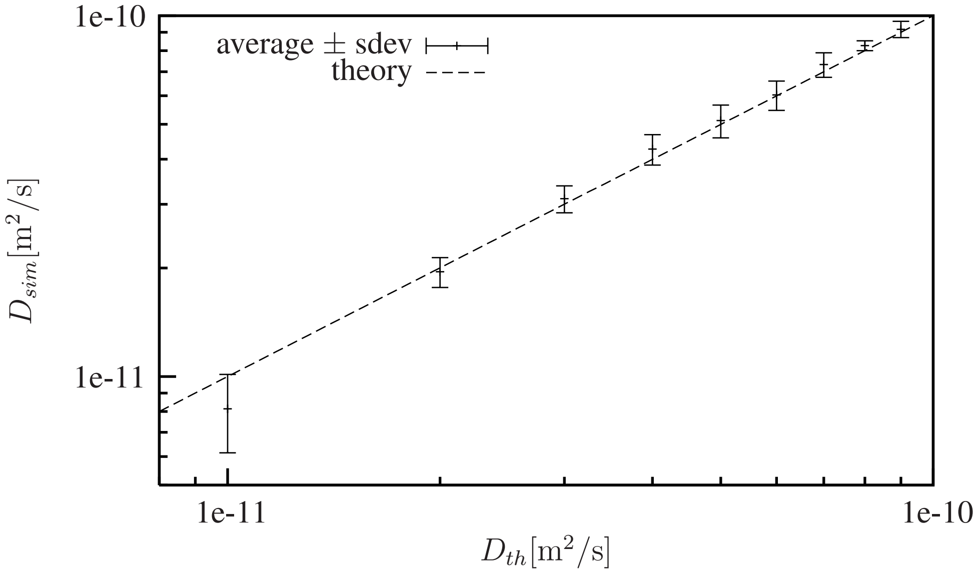

Figure 2-2. *Theoretical diffusion coefficient vs.* D_{sim} *from the simulation. Each point is the result of 6 simulation runs. Parameters were set according to Tab. 2.1.*

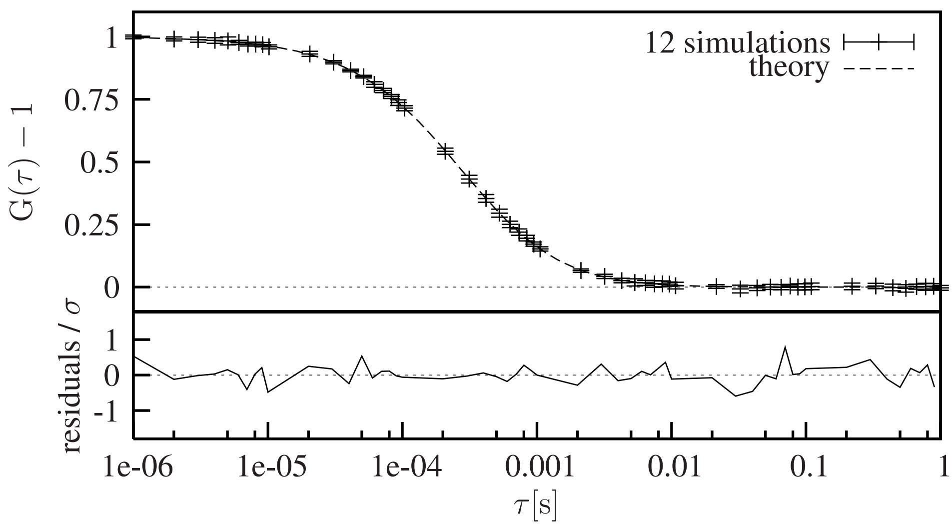

Figure 2-3. *Average autocorrelation and standard deviation from 12 normalized simulations of* 4.19 *seconds each. The parameters were set according to Tab. 2.2. The residuals below show the difference between the simulated curve and the theoretical function in multiples of the standard deviation.*

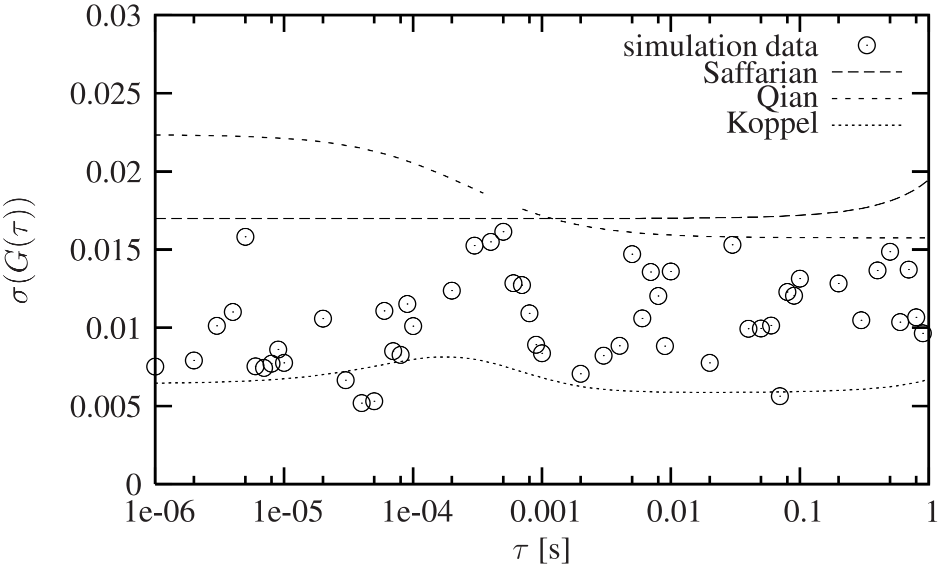

Figure 2-4. *Standard deviation of 12 simulations compared to Saffarian's, Qian's and Koppel's theoretical approximations.*

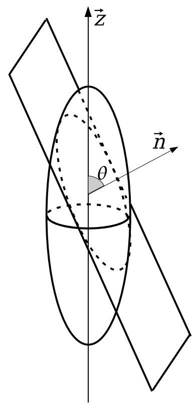

Figure 2-5. *In the orientation model, molecular diffusion is restricted to two-dimensional planes intersecting the focus intensity ellipsoid at arbitrary angles θ and vertical intercepts. Integrating contributions from a number of orientations results in an effective angle θ_m.*

function is expected to depend on the plane's normal angle [43]. Though it is possible to orientate a membrane (in a magnetic field or on a surface), and then perform an FCS measurement, it is experimentally easier to examine diffusion in non-oriented samples. In this case, there are a number of non-oriented layers contributing to the signal simultaneously. For the following, it is assumed that the orientation of these layers in space is random. The contributions from different orientations are integrated resulting in an effective angle. For lamellar systems showing two-dimensional diffusion and random orientation, the next equation will be used as a correlation function

$$G_o(\tau) = 1 + \frac{1}{N}\left(1 + \frac{\tau}{\tau_d}\right)^{-0.5(1+\cos\theta_m)}\left(1 + \frac{\tau}{K^2\tau_d}\right)^{-0.5\,\sin\theta_m}. \tag{2.16}$$

The effective angle θ_m is the magic angle $\theta_m = \arccos\left(1/\sqrt{3}\right) \approx 54.7°$. This model is referred to as the orientation model. It is based on a single diffusion coefficient. The simulation from the previous chapter is used to find out if Eq. 2.16 is an allowed model for orientation averages. To adapt it to the problem of diffusion in bilayers, the algorithm was modified in three points

1. Two-dimensional diffusion
   The molecules were still distributed randomly on a three-dimensional lattice. But diffusion was restricted to planes only. Lattice steps in vertical direction were excluded. The time step was set according to two-dimensional diffusion, $\Delta t = \epsilon^2/4D$.

2. The excitation profile is given an axis ratio of six to ensure a significant asymmetry.

3. The excitation intensity ellipsoid can be tilted by a user-defined angle.

Because of the elongation, it was necessary to increase the simulation volume to a lattice size of 1024^3. The simulation parameters are listed in Tab. 2.3. A series of 26 correlation functions was

	parameter	symbol	unit	value
setup	laser power	P	mW	2
	wavelength	λ	nm	514.5
	numerical aperture	NA		1.25
	transmission factor	θ_{trans}		0.1355
	focus axis, lateral	w_0	μm	0.3
	focus axis, axial	z_0	μm	1.8
fluorophore	diffusion coefficient	D	m^2/s	2.5×10^{-11}
	exc. cross section	σ_{exc}	m^2	2×10^{-20}
	em. quantum yield	ϕ_f		1.0
	av. no. of mol. on lattice	N		64
simulation	lattice size	L		1024
	lattice parameter	ϵ	nm	5
	simulation time	T	s	4.19
	bin interval	ΔT	μs	1
	angles	θ	$^\circ$	$5 - 85$
internal	time step	Δt	ns	250
	av. no. of mol. in focus	N		0.43140
	concentration	c	M	7.94×10^{-10}
	diffusion time for $\theta = 0^\circ$	τ_0	ms	0.9

Table 2.3. *Parameters for the simulation series to determine the orientation average of two-dimensional diffusion.*

simulated. 20 different angles of the excitation profile reaching from $5, 10, 15, \ldots, 85^\circ$ were chosen in the computations. The resulting intensity traces were summed up with equal weights. After computing the correlation function from this data, the result represents the orientation averaged correlation curve. Additionally, the separate correlation functions for each angle were normalized and then averaged, resulting in a smoother curve. Example correlation for some discrete orientations are given in Fig. 2-6. As expected, the apparent diffusion time increases with the angle of inclination. Values of up to 2.6-fold the definition $\tau_0 = w_0^2/4D$ are reached (see inset of Fig. 2-6). This coincides with the value determined by Weiss [43]. The correlation average from 20 different angles is shown in Fig. 2-7 (*plus* symbols). The average curve resulting from the intensity traces are plotted as *cross* symbols. For comparison, the simulation data are compared to the expected function Eq. 2.16. The simulation data differs slighty from the model. While the (orientation averaged) diffusion time appears to be correctly matched by the model, the shape of the correlation curve shows systematic deviations. In Fig. 2-7, σ was estimated using the result of six simulation runs with equal parameters. The error originates from an inherent dependency $K = K(\theta)$. Further analysis of Eq. 2.16 is necessary and is still being developed. Nevertheless, the model provides to be a reasonable function to describe diffusion in bilayers.

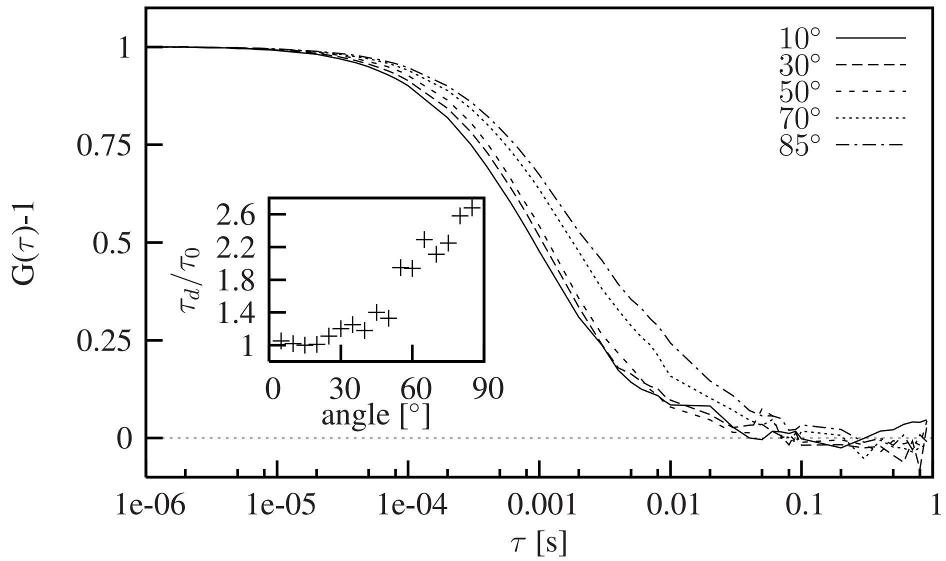

Figure 2-6. *Simulated correlation curves for two-dimensional diffusion under different angles of inclination towards the excitation volume. The inset shows the corresponding diffusion times relative to* τ_0.

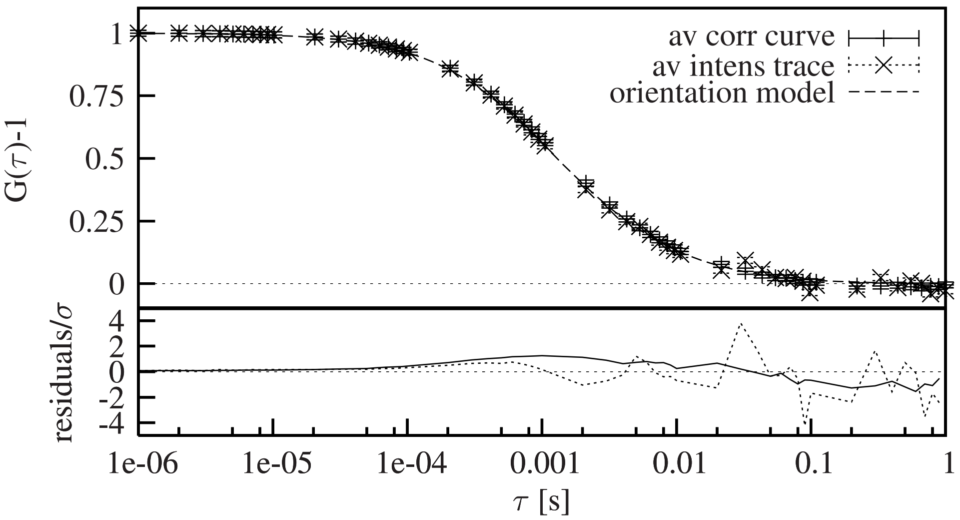

Figure 2-7. *Average correlation curves obtained from simulations with angles between* 5° *and* 85°. $+$ *symbols represent the normalized and averaged correlation curves while* $\times$ *symbols are derived from the superimposed intensity data. The residuals are displayed in units of* σ *which were estimated from separate simulations.*

Chapter 3

Fluorescence detection

The history of Fluorescence Correlation Spectroscopy (FCS) begins in 1955 when the confocal microscope was invented by Minsky [44]. The idea to use the fluctuations of fluorescent molecules transitting through a small observation volume was born in 1974 when Magde and Elson implemented the first concept of FCS [25]. Its application and related methods have quickly progressed since then. Today, there are a variety of microscopes commercially available. Some of them combine Fluorescence Imaging and FCS capability, so that biological specimens can be analyzed at distinct positions.

The experimental part of this work begins with a specification of the laboratory equipment. Three different setups were used. Two of the instruments were assembled in the laboratory. They are part of an ongoing project of building a fluorescence detection system for tracking single molecule motion. The first one, the open microscope setup, is introduced in section 3.1. It is applied for recording fluorescent intensity traces and correlation functions. The main advantage is a positioning unit with a specified accuracy in the nanometer range. The imaging setup, as the second one, consists of a microscope stage which can be equipped with a camera (section 3.2). This system is able to record fluorescent images and save them for subsequent image analysis. The sensor of the camera offers high frame rates and good sensitivity at the same time. The equipment is used to observe the Brownian motion of a single particle in chapter 4. The performances of these systems regarding their optical characteristics are equivalent to commercial systems. The experiments on surfactant bilayer systems (chapter 5), on the other hand, were carried out on a commercial microscope. The setup is described shortly in section 3.3. In this chapter, only techniqual specifications that are necessary for the experiments are discussed. Information about companies can be found in the Appendix A, List of manufacturers.

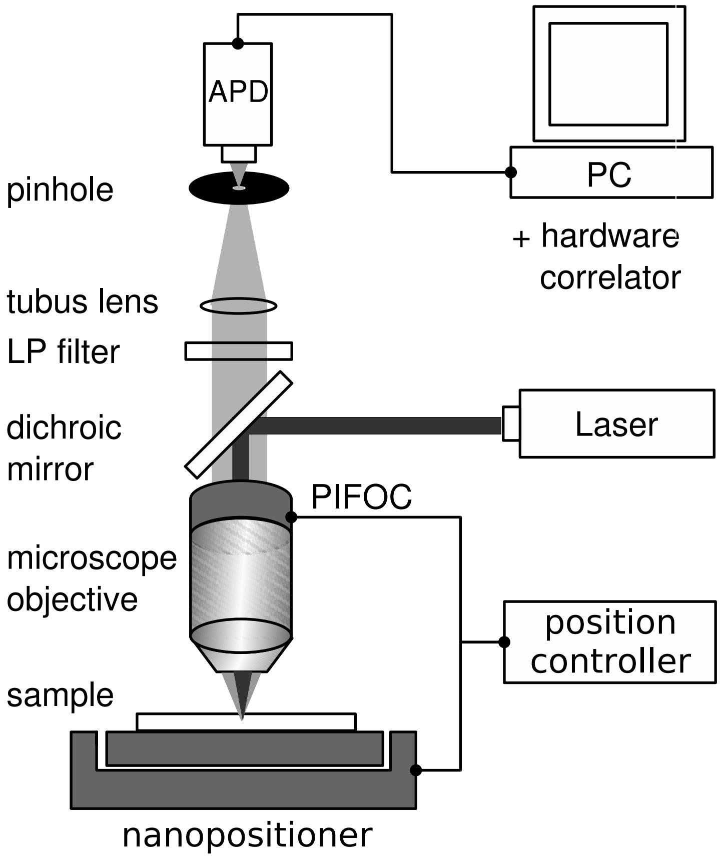

Figure 3-1. *Upright setup of the open microscope. The light from the green laser is reflected by a dichroic mirror and coupled into a high-aperture objective. The beam is focused into the sample. The emission light from fluorescent molecules is collected by the same objective and projected on the detector's sensor by the tubus lens (epifluorescent setup). Excitation light is absorbed by a transmission filter with appropriate filter characteristics. The pinhole reduces the focus extension in the vertical direction. Exact positioning of the sample is possible with two nanopositioners for xy- and z-direction.*

3.1 Open microscope setup

Confocal detection in chapter 4 was performed using an open microscope. The construction of the microscope follows the description given in [42]. In contrast to Fig. 1-10, the setup is in upright position with the microscope objective viewing from top to bottom (Fig. 3-1). The laser is an argon ion gas laser. The output laser intensity is reduced by a dichroic mirror with a transmission of 10% and neutral wedge filters. The experiments were carried out at a laser wavelength of $514.5\,\mathrm{nm}$. The laser worked in the modelocked operation mode at a pulse frequency of $84\,\mathrm{MHz}$. This time scale is smaller than the correlator's sampling time. Thus, the pulse frequency was not observed as an artefact in the correlation curves. The beam profile was not Gaussian because the laser tube suffered from aging effects (Fig. 3-2). The deviation from the optimal profile is a problem for

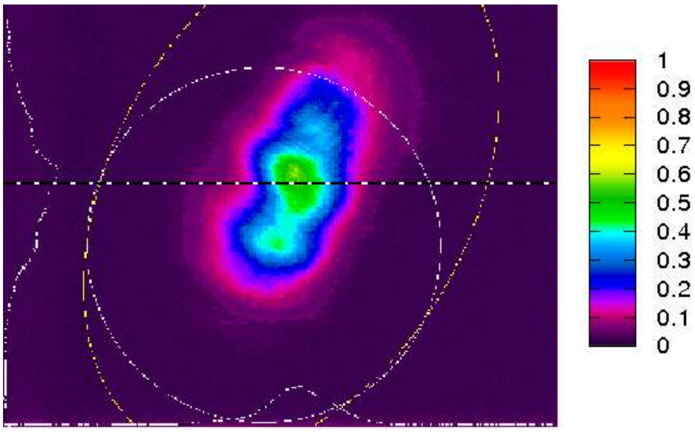

Figure 3-2. *Intensity profile of the Argon ion laser measured with a beam diagnostics system. In modelocked operation, the profile was not Gaussian. The intensity is displayed in a miscolored scale. The graphs at the side of the image represent the projected intensities in two directions.*

absolute concentration determination, but does not perturb the relative measurements presented in this work. There is a dichroic mirror in the beam path that reflects the excitation light and transmits the emission light. The emission light is projected on a pinhole with a tubus lens (focal length $165\,\mathrm{mm}$). The pinhole diameter is $50\,\mu\mathrm{m}$. As a microscope objective either an Apochromat $63\times$ (NA 1.2 Water immersion) or a Plan Neofluar $63\times$ (NA 1.4 Oil immersion) was used. Some properties are summarized in Tab. 1.3. The optional beam expander appearing in Fig. 1-10 was not installed in the open microscope setup. Before a measurement series, the pinhole position was adjusted in horizontal and vertical direction to find the maximum fluorescence intensity. The detection unit consists of an avalanche photo diode with a dead time of $50\,ns$ and a dark count rate of $< 100\,\mathrm{counts/s}$. The photo diode is connected with the TTL input of a hardware correlator. The correlator has a minimum sampling time of $200\,\mathrm{ns}$. A list of manufacturers for all devices is given in the appendix.

Nanopositioning

The position of the focus was controlled by a positioning unit with $3\,\mathrm{nm}$ precision (Fig. 3-3). The unit consists of a table to carry the sample. The positioner is fixed under the objective. The inner frame of the table can be moved horizontally by piezoelectric forces in response to the applied voltage. The maximum amplitude in both directions is $100\,\mu\mathrm{m}$. The vertical position of the objective is controlled by a focus positioner (PIFOC) with similiar properties. It is attached between the objective and the mount.

The overall response time of the positioner including all electronics and interfaces is an important measure to evaluate the suitability for particle tracking. The system's response time was determined in a dynamic measurement [45]. The response time is about $7.1\,\mathrm{ms}$ while performing a Random Walk.

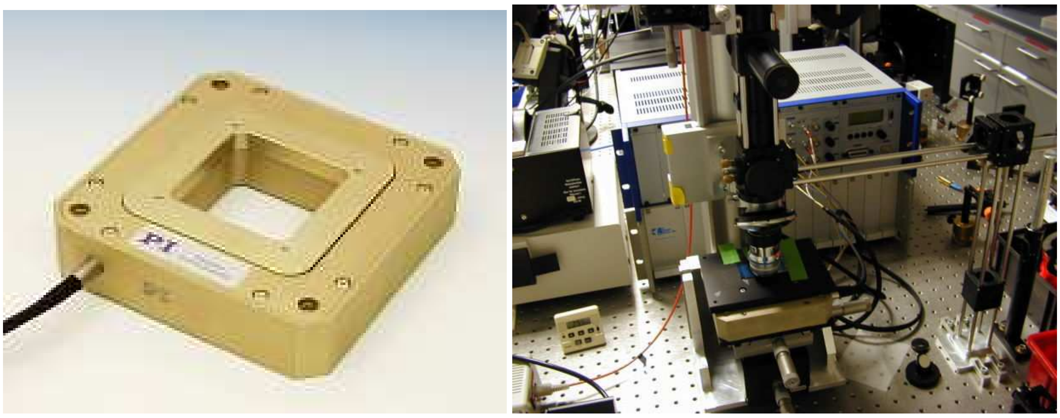

Figure 3-3. *Nanopositioner P-734 (left). Confocal microscope setup with position controller PI-E500 in the background (right).*

3.2 Fluorescence Imaging

The term Fluorescence Imaging subsumes different methods like FLIM (Fluorescence Lifetime Imaging), LSM (Laser Scanning Microscope), and derivates of them. Here, we concentrate on direct detection of fluorescence images with a camera mounted on top of a microscope. Image detection is carried out with the newly built demonstrator microscope (Fig. 3-4 & 3-5). It allows to switch between three different wavelengths and white light illumination. The viewport on top can be equipped with a camera, or a confocal detection unit consisting of a pinhole holder and an optical fiber.

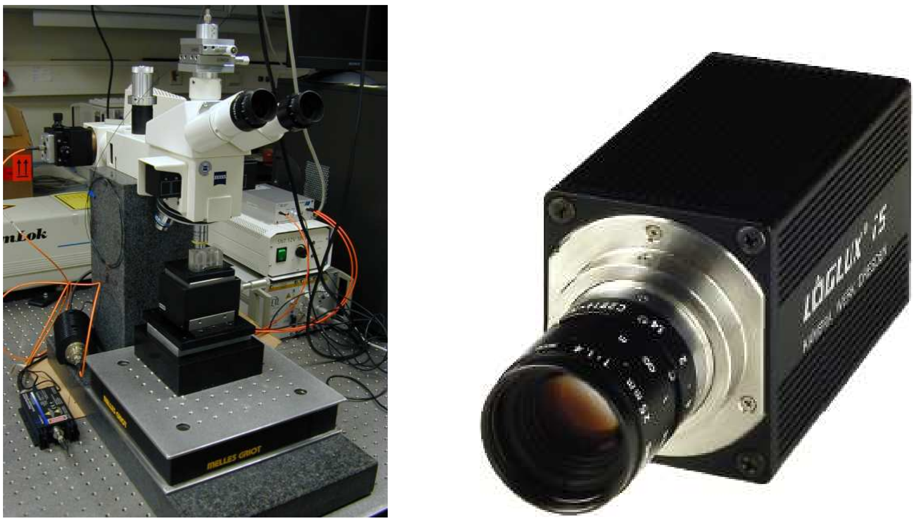

Figure 3-4. *Measurement setup for image detection (left). The pinhole holder on top can be replaced by the camera (right).*

The goal is to develop a detector which is capable of observing single fluorescing molecules over a long period of time. Single molecule detection with spatial resolution puts high demands on the sensitivity of the detector. The basic method of recording images with a camera has suffered

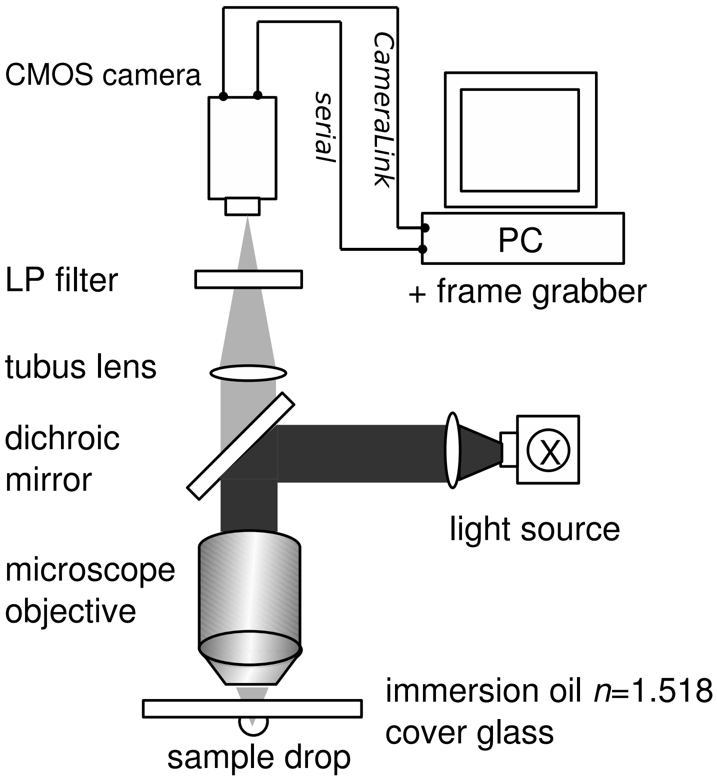

Figure 3-5. *Schematic drawing of the imaging setup.*

from slow readout rates and insufficient sensitivity for a long time. Today, with improvements in CCD and CMOS technology, these problems have been overcome. Recently developed cameras achieve high sensitivity and frame rates at the same time [46].

3.2.1 Camera properties

The camera in Fig. 3-4 is based on CMOS technology. It combines the advantages of high frame rates and good sensitivity. The sensor is a monochrome sensor with a maximum gray scale depth of 10 bit. The readout is controlled by a frame grabber hardware which was installed into a PC. The interface is described in detail in [47].

Resolution

The resolution of a digital camera in real space is given by the pixel resolution divided by the overall magnification of objectives and lenses along the optical detection path. The camera resolution is limited by the pixel size and distance. The CMOS sensor has a sensitive area A of $8.576 \times 6.861\,\mathrm{mm}^2$ at a maximum resolution of 1280×1024 pixel. The pixel size is given by the

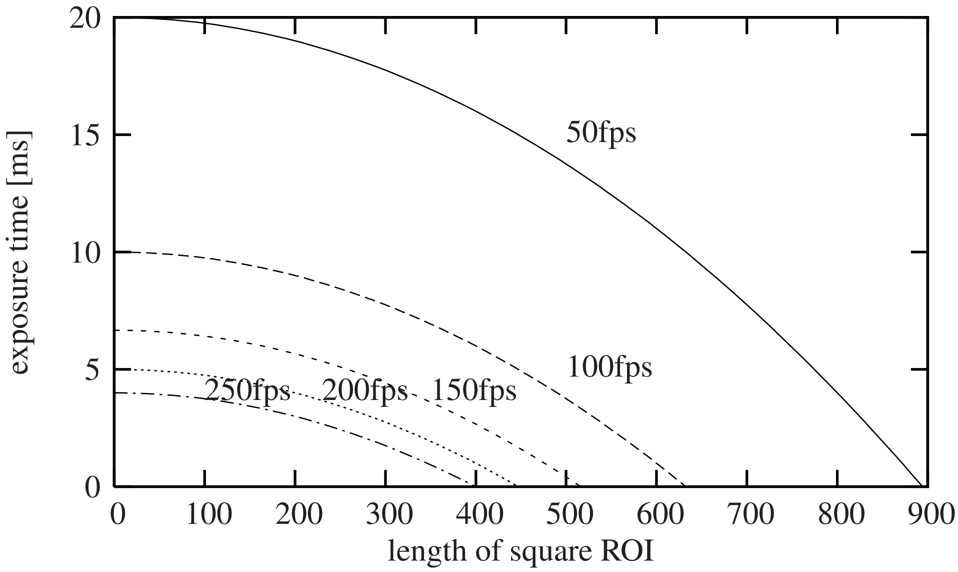

Figure 3-6. *The diagram shows the maximum exposure time which depends on the chosen frame rate, the readout time, and the size of the ROI [47].*

sensor dimensions divided by the number of pixels,

$$A_{pix} = \left(\frac{8.576\,\mathrm{mm}}{1280}\right)^2 = (6.7\,\mu\mathrm{m})^2 \tag{3.1}$$

Including the scale factor $M = 63$ of the microscope objective (Plan Neofluar 63× 1.4 Oil), the theoretical resolution of the camera in real space is $106\,\mathrm{nm}$. This is below the limit of optical diffraction.

Sensitivity

The exposure time/frame can be set according to Fig. 3-6. It depends on the size of the ROI and the chosen frame rate. The manufacturer (*Kamerawerk Dresden*) specifies a sensitivity of $S = 3.29\,\mathrm{V}\,\mathrm{lx}^{-1}\,\mathrm{s}^{-1}$. For practical purposes it is useful to convert to photonic units. The lux is a photometric unit which takes into account the eye's sensitivity function for different wavelengths. The camera manufacturer defines $1\,\mathrm{lux}$ as

$$1\,\mathrm{lux} = 5.56 \times 10^{-3}\,\mathrm{Wm}^{-2} \tag{3.2}$$

integrating the luminosity function over the visual band. In fluorescence measurements, a smaller wavelength band is detected, and thus,

$$1\,\mathrm{lux} = 1.4641 \times 10^{-3}\,\mathrm{Wm}^{-2} \tag{3.3}$$

at $\lambda_{em} = 555\,\mathrm{nm}$ is used alternatively. The light intensity on the sensor can be expressed as

$$I = \frac{W_\lambda}{A_{pix}\,t} = \frac{\mu}{A_{pix}\,t}\,\frac{hc}{\lambda_{em}} \tag{3.4}$$

where $W_\lambda = h\,c/\lambda_{em}$ represents the photon energy. h names Planck's constant, and μ the number of photons. I is inserted into the definition of the sensitivity S

$$S = \frac{U}{I\,t} = \frac{U\,A_{pix}\,\lambda_{em}}{\mu\,h\,c}, \tag{3.5}$$

where U stands for the sensor's voltage output. If the output voltage range of the sensor amplifier is $U_{max} - U_{min}$ is distributed on a 8 bit gray scale (256 values), the smallest voltage difference is

$$\Delta U = \frac{U_{max} - U_{min}}{256}. \tag{3.6}$$

This holds for an amplifier gain of one. The gain can be raised to higher values taking a loss in the signal-to-noise ratio. Inserting the minimum voltage difference $\Delta U = (2.70\,\mathrm{mV}{-}1.59\,\mathrm{mV})/256 = 4.34\,\mu\mathrm{V}$ into Eq. 3.5 and solving for μ, gives the number of photons that are necessary to increase the pixel value by 1:

$$\mu = \frac{\Delta U\,A_{pix}\,\lambda_{em}}{S\,h\,c} \approx 242. \tag{3.7}$$

With this value it is possible to estimate the requirements for single molecule detection. Taking the emission rate of a Rhodamine molecule of $k_{10} = 10^8\,\mathrm{s}^{-1}$ from Fig. 1-8, the number of emitted photons in a $5\,\mathrm{ms}$ frame interval is 5×10^5. A detected pixel value of 60 is assumed to show contrast to the background of ≈ 40. The number of photons which have to be detected on a pixel is $N_{min} = 60 \times 242 = 14520$. Thus, the total transmission factor of the optical setup must be higher than $N_{min}/5 \times 10^5 = 0.03$. This is a reasonable value, which is provided by this equipment.

3.2.2 Single particle measurements

Imaging systems in microscopy offer the possibility to observe many different molecules at the same time. Using different types of fluorophores in different colors, other molecules can be labeled and visualized. This can provide useful information about conglomerates of molecules in natural environments, such as a cell. If the goal is to *localize* a single molecule in an assembly, the microscope's diffraction limit does not prevent a molecule from being detected. If the sensor sensitivity is good enough, single molecules can be observed, yet their position is only known down to half of the emission light's wavelength. The goal of single molecule detection is to distinguish molecules from each other on the basis of their observable properties. It is interesting to determine as many physical properties as possible. Aside from their color, molecules can be identified by other parameters. As an example, the diffusion coefficient can be measured directly by analyzing a molecule's trajectory. This is done by plotting the root mean square distance of the particle against time (Eq. 1.15). By observing a Brownian object over a period of time, the relation can be computed directly from subsequent images. The position of the particle has to be determined from each image. Deviations from the linear relation indicate types of motion other than free diffusion.

It is desirable to observe molecules over long periods of time. Problems occur if the molecule wanders out of the focus plane. This motivates to develop optical or mechanical tracking systems which follow a trajectory in real time. Mechanical tracking can be realized by placing the sample on a positioner which is controlled electronically and coupled to an imaging software. Using a differential approach, the particle's present distance from the central position is determined, and then translated into a control command for the positioner. The imaging setup, the software, and the position controller form a feedback loop. Single molecule detection is possible under certain conditions. The fluorescence quantum yield, exposure time, speed of motion, and the light collection efficiency of the objective must be optimized. It is one goal to find out, if the Fluorescence Imaging setup is suitable for single molecule detection and tracking.

3.3 ConfoCor 2 setup

The setup uses a *Zeiss* ConfoCor 2 inverted microscope with a motorized stage. The objective is a C-Apochromat $40\times$ with a numerical aperture of 1.2, water immersion type. It is equipped with a correction ring for varying cover glass thicknesses. The HeNe laser works at a wavelength of $543\,\mathrm{nm}$. The laser power is reduced to $100\,\mu\mathrm{W}$ by an acousto-optic tunable filter. The detection channel consists of a variable pinhole, which is set to a diameter of $78\,\mu\mathrm{m}$. The fluorescence signal is detected by a built-in avalanche photodiode (SPCM-AQR 13). The emission light passes a long pass emission filter with a cut-off wavelength of $560\,\mathrm{nm}$. A constant temperature in the sample chamber is maintained by an electronically controlled holder. The schematic setup was shown earlier in Fig. 1-10. Further details can be taken from the company's brochure [48].

Chapter 4

Diffusion in microchannels

Liquids in microchannels show laminar flow behavior. This hinders a uniform mixing of reagents because mixing is limited by the laws of diffusion. As pointed out in the introduction, adequate mixing of liquids is an important precondition for chemical reactions in microfluidic systems. In microfluidic flows, the kinetics of chemical reactions are limited because the reactant molecules need some time to find a reaction partner. A quantitative analysis of chemical reactions inside a liquid channel requires characterization of the mixing behavior inside the channel.

For the purpose of establishing enzymatic reactions in microchannels, a Y-shaped mixing channel with two inlets and one outlet was designed and produced. The simple concept of the Y-mixer [49] has the advantage that well-defined conditions exist. There is only one interface between the liquids. The mixing process is predictable. In certain applications this channel geometry is preferable. The fluid channel has a size of only $100\,\mu\mathrm{m}$ which is about the size of a hair. Due to the small dimensions of the channel, the placement of the laser focus is difficult.

The velocity profile of the flow channel is simulated using the Computational Fluid Dynamics software *FLUENT*, and validated by FCS. The results described by Goesch [40] are reproduced. After that, the experiment is carried on further to determine a concentration gradient inside the microchannel. The purpose is to quantify the effect of diffusion limited mixing on the micrometer scale.

4.1 Flow profiles in microchannels

The microchannels are straight channels covered with Borosilicate glass. The glass was attached on the surface by anodic bonding. The channels were etched into silicon wafers with a thickness of $300\,\mu\mathrm{m}$. Pictures of the microfluidic channels are shown in Fig. 4-1. To enable FCS as a method, the water running through the channels contains the fluorescent dye Rhodamine 6G in low concentration. The microchannel is first characterized by determing the velocity profile in the horizontal and vertical cross section.

4.1.1 Setup

The measurement setup was the open microscope shown in section 3.1. A photos of the experiment is depicted in Fig. 4-2. The laser power was $400\,\mu\mathrm{W}$ at first, and later reduced to $100\,\mu\mathrm{W}$ at the rear side of the objective. The Apochromat $63\times$ 1.2 W was used as a microscopy objective. The space between the objective and the microfluidic glass surface is filled by a drop of water acting as an immersion medium. The cross sections are trapezoidal (Fig. 4-3). The width on

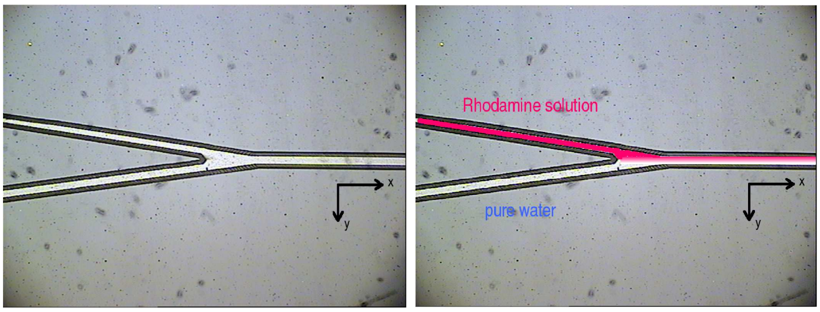

Figure 4-1. *Microscopy image of the Y-shaped mixing channel. The total length of the outlet is $l = 3\,\mathrm{cm}$. When liquids containing different species are fed into the inlets, a liquid boundary separating a concentration gradient is formed (right).*

the upside is $64\,\mu\mathrm{m}$ for the inlets and $100\,\mu\mathrm{m}$ for the outlet. The angle between the walls and surface is $54.7°$. This is a consequence of the silicon crystal's anisotropic (110-) structure. The channels have a constant depth of $40\,\mu\mathrm{m}$. The floor widths of inlet and outlet channels are $7.4\,\mu\mathrm{m}$ and $43\,\mu\mathrm{m}$, respectively. The summed-up cross sections of the two inlets match the outlet cross section $A_{\bigtriangledown} = 2867\,\mu\mathrm{m}^2$ to minimize acceleration of the liquid at the junction.
A constant flow rate F is guaranteed by a syringe pump which maintains a constant pressure on the gastight syringes. The fluid channels and the syringes are connected with flexible polyethylene hoses. The flow rate of the syringe pump can be adjusted in units of volume/time.

Focus positioning

The laser focus can be positioned inside the microchannel by two nanopositioners, one for horizontal, and the other for vertical alignment (Fig. 3-3). The horizontal position can be adjusted by moving the xy-positioner on which the microstructure is attached (see Fig. 4-2). The vertical position is set by moving the microscope objective in relation to the microstructure. The coordinate axes are defined in Fig. 4-1 and Fig. 4-3.
Visual observation of the channel was not possible with this setup. Instead, the position of the walls and the maximum flow velocity can be determined by inspecting the fluorescence intensity trace and the correlation function.

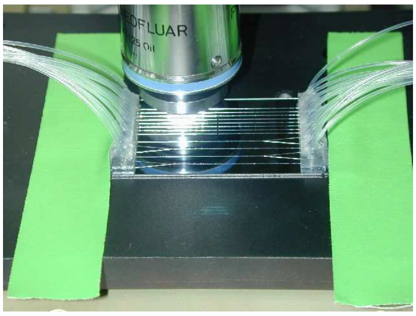

Figure 4-2. *Setup for the flow measurements. Polyethylene hoses are attached to the microfluidic chip and connected to each channel. A drop of water as an immersion medium was applied between the surface and the objective.*

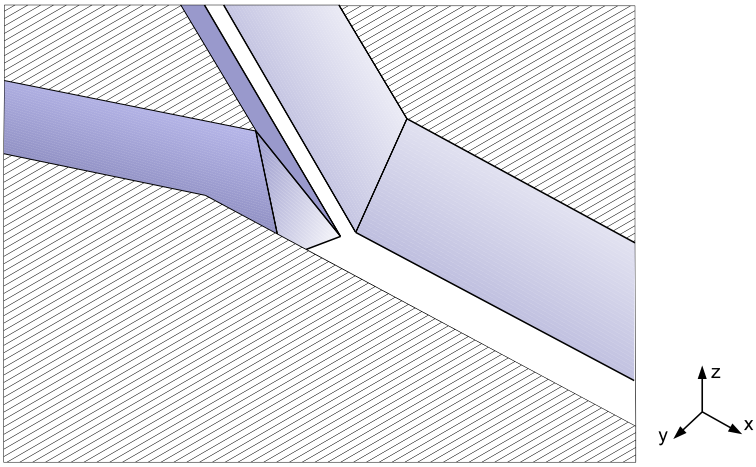

Figure 4-3. *Sketch of the junction between the inlets with trapezoidal cross sections. The top of the structure is drawn in a hatching pattern, while the bottom floor is white. The walls are blue. Direction of view from top left.*

CFD Simulation

The three-dimensional geometry of the microfluidic channel was reconstructed as a grid model in a software specialized on Computational Fluid Dynamics (CFD). Fig. 4-3 schematically shows a clipped drawing based on the grid model of the channel. Subsequently, the velocity profile of running water inside the channels was simulated using a numerical simulation that applies the Finite Element Method (FEM). It is based on a forward integration of the equations of motion for small volume elements. In this iterative calculation the momentum and mass conservation law must be obeyed. The simulation starts with a uniform velocity distribution of $v_{init} = 1\,\mathrm{mm/s}$ over the area of the inlets. The calculation shows that the stream becomes a stationary flow profile after a distance of $0.145\,\mathrm{mm}$. The velocity profile is color coded and visualized in Fig. 4-4. An analysis of the simulation data showed that the cross sectional profiles in horizontal and vertical direction are compliant with the assumption of a parabola. In the strict mathematical sense, the profiles are not exactly parabolic. The influence of the side and bottom walls on the profile cannot be neglected for certain scenarios. Furthermore, a vertical acceleration of the fluid in negative

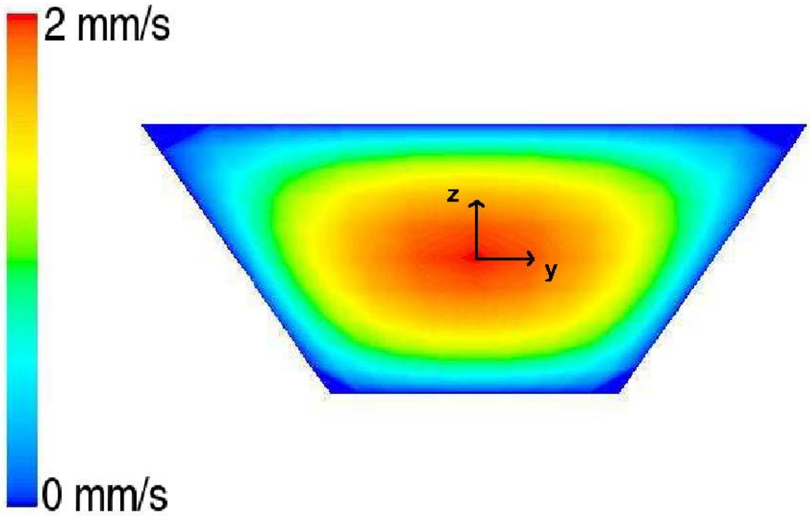

Figure 4-4. *CFD simulation of the velocity profile in the outlet channel. In the stationary profile the central maximum is* $\approx 2\, v_{init} = 2\,\mathrm{mm/s}$ *(by courtesy of Fraunhofer SCAI).*

z-direction occurs at the junction. The reason is the sudden increase in floor diameter. This gives additional room for the liquid at the bottom of the outlet channel. This component is neglected at the point of measurement which is far from the junction ($\approx 1\,\mathrm{cm}$).

4.1.2 Calibration

The focus parameters were determined before the actual experiment. The focus calibration resulted in focus parameters $w_0 = 0.32 \pm 0.01\,\mu\mathrm{m}$ and $z_0 = 3.2 \pm 0.3\,\mu\mathrm{m}$. These values differ significantly from the theoretical calculation in Tab. 1.3. This difference is partially attributed to variations in the glass thickness. The glass layer which covers the microfluidic channels has a thickness of $200\,\mu\mathrm{m}$ which differs from the standard cover glass thickness $170\,\mu\mathrm{m}$. This has a strong influence on the diameter of the laser focus [28]. For comparison, calibrations with cover glasses lead to a smaller value for z_0 of about $2.2 \pm 0.3\,\mu\mathrm{m}$. The non-Gaussian beam profile of the laser (Fig. 3-2) is also expected to contribute to the aberration.

4.1.3 Experimental procedure

The syringes were filled with the same Rhodamine 6G solution in a concentration $< 10^{-8}\,\mathrm{M}$. The flow rate was set to $F = 0.5\,\mu\mathrm{l/min}$ for both inlets. Following from this, the average flow velocity in the outlet is theoretically given by $\bar{v}_{th} = F/A_{\bigtriangledown} = 5.8\,\mathrm{mm/s}$.
The laser focus was placed at a distance of $\approx 10\,\mathrm{mm}$ from the junction. After the channel boundaries had been found, the focus was vertically placed in the center, and horizontally, at a side wall of the outlet channel.

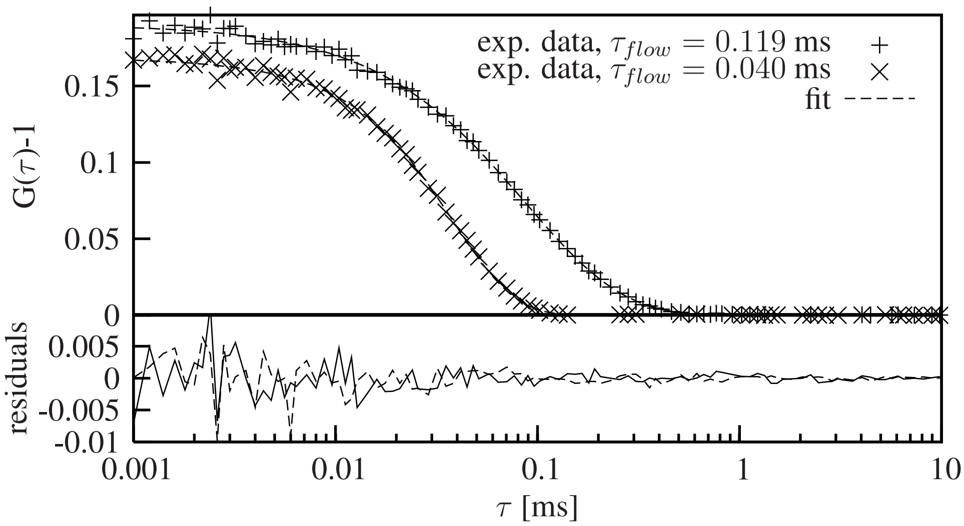

Figure 4-5. *Correlation curves for fast and slow running fluid fitted with model function 1.49. The number of molecules are $N = 5.3$ and $N = 5.9$, respectively.*

After the microchannel and the laser focus had been aligned, a series of $20 - 23$ consecutive correlation measurements of $30\,\mathrm{s}$ each were carried out. The focus position was moved in horizontal or vertical direction from one side to the opposite with a step size of $4\,\mu\mathrm{m}$ ($2\,\mu\mathrm{m}$, resp.) between single measurements.

4.1.4 Analysis and results

The recorded correlation functions were fitted with the FCS equation for combined diffusion and flow, Eq. 1.49. Free fit parameters were τ_{flow} and N. In the analysis, the diffusion constant was kept constant at the literature value of $D = 280\,\mu\mathrm{m}^2/\mathrm{s}$. Example correlation functions are shown in Fig. 4-5. The local flow velocity is obtained by inserting τ_{flow} into Eq. 1.50. The measurement error is determined from Gaussian error propagation. The error of w_0 can be neglected compared to the error of τ_{flow}. Two points of measurement at the sides were excluded because the laser focus overlapped with the wall, and the fluorescence signal was unusable for analysis. The flow profiles were fitted with the parabolic equation

$$v_x(y,z) = \frac{3}{2}\bar{v}\left(1 - \frac{y^2}{d^2} - \frac{z^2}{h^2}\right) \tag{4.1}$$

The origin of the yz-coordinate system is the center of the channel. $\bar{v}$ names the average velocity along the central y_0- or z_0-plane. d and h are the channel's half width, resp. height, in these planes. Eq. 4.1 does not decribe the full velocity profile because the geometry specific boundary conditions are not kept. The FCS measurements show a very good agreement between the measured flow velocity and a parabola fit (Fig. 4-6). The average flow velocity in the z_0-plane section could be determined to $5.60 \pm 0.03\,\mathrm{mm/s}$, and $5.59 \pm 0.03\,\mathrm{mm/s}$ in the y_0-plane. Compared to the theoretical estimate $\bar{v}_{th} = 5.8\,\mathrm{mm/s}$, which was integrated over the total channel area, the values coincide within an error margin of 5%. The channel dimensions resulting from the fits are $87.3\,\mu\mathrm{m}$ for the width (in the z_0-plane) and $41.9\,\mu\mathrm{m}$ for the height. Pretending that the profile was rectangular, and the flow velocity was constant over the cross section, the flow rate through the channel would be $F = 4\,h\,d\,\bar{v} = 1.23\,\mu\mathrm{l/min}$ exceeding the expected value by 23 %. Due to slight misalignment the width comes out too big compared to the true value of $d = 71.5\,\mu\mathrm{m}$ in the central plane. The height agrees well with the given value from the production process. The results confirm that flow profiles can be determined with high precision inside microchannels.

4.2 Diffusion limited mixing

Besides dynamic properties, like the average time of molecules flowing through the laser focus, FCS also provides information about the concentration of fluorescent molecules in the solution. This experiment is an extension of the previous. We expect to see the equalization of a substance along a concentration gradient in streaming water. Fluid dynamics predict laminar behavior of the fluid. The absence of any convection or turbulence allows to observe undisturbed diffusion. Again, the measurement was set up according to Fig. 4-1 and Fig. 4-2. The concentration gradient $\partial c(x, y, z)/\partial y$ levels off along the flow direction.
In the following, the dependence of $c(y \mid x_0 = 1\,\mathrm{cm}; z_0 = 0\,\mathrm{cm})$ on the y-coordinate in the center of the channel is determined. It is difficult to chose two distant measurement positions in the outlet channel without misaligning the chosen vertical plane of measurement. Instead of moving the channel along the x-coordinates, the flow velocity was changed. This simplifies the experiment greatly.
The flow in x-direction and the diffusion process are perpendicular to each other. They are competitive in the sense that one process can be dominant depending on the average flow velocity. The lower limit of the flow velocity, below that diffusion is the dominant process, can be estimated by the channel dimension and the diffusion coefficient of the dye molecules. With Eq. 1.15, the average time for a Rhodamine molecule to propagate across the half width d of the channel becomes $\bar{t} \approx d^2/6D = 3\,\mathrm{s}$. Dividing the length of the channel behind the junction by this value, the minimum flow velocity for observing diffusive mixing is $v_{min} > x_0/\bar{t} = 3.3\,\mathrm{mm/s}$.

CFD Simulation

The mathematical treatment of the mixing problem, as it appears in this experiment, cannot be solved analytically. The calculation presented in section 1.1.4, Eq. 1-4, is valid only for

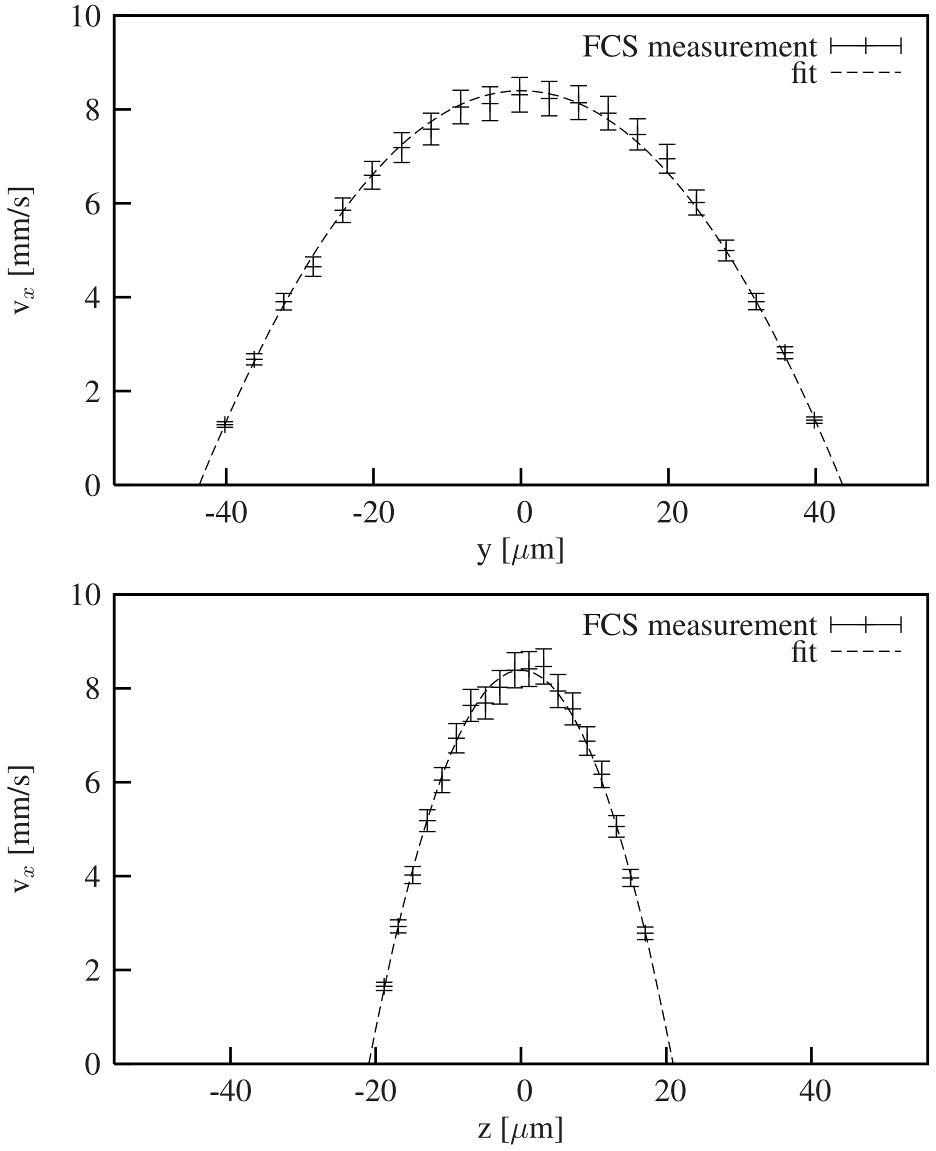

Figure 4-6. *Flow velocity along the y-direction (top) and the z-direction (bottom) across the central planes z_0 and y_0 of the microchannel. The error bars are given by the error of the fitted parameter τ_{flow}.*

liquids at rest. It can serve as an analytical approximation at most. Here, a concentration boundary and a flow profile appear simultaneously. The problem is three-dimensional (instead of one-dimensional) and additionally, reflecting walls restrict the channel on four sides.
This problem can again be solved with the help of the numerical CFD simulation. Diffusion processes are not automatically accounted for. The calculation of diffusing molecules in high dilution cannot be realized by the FEM alone. It is realized by an additional simulation step using a species transport model. In this model, the fluorophore solution is defined as an equivalent liquid with properties partially matching those of the Rhodamine molecule. The dynamic viscosity of this equivalent liquid is chosen eight times higher than the viscosity of water. This is according to the diffusion coefficient ratio of water and Rhodamine molecules. The mass fraction of the equivalent liquid was chosen as $1/1000$. Thus, the overall viscosity of the simulated liquid does not differ from water. The details about the simulation are explained in the project report [50].
The result of the CFD simulation including the species transport model is depicted in Fig. 4-7. Fig. 4-8 shows the according cross sectional distributions from the central plane. At a flow velocity of $v \approx 2\,\mathrm{mm/s}$ in the center of the channel, the Rhodamine is evenly distributed after $\approx 9 - 10\,\mathrm{mm}$. Theoretically, a value of about $v \times \bar{t} = 6\,\mathrm{mm}$ was expected (cp. introduction to this section). To observe the concentration step in an experiment, a higher flow velocity should be chosen than in the simulation.

4.2.1 Calibration

Again, the focus parameters were determined before the experiment. Values of $w_0 = 0.317 \pm 0.003\,\mu\mathrm{m}$ and $z_0 = 3.2 \pm 1\,\mu\mathrm{m}$ were obtained.

4.2.2 Experimental procedure

One syringe was filled with pure water, the other one with the Rhodamine 6G solution ($c < 10^{-8}\,\mathrm{M}$). The flow rate was adjusted to $F = 0.5\,\mu\mathrm{l/min}$ in both inlets. The microchannels were then carefully filled with both solutions. At the junction, a boundary of two adjacent liquids is formed and molecular exchange is enabled. The system was left alone for several minutes until diffusion and flow have became stationary at constant rates. The laser power was $100\,\mu\mathrm{W}$ in this experiment.
Then, 28 correlation measurements were carried out across the channel center. As a compromise between total measurement time and data quality, the duration for one curve was 45 s. In between measurements the laser focus was moved $3\,\mu\mathrm{m}$ further along the y-axis. For comparison, the flow rate was increased to $F = 2.0\,\mu\mathrm{l/min}$ in both channels. The measurement was repeated at the

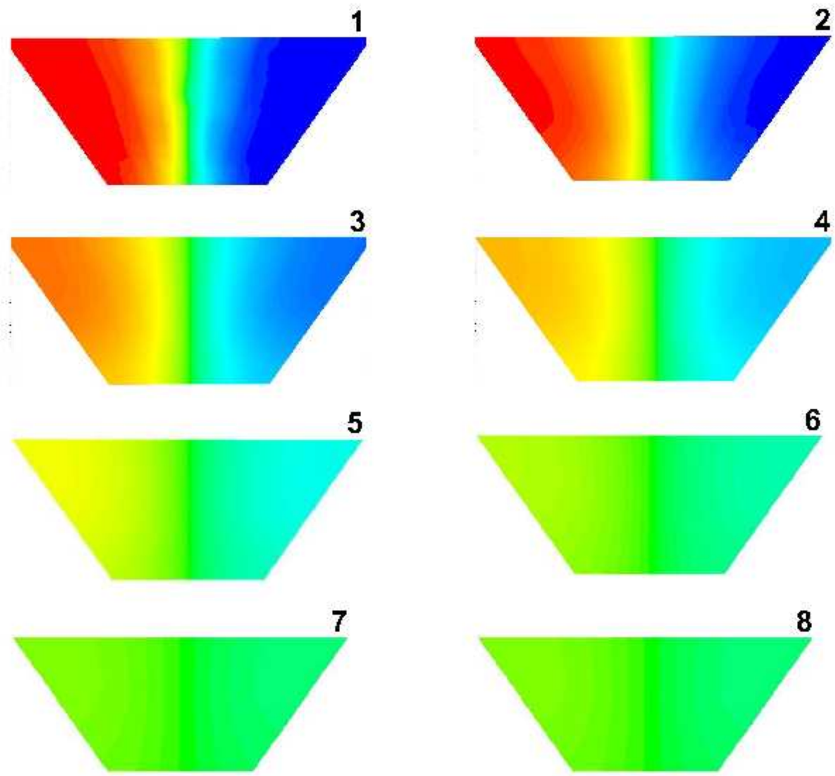

Figure 4-7. *CFD simulation of diffusive mixing in the Y-shaped microchannel. The images are cross sections taken at distances* 0, 0.1, 0.5, 1, 2, 3, 4, *and* 5 *mm from the junction (image by courtesy of Fraunhofer SCAI).*

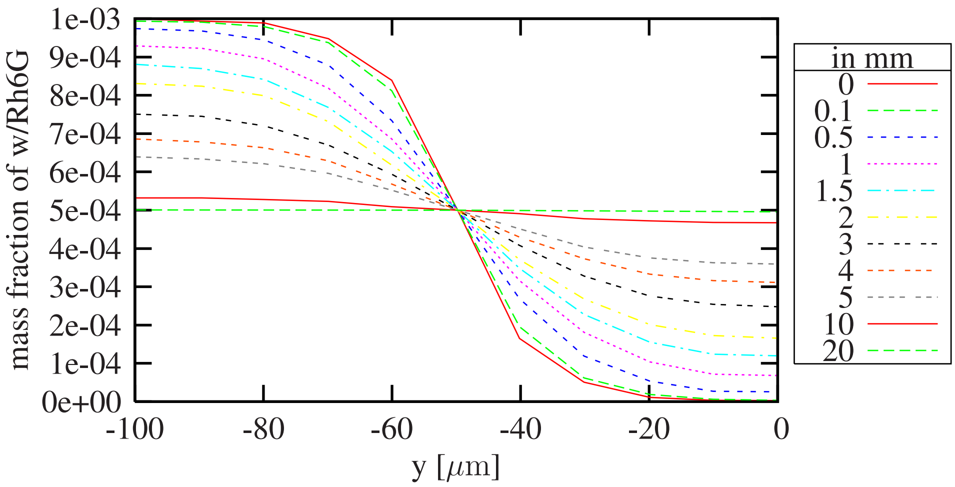

Figure 4-8. *CFD results for the central concentration distribution across the outlet cross sections. The curves represent concentration distributions along the y-axis in the center of the channel. The distance from the junction is given in the legend (image by courtesy of Fraunhofer SCAI).*

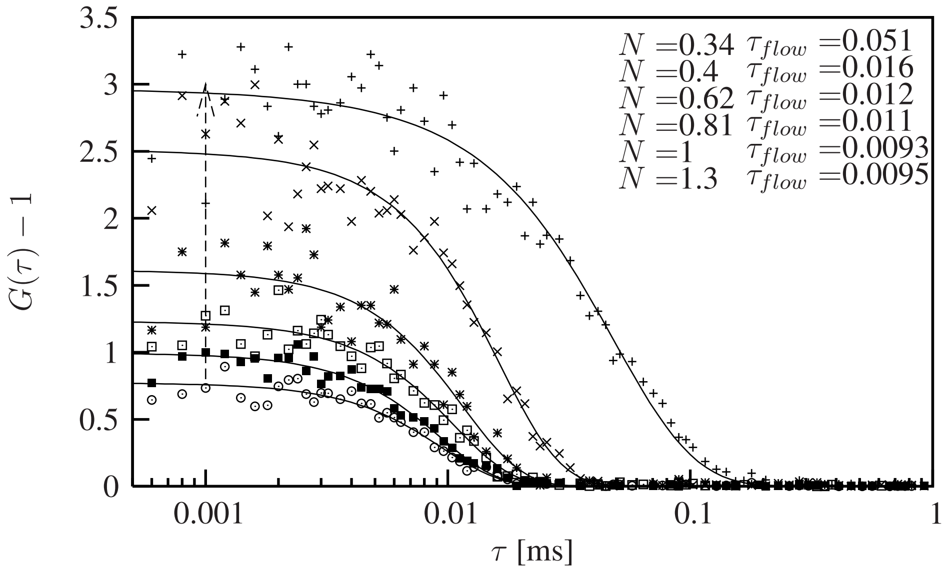

Figure 4-9. *Correlation data from the mixing experiment. Straight lines are best fits. The arrow points in direction of decreasing concentration.*

same positions. It is expected that the dye concentration in one half of the channel is lower at the higher flow rate.

4.2.3 Analysis and results

As in the previous experiment, the correlation functions were fitted to Eq. 1.49 with free parameters N and τ_{flow}. Some correlation curves are shown in Fig. 4-9. The data from three measurement positions at the sides were excluded from the analysis because the measurement was disturbed by unpredictable optical effects originating from focus overlaps with the side walls. The local fluorophore concentration at the chosen positions was determined for the low and for the high flow rate. The uncertainty in concentration is given primarily by the standard deviation of the correlation function. Koppel's theoretical expression, Eq. 1.43, was applied resulting in a value of about 10 %. Only for absolute concentration measurements the error in the observation volume must be taken into account.

Figure 4-10 shows the measured Rhodamine concentration gradient along the profile of the microchannel. Additionally, the velocity profiles are depicted in the top diagram. The concentration values are given in arbitrary units (a. u.) on the left, and in $\mathrm{mol/l}$ on the right axis. The latter follow from the calibrated focus parameters. They should not be regarded as absolute values because the open microscope setup does not provide true concentration determination without information about the function $MDE(\mathbf{r}, z)$.

The fall-off in concentration along the y-axis is significant at the higher flow rate. At the low flow rate, the concentration is almost constant across the channel. Subsequently, Eq. 1.13 was fitted

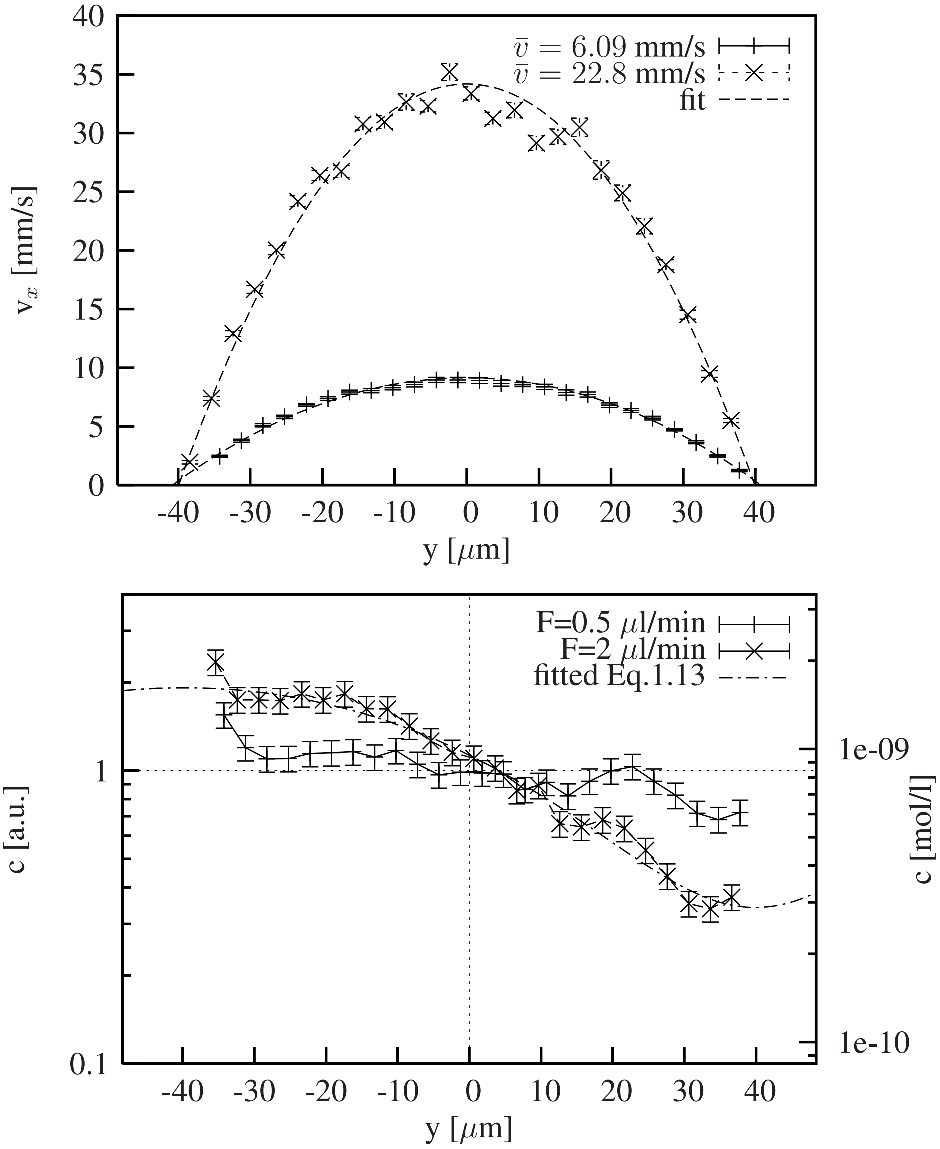

Figure 4-10. *Velocity profiles in the outlet channel for high and low flow rate (top). Distribution of Rhodamine 6G fluorescent dye in the microchannel at two different flow rates (bottom). The concentration data for the higher flow rate was fitted to Eq. 1.13 (fit parameters $c_0 = 2.3$, $t = 1.4\,\mathrm{s}$).*

to the values for the higher flow rate including terms of fourth order. This approximate equation describes the data surprisingly well. However, the fitted time parameter $t = 1.4\,\mathrm{s}$ is much larger than the average flow time from the junction to the point of measurement. Ignoring the fact that the model is not strictly valid, this result indicates that the mixing is more efficient than expected. The experimental data is not precise enough to allow for a better quantitative comparison with the simulated concentration distribution. Qualitatively, the theoretical approximation by Eq. 1.13 and the CFD simulation are both confirmed.

To improve the accuracy of the data, several correlation functions can be averaged at each position. This requires a considerably longer measurement time. As an additional measure of the local concentration, the average fluorescence intensity can be taken into account. In the low concentration range, the mean fluorescence intensity is proportional to the dye concentration. Further improvement can be reached by establishing well-defined conditions of the laser focus. The glass layer thickness has to be changed to $170\,\mu\mathrm{m}$. The beam profile can be optimized by using a different laser.

4.3 Particle tracking

As was shown in the previous sections, the detection of fluorescent molecules in solution gives information about local and dynamic properties like the molecule concentration, the flow velocity, or the diffusion coefficient. However, sometimes the relevant information is hidden due to averaging over a large number of molecules. Despite the single molecule sensitivity of a confocal microscope, the FCS method requires to observe a molecule ensemble to determine properties of a molecule species from the intensity trace. In contrast to that, it is advantageous to determine properties of single molecules, e. g. in intracellular measurements. If fluorescence labeled molecules can be distinguished from each other, certain cell functions could be revealed easier.
One goal of single molecule detection (SMD) techniques is to track a single molecule trajectory and to determine specific parameters during observation [46, 51]. Thus, new information can be obtained considering that the results are subject to fluctuations. For a detailed discussion of the significance of single molecule measurements see e. g. [52]. In this section, the principle of single molecule measurements is shown in vitro using a micrometer sized particle. This has the advantage of a high signal-to-noise ratio and slow particle motion. The setup for video microscopy is introduced for this purpose.

4.3.1 Experimental procedure

Image detection was realized using the microscope setup described in section 3.2. The solution was prepared by diluting a stem solution of fluorescent microspheres by a factor of 100. A hanging drop was applied to the surface of a cover glass and put under the objective. The microscope objective was a Plan Neofluar $63\times$, 1.4 Oil immersion. White light was used for illumination because the parallely installed (blue) laser did not match the excitation spectrum of the fluorescence dye. The particle was observed for $20\,\mathrm{s}$ at a frame rate of $50\,\mathrm{fps}$. The exposure time was $8\,\mathrm{ms}$/frame. The digital film was recorded in the AVI file format.

4.3.2 Analysis and results

After recording, 1000 images were captured from the film and converted into ASCII files (using the conversion utility of the *MPlayer* software). A short program was written to find the pixel coordinates with maximum gray value in each frame of the film. The background pixel value was ≈ 40 on the average, while the particle intensity reached a maximum of 123. The pixel with highest intensity in each frame was assigned to the particle's center position. The time interval was given by the inverse of the frame rate $50\,\mathrm{fps}$. The trajectory in two dimensions was reconstructed from the 1000 coordinates (Fig. 4-11).

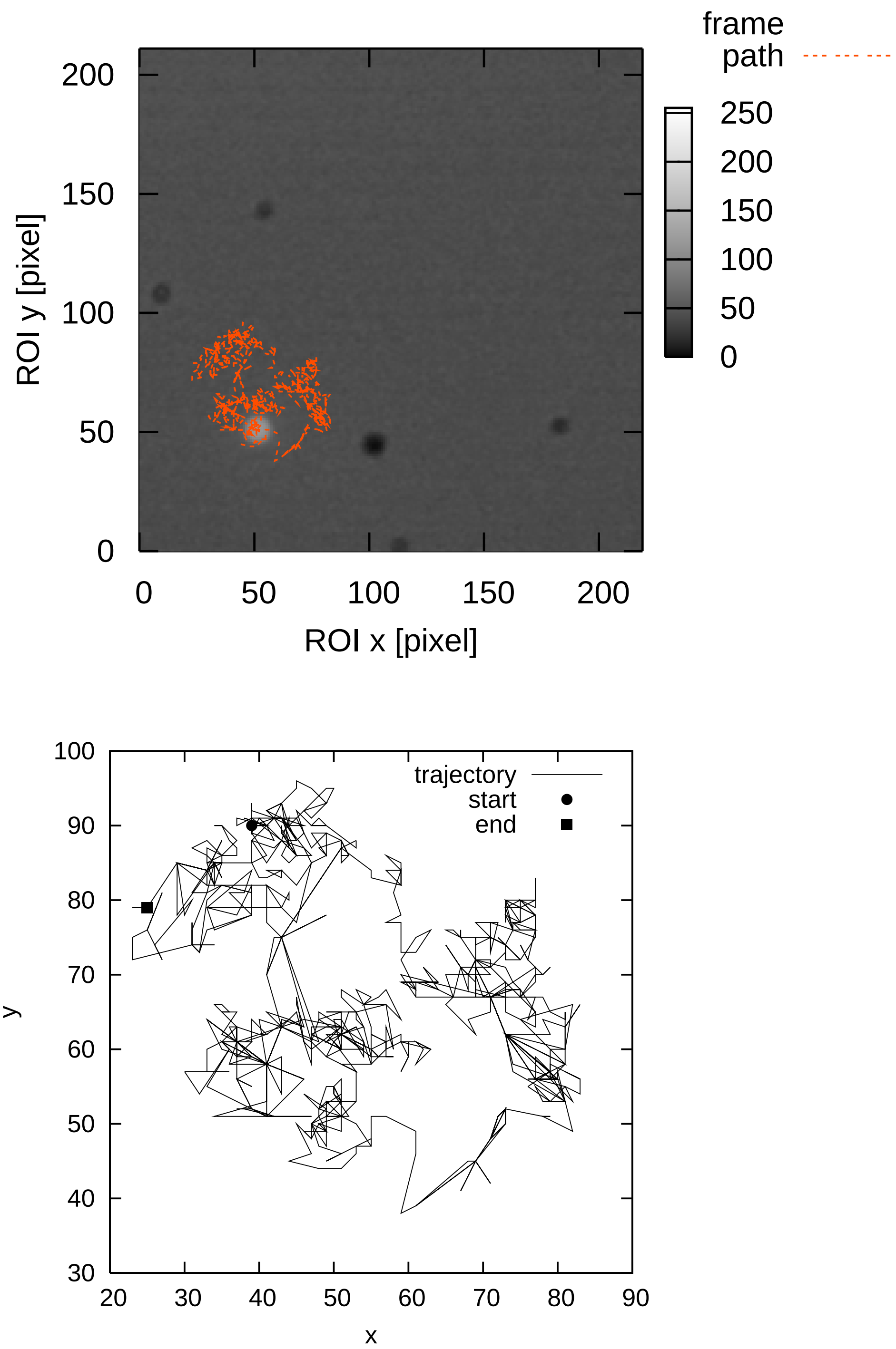

Figure 4-11. *Captured frame from the film of a diffusing particle. Black dots in the image are dirt on the objective or optical filter. The microsphere's trajectory is drawn in the image plane (top) and separately as a graph (bottom).*

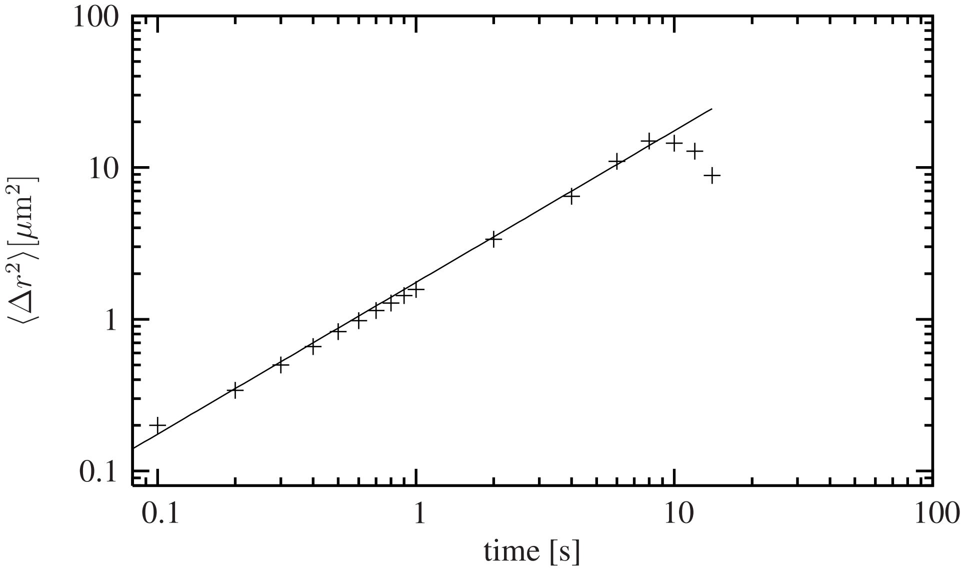

Figure 4-12. *The mean square distance for the path of the particle shown in Fig. 4-11. The diffusion coefficient is determined from the slope of the linear fit between* 0.1 *and* $6\,\mathrm{s}$.

In case of a Brownian motion, the mean square distance from an arbitrary starting point is proportional to time (Eq. 1.15). When the mean square distances are computed from the coordinates of the particle, its diffusion coefficient can be determined. The microsphere motion in Fig. 4-11 supposedly conforms to a free particle. Fig. 4-12 shows the linear relation between $\langle r^2 \rangle$ as it was determined from the particle path. D is obtained from the slope of the linear fit between 0.1 and $6\,\mathrm{s}$,

$$D = \frac{\langle \Delta r^2 \rangle}{4\,\Delta t} = 0.445\,\mu\mathrm{m}^2/\mathrm{s}.$$

The expected diffusion coefficient $D_{1\mu} = 0.429\,\mu\mathrm{m}^2/\mathrm{sec}$ for a particle with a diameter of $1\,\mu\mathrm{m}$ is known from Eq. 1.16. Theoretical and experimental value agree very well within an error margin of $5\ \%$. The hypothesis that the particle motion is Brownian can be accepted. Deviations from the linear relation occur after $10\,\mathrm{sec}$. Apparently, the particle performed a path returning close to its starting point.

Conclusion for mechanical tracking

The experiment shows that the diffusion coefficient for a single particle can be determined with good precision. For this particle and framerate the time that is necessary to determine D can be reduced theoretically to about half a second. This is considerably shorter than in FCS. To follow the trajectory of the particle mechanically in real time, the response time of the nanopositioner has to be considered. The response time of $7.1\,\mathrm{ms}$ is known from a dynamic measurement. The step size can be assumed to be at the limit of the optical resolution. The highest diffusion coefficient which could be followed is then $D_{max} \approx 2\,\mu\mathrm{m}^2/\mathrm{s}$. In this case, the camera and image processing software must work at a frame rate of $150\,\mathrm{s}^{-1}$. Mechanical tracking of small molecules in aqueous solution is still out of reach in this concept. However, tracking of particles bigger than $100\,\mathrm{nm}$, or tracking of single molecules in media with higher viscosity, seems to be a realistic goal.

4.4 Discussion

In section 4.1 and 4.2, the laminar flow profile and the properties of a microfluidic mixing channel were examined. The experimental velocity profiles agree well with the classic equations for laminar flow in such devices.
Mixing of an initially uneven concentration could be observed. Differences in local concentrations inside a microchannel were successfully detected. The concentration gradient can be adjusted by changing the flow rate. Diffusion due to Brownian motion appears as the only source of mixing inside the channel. There is no evidence, that other effects contribute to better or worse mixing. The measurement data agree well with predictions from the CFD simulation. Analytical expressions for complex geometries in three dimensions do not exist. Simple analytical calculations give qualitatively good estimates. Numerical simulations help solving the problem for special cases with a precision only limited by computational power. For a quantitative comparison, the measurement precision must be improved. Repeated measurements at the same positions reduce the stochastic error as mentioned in section 4.2.3. The optical properties of the cover glass have to be adapted to the standard of $170\,\mu\mathrm{m}$ in microsopy. This type of glass requires very careful handling during the bonding process and is rarely used. Theoretical focus calculations which include the refractive indices of the material along the beam path can also contribute to higher precision.
The experiment shows that uniform mixing is quickly reached in the $100\,\mu\mathrm{m}$ channel at low flow rates. Nevertheless, for the purpose of observing biochemical reactions in a continuous flow, the Y-channel mixer has a disadvantage. At high flow rates, the medium has left the microchannel before uniform mixing has been reached. In low concentrations, the time for the initiation of enzymatic reactions in the outlet channel might be too short. However, as the sensitivity for detecting single molecule transitions is given, there is still a chance that the Y-channel mixer can be used as a reaction chamber for continuous flow systems. In this case, fluorescent switches as sensor molecules can be applied. A four component system consisting of Amplex UltraRed (*Invitrogen*), glucose oxidase, glucose, and horseradish peroxidase (HRP) was tested in small sample drops and in microfluidic channels. Amplex UltraRed separates the fluorescent dye resorufin upon the reaction with H_2O_2. The latter is a reaction product of the enzymatic reaction between glucose oxidase and glucose in the presence of HRP. The reaction kinetics were analyzed according to the Michaelis-Menten theory for enzymatic reactions. Confocal intensity measurements showed that the reaction is initiated even below micromolar concentrations of glucose. For even lower

concentrations, single molecule events have to be counted and discriminated from the background using one of the SMD techniques. For the analysis of single molecule reaction data, the fluorescence intensity signal has to be interpreted in an appropriate way. Stochastic methods based on information from the photon counting histograms (PCH) of the fluorescence signal are promising tools which are presently being developed [53].

The problem of mixing on the microscale has been approached earlier. Most suggestions are based on the idea to multiply the area of contact between the two liquids. This can be achieved by intersecting and recombining the stream [54, 55]. Other methods rely on chaotic mixing [56]. In both cases, the experimental realization is not easy because complicated flow geometries have to be produced. Especially for the chaotic mixer, another disadvantage is the unpredictable molecule distribution after the mixing stage. Through the mixing process chemical reactions are accelerated, but the internal conditions do not reach a completely homogeneous distribution. Nevertheless, in very low concentrations, a 'homogeneous' destribution of a molecule species does not exist. Statistical fluctuations of the local concentration dominate the molecular distribution as pointed out in section 1.1.1. These remain an important factor and must be taken into account in theoretical calculations as well as in experiments. The necessary measurement time and the significance of the result is affected thereby [52]. New numerical simulations that combine reaction kinetics, diffusion, and liquid flow would contribute to the development of microreaction devices with predictable properties.

For the purpose of measuring flow profiles, other methods are available. Two methods called double-focus fluorescence cross correlation, and Particle Image Velocimetry (PIV) have been successfully applied to fluidic channels [57, 58].

4.4.1 Outlook: Real time image processing and 3D molecule tracking

Real time image processing of a single molecule observation demands the experimental conditions to be improved. Because of the low fluorescence yield from a single molecule, especially the background noise has to be reduced. Laser irradiation instead of white light is recommended. Furthermore, the exposure time must be optimized to gain a sufficient number of photons/pixel, and, at the same time, the frame rate has to be high enough to keep track of the molecule position. Regarding the sensitivity of the CMOS camera, which was calulated in section 3.2, single molecule detection should be a reachable goal. To realize a tracking system, the position detection has to be processed in real time [42, 59]. There are several algorithms for detecting the center of a particle's position to be tracked in fluorescence images data. An efficient approach which can be realized in FPGA hardware (Field Programmable Gate Array) was suggested by Lueghausen [47]. Position control has to be connected to the software to receive the coordinates with a shortest possible delay. Generally, three points have to be considered:

1. Constraints have to be given for the maximum amplitude of the positioner in every direction to prevent it from damage.

2. The mechanical precision is higher than the optical resolution of a light microscope. In biological cells, some relevant structures can be much smaller. Single molecule tracking does not improve resolution.

3. Photobleaching limits the time for observation in the case of molecules.

Tracking in three dimensions suffers from another problem, that is the molecule's vertical direction of motion. Due to the optical symmetry along the beam axis, the up- and down-direction cannot be distinguished from each other. Different solutions to this problem were proposed. One is to operate the objective nanopositioner in a scanning mode. The PIFOC performs an oscillation around the molecules present position. The zero point has to be adjusted as soon as a change in the molecules vertical position has been detected. This requires a rather complicated computational and piezomechanical effort and slows down the tracking performance. There is a method available for nanoparticles which is based on analyzing the fraction of forward scattered light [60]. A different approach is a wedge prism located at the back focal plane. The idea was presented by Mizutani [61]. The prism separates the fluorescence image into two halfs. Hereby, an optical asymmetry is introduced into the detection path. The molecule's vertical direction of motion can be distinguished from each other by the asymmetric intensity distribution on the detector.

Chapter 5

Diffusion in surfactant bilayers

The preceding chapter 4 focussed on molecular motion in structures with micrometer expansions. It was shown that, on this scale, fluids and molecules act consistently with the classic theories. When diffusion is observed on a nanoscale, additional phenomena emerge. In this chapter, diffusion experiments are carried out to measure the dynamics inside supramolecular structures. The size of the observation volume in FCS, as it is used here, is fixed. Instead, scaling to the nanometer range can be achieved by reducing the size of the observed physical system. The examination of nanostructured environments can bring out new information about molecular interaction. In this chapter, the diffusion coefficient – as a measure of mobility – is determined for binary systems composed of surfactant/water emulsions in different mixing ratios. The mixtures of lipid and water form a micellar and a lamellar phase. Additionally, the influence of a third substance is investigated (cholesterol). In a ternary systems, structural changes can occur. Fluorescent molecules are added to the lipid bilayers to probe these changes. The presence of cholesterol is expected to have an influence on the molecular mobility. The obtained results affect the related field of Cell Biology, as a major part of it deals with diffusion in the cellular membrane.

5.1 Introduction

In eukaryotic cells, the plasma membrane is mainly composed of glycerophospholipids, sphingolipids, and a sterol. The amphiphilic structure of the lipid molecules results in the formation of a bilayer membrane. For their function, cells need an exchange of molecules and ions with their surrounding through the cell membrane. The knowledge of how these transport processes are controlled by the cell are important, e. g., for the development of pharmaceuticals. The fact that the composition of the cell membrane is maintained by intracellular functions suggests that it is a key factor for the cell's life cycle and communication. Especially the cholesterol and lipid content of the membrane play an important role for the regulation of protein transport inside and outside the cell [62]. Cholesterol within the membrane has an influence on the molecular order by

hydrophobic and steric interaction [63, 64]. The purpose is to quantify the effect that cholesterol has on the properties of surfactant membranes.
Mechanical properties of cell membranes as well as the exchange of matter through the membranes depend strongly on the diffusion of lipid molecules inside the membrane. To study diffusion in membranes, several methods have been used. Light scattering and NMR methods provide high precision due to averaging over large ensembles of particles. On the other hand, when diffusion on small scales with few or even single molecules shall be observed, fluorescence microscopy methods provide a better way to determine more interesting properties. For this study, Fluorescence Correlation Spectroscopy (FCS) was chosen as an experimental technique offering the advantages of small sample volumes and short measurement times.
Because of the similarity between the lamellar phase of surfactant/water emulsions and the biological cell membrane they have been considered as simplified model systems for membranes. Adding other substances to the system can also affect the phase transitions and the properties of the individual phases. Cholesterol is an ingredient in natural membranes. Because its fraction in the total lipid content varies among different cell types, its function is not completely clear. Here the effect of cholesterol on a surfactant/water system, in particular the lamellar phase, is studied. By using a surfactant/water model, the fundamental influence of cholesterol incorporated in bilayers is examined. In contrast to lipids of biological membranes, the chosen surfactant consists of a headgroup and a single saturated dodecyl chain. The molecular order of the system is simplified compared to biological membranes composed of a variety of complexer lipids. It is shown that cholesterol does not reduce diffusional mobility in complex structures only, but in basic lipid assemblies as well.

5.2 Membrane system

5.2.1 Components

$\mathbf{C_{12}E_5}$ As a model membrane, the system $C_{12}E_5$/water was chosen. The lipid pentaethylene glycol monododecyl ether ($C_{12}E_5$) is a non-ionic surfactant with a molecular weight of $M = 406.6\,\mathrm{g\,mol^{-1}}$. For the molecule length values from 22 Å to 26 Å [66, 67] were reported. The critical micelle concentration for $C_{12}E_5$ is $64\,\mu\mathrm{M}$ at 25°C [68]. As can be seen in the diagram (Fig. 5-1), the emulsion of $C_{12}E_5$ and H_2O shows different phases depending on the surfactant concentration and temperature.

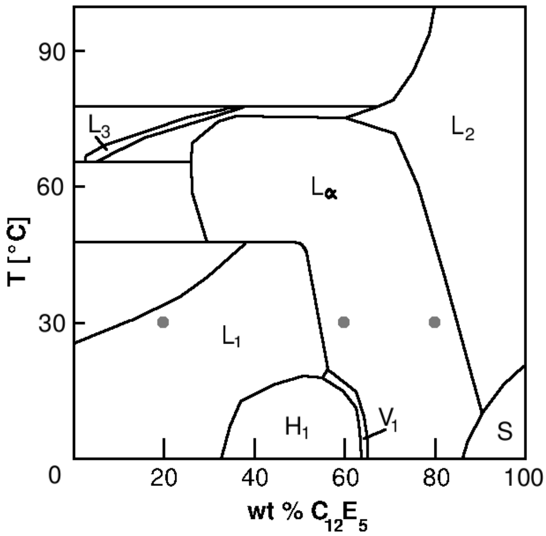

Figure 5-1. *Phase diagram of $C_{12}E_5$ and H_2O. L_1 and L_α denote the micellar and the lamellar phase, respectively. H_1 is the hexagonal phase, L_2 and S the inverse micellar and the solid phase. V_1 is the cubic phase. L_3 is a sponge phase. Unnamed areas are bicontinuous. The gray dots mark the systems that were measured. The image was redrawn from [65].*

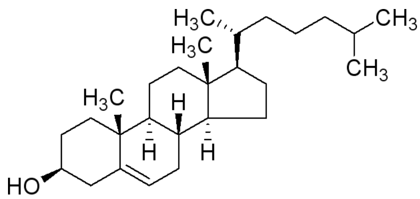

Figure 5-2. *Chemical structure of cholesterol.*

R18 The use of a fluorescent marker molecule is required to detect light from the transparent system. For this purpose, the fluorophore octadecyl Rhodamine B (R18) was chosen ($D = 420 \times \mu\mathrm{m}^2\,\mathrm{s}^{-1}$ in water, $M = 731.5\,\mathrm{g\,mol}^{-1}$). R18 is an amphiphilic molecule with a polar head and an unpolar tail (see Fig. 1-7 and Tab. 1.2.). The dye molecules enter into the bilayer system and probe its mobility. Here, it is generally assumed that their diffusion is related to the lipid molecules, but an independent verification would be appropriate. There is no information available if R18 prefers the lipid-ordered or disordered phase.

Cholesterol has a molecular weight of $386.65\,\mathrm{g\,mol}^{-1}$ and a density of $1.07\,\mathrm{g\,cm}^{-3}$ at 20°C. The molecule length is 16 Å. The structure of cholesterol is depicted in Fig. 5-2.

5.2.2 Preparation of Surfactant Emulsions

Lipid and cholesterol were weighed with a micro balance, vortexed, heated and sonicated until the system became completely homogeneous. Then, *milliQ* water containing fluorescent dye was

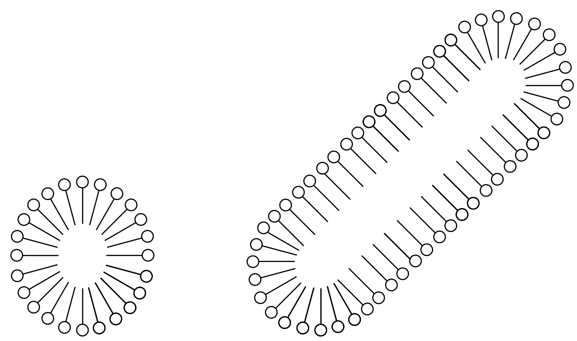

Figure 5-3. *Spherical and rod-like micelle*

added. The 20 wt $\%$ $C_{12}E_5$ and the 60 $\%$ solutions contained $10^{-8}\,\mathrm{M}$ R18, while the concentration in the 80 $\%$ solution was $10^{-7}\,\mathrm{M}$. The samples were then again heated to 60-70°C, sonificated, vortexed, and frozen (-80°C). These steps were repeated until the samples had become homogeneous gels. For the nominal 60 wt $\%$ emulsions, the fraction of $C_{12}E_5$ and cholesterol varied between 0.596 and 0.643. In the subsequent measurements of the 80 wt $\%$ emulsion the lipid fraction was kept constant at 0.80. The ratios of substances are listed in Table 5.3.4.

5.2.3 Micellar phase

In the micellar phase, the dye molecules enter the micelle and the observed diffusion will be that of the micelle. From standard diffusion theory, the expected diffusion coefficient D is related to the apparent hydrodynamic radius R_h of a sphere by Eq. 1.16. The diffusion coefficient of a typical micelle with a diameter of $5.0\,\mathrm{nm}$ is $D_{mic} = 86\,\mu\mathrm{m}^2\,\mathrm{s}^{-1}$ with $T = 293\,\mathrm{K}$, and the viscosity of water $\eta = 1\,\mathrm{mPa\,s}$. Corrections can be applied for elliptical or flexible geometries, but will be neglected for the further analysis.

5.2.4 Lamellar phase

In the lamellar phase, the lipid molecules form a bilayer structure. The membrane layer thickness is about double the length of a surfactant molecule $\delta = 2\,l_s$. The repeat distance of the lamellar structure is

$$X_{lam} = 2\,l_s/\phi_s \tag{5.1}$$

where ϕ_s is the volume fraction of the surfactant in the emulsion. Assuming $\phi_s = 0.6$ (0.8) and $l_s = 26$ Å, the repeat distance has a value of $X_{lam} = 8.7\,\mathrm{nm}$ ($6.50\,\mathrm{nm}$). The molecular order of the lamellar phase is maintained by van der Waals forces between the alkyl chains and hydrogen bonding forces between water molecules and the lipid headgroups [69].

The FCS measurements probe the bilayer dynamics in a volume of $\approx 0.5\,\mu m^3$, at a distance of $60\,\mu\mathrm{m}$ from the cover glass surface. Because this distance leaves room for about $7000 - 9000$

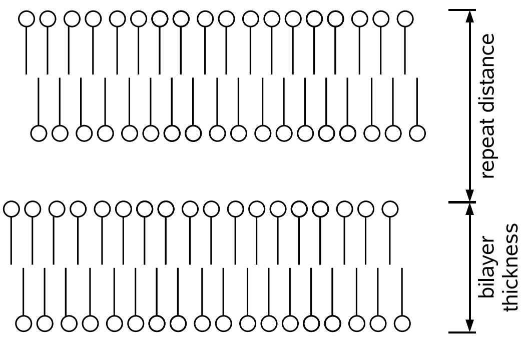

Figure 5-4. *Lamellar bilayer*

bilayers, it is assumed that surface effects are no longer important and the bilayers are randomly oriented. In addition, the horizontal alignment of the measurement position is varied across the sample drop. Remaining orientations of bilayers are averaged out by repeated measurements.
The molecular diffusion of each molecule is restricted to a single two-dimensional bilayer. The resulting propagation differs from that of free diffusion [12], but the observed signal represents an average over all possible orientations. Within the laser focus, which represents the sensitive volume, there is room for about 50 bilayers when they are arranged horizontally and 300 when they are arranged vertically.
Following the procedure of Galla and Sackmann for proteins and lipids in biological membranes [70], the diffusion of dye and lipid molecules are related to their molecular weights as

$$D_{dye} = D_{lipid} \left(\frac{M_{lipid}}{M_{dye}} \right)^{1/2} . \tag{5.2}$$

When $C_{12}E_5$ is compared to R18, the correction factor is 0.75.
Experimental data show that the shear viscosity in such binary or ternary systems can easily span orders of magnitude from $1\,\mathrm{mPas}$ to $10^5\,\mathrm{Pas}$ depending on concentration, pressure and temperature [71, 72, 73], but the effect of cholesterol on these parameters has not been studied so far.

5.3 FCS measurements

The experiments were carried out on the ConfoCor 2 microscope described in chapter 3.

5.3.1 Calibration

The focus parameters were calibrated with a $10^{-8}\,\mathrm{M}$ aqueous solution of Rhodamine 6G. The waist parameter determined in this way fell between $w_0 = 0.22 - 0.25\,\mu\mathrm{m}$, with an average of $\bar{w}_0 = 0.241\,\mu\mathrm{m}$. The structure parameter K was set to a fixed value of 6.0 corresponding to a

vertical focus radius of $z_0 = 1.3 - 1.5\,\mu\mathrm{m}$. The theoretical calculation using Rigler's and Mets' formula resulted in a slightly smaller value for w_{th} (cp. Tab. 1.3).
Adding $C_{12}E_5$ to pure water changes the refractive index of the sample solution. Hamano gives a linear equation to calculate the refractive index of a $C_{12}E_5$/water mixture [74] for a wavelength of $633\,\mathrm{nm}$ and a temperature of 20°C. According to this, the mixtures consisting of 20, 60, and 80 wt % $C_{12}E_5$ have refractive indices of $n' = 1.357$, 1.407, and 1.432.
The difference in optical refraction changes the size of the focused laser spot. Taking this into account, the focus waist is estimated in these three media to be $\hat{w}_0 = 0.236$, 0.228, and 0.224, respectively. These values were used in the evaluation of the correlation functions.
Two additional experimental adjustments were done to take the different refractive index into account. The microscope objective has a correction ring which can be used to adjust the refraction properties to varying cover glass thicknesses. Measurement series with 20 wt % and 50 wt % $C_{12}E_5$ emulsions showed the highest fluorescence count rates if the correction ring was in the maximum position of $0.18\,\mu\mathrm{m}$. In all following experiments the correction ring was kept in this position. Secondly, the length of the optical light path was reduced by setting the focus to a position $60 \pm 1\,\mu\mathrm{m}$ above the cover glass surface.

5.3.2 Autocorrelation model functions

The standard model proved to be unsatisfactory for the analysis of the diffusion measurements in the lamellar phase. This is related to the fact that the molecules are not free to diffuse in three dimensions, but are confined to the two-dimensional bilayers. The orientation of these bilayers with respect to the laser beam is random, so the measurements detect an orientational average. The orientation model from section 2.4, Eq. 2.16, is used as an alternative. The triplet term in Eq. 1.46 is added.

5.3.3 Experimental procedure

During the FCS experiments, the samples were placed in *Lab-Tek* 8-NUNC sample chambers. The bottom glass type is Borosilicate $\#1$ with a thickness between 0.13 and $0.16\,\mu\mathrm{m}$. The micellar emulsions are liquids and $4 - 5$ drops can be poured into the chambers. For the highly viscous gel emulsions ($60\,\%$ surfactant and more) a spatula must be used. The vessel was placed into the holder and covered with a non-transparent lid. The temperature control unit was set to 30°C. Table 5.3.4 lists the different samples that were used for this study, showing the different Molar ratios of cholesterol and $C_{12}E_5$.
Five subsequent correlation functions of 30 s each were averaged for one measurement. For each sample, 8 to 20 measurement runs were performed. The correlation functions were fitted to the

theoretical expressions of Eq. 1.40, Eq. 2.16 to determine the diffusion time and, using Eq. 1.42, the diffusion coefficients. Additionally, the cpm value was determined.

5.3.4 Results

Figure 5-5 shows a typical measurement result from the micellar phase, for a sample of 20 wt % $C_{12}E_5$. The experimental correlation data were fitted with the standard FCS function for free diffusion, Eq. 1.46. The best fit was obtained for the average parameters $\tau_d = 2800 \pm 800$, $N = 0.32 \pm 0.03$, $\tau_{trip} = 3\,\mu s$, $p = 0.14$. According to Eq. 1.42, this corresponds to a diffusion coefficient $D_{mic} = 5.4 \pm 2\,\mu\mathrm{m}^2/\mathrm{s}$. This value agrees with the expectation that it arises from the diffusion of prolate micelles. Their average size can be estimated using the corrected Stokes-Einstein expression for rod-like objects (Eq. 1.17). An axis ratio of 40:1 is presumed which was given in [14] resulting in $a = 180\,\mathrm{nm}$ for the long axis. For the given sample, this amounts to about 5000 micelles in the focal volume, of which on average $N = 0.32 \pm 0.03$ carry a fluorescent molecule.

In the lamellar phase two different ratios of $C_{12}E_5$ and water were examined, 60 wt % and 80 wt % surfactant. In this case, fluorophores diffuse independently within the lipid bilayers. The average number of molecules in the detection volume was 1.1 ± 0.3 for the low concentrated lamellar and 11 ± 6 for the high concentrated lamellar phase. The higher value for the 80 % lamellar phase was expected from the sample preparation.

Fitting these data with the standard model of unrestricted (3D) diffusion (Eq. 1.46), a significant deviation is found, as shown in Fig. 5-6. However, there is no systematic deviation if the experimental data is fit to the orientation model, Eq. 2.16. For the example shown in Fig. 5-6, the two models yield diffusion times of $\tau_d = 1.32 \pm 0.02$ (standard model) and $\tau_d = 0.901 \pm 0.008$ ms (orientation model), corresponding to diffusion constants D of 12.4 and $18.2\,\mu\mathrm{m}^2/\mathrm{s}$. While this analysis results in different values for the diffusion constants, the dependence on the cholesterol content does not change. The values of the measured diffusion constants are consistent with the assumption that the fluorescent R18 molecules were confined to the lipid bilayers. To check for a fraction of R18 in the water phase, the data was fit to a two-component model function. The results show no significant component with a high diffusion constant.

Figure 5-7 summarizes the change of the diffusion constant in the 60 % lamellar phase upon the addition of cholesterol. At low concentrations, no substantial effect is visible, but at a cholesterol content of about 8 %, a sudden reduction by ≈ 20 % occurs. A further increase of the cholesterol concentration yields an additional continuous reduction. The total decrease in the molecular mobility is ≈ 30 % for a cholesterol Molar ratio of 0.2.

The same measurements were also performed for the samples with the higher lipid contents. As shown in Fig. 5-8, the diffusion constant for low cholesterol content is approximately half of the

phase wt %	$C_{12}E_5$ mg	chol. mg	H_2O mg	ratio	lipid frac
mic 20	80	0	320	0	0.20
lam 60	243.5	48.8	162.6	0.211	0.643
	233.7	38.1	154.8	0.171	0.637
	255.3	38.3	170.7	0.158	0.632
	230.5	33.9	156.8	0.155	0.628
	243.2	31.3	163.0	0.135	0.627
	267.7	31.5	177.7	0.124	0.627
	255.6	25.3	168.9	0.104	0.624
	199.3	19.6	132.9	0.103	0.622
	250.0	21.4	167.5	0.090	0.618
	227.1	16.8	151.6	0.078	0.617
	219.7	12.1	145.8	0.058	0.614
	253.6	9.7	173.6	0.040	0.603
	229.4	8.2	153.6	0.038	0.607
	227.0	4.1	156.8	0.019	0.596
lam 80	153.8	3.05	40.7	0.021	0.794
	159.5	10.75	43.4	0.071	0.797
	159.0	15.7	44.6	0.104	0.797
	159.4	17.2	44.4	0.113	0.799
	155.8	20.5	45.0	0.138	0.797
	159.5	26.8	48.2	0.177	0.794

Table 5.1. *The table lists the amount of substances used in the microemulsions. The ratio value gives the Molar ratio of cholesterol versus $C_{12}E_5$. The lipid frac value denotes the fraction of $C_{12}E_5$ and cholesterol.*

corresponding data for the 60 % system. Again, a sudden decrease of the mobility is observed at a cholesterol content of ≈ 8 %, and a continuous decrease at higher concentrations.
The triplet fraction in the correlation amplitude is at 16 % on the average. The cpm value is between $11 - 14\,\mathrm{kHz}$ for low concentrations of cholesterol. Increasing the cholesterol concentration reduces the count rate by up to 50 % (Fig. 5-9). This may be a consequence of increased scattering in these samples. Visually observable was a small turbidity in the sample with a cholesterol ratio of 0.2 at room temperature. Alternatively, the count rate reduction may occur due to fluorescence quenching by the cholesterol.
In addition to the graphical representation of the diffusion data, Table 5.2 also gives the numerical values for the extreme cases. The last column of this table also shows the inferred diffusion constants of the lipid molecules, which were calculated from the measured diffusion constants by correcting for the different molecular weights using Eq. 5.2.

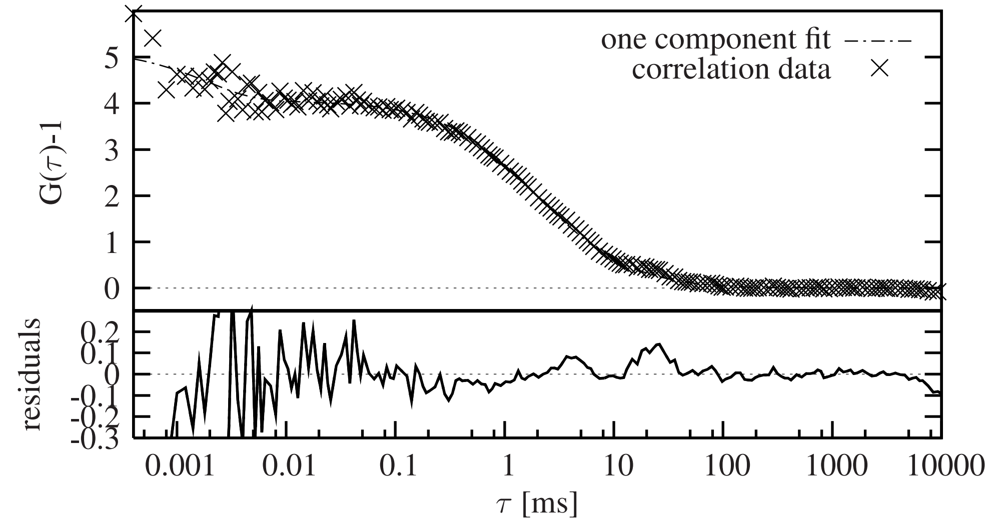

Figure 5-5. *FCS data for the micellar phase. The diffusion time in this example is* $\tau_d = 1.99 \pm 0.05$ *ms. The residuals show the absolute difference between fit and correlation data.*

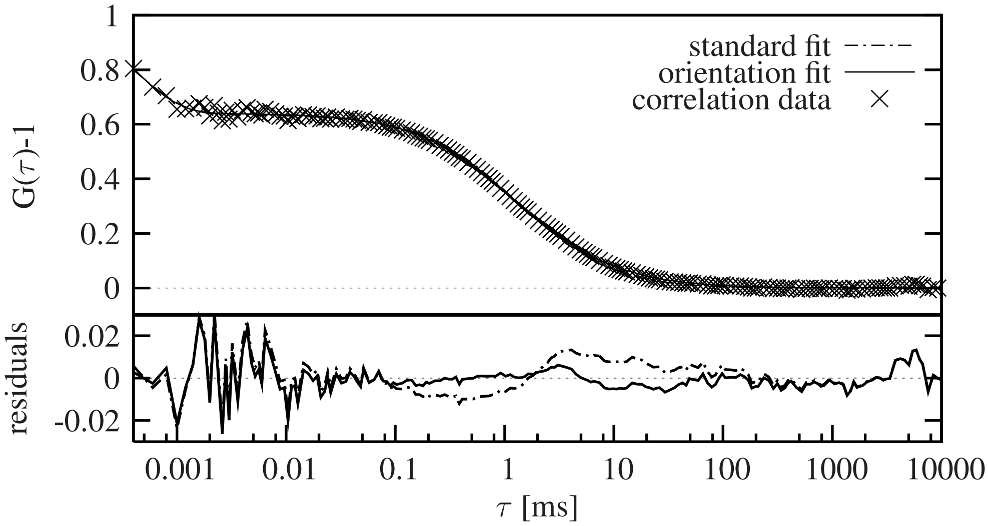

Figure 5-6. *Example for the FCS data from the surfactant/cholesterol/water emulsion. The experimental data (crosses) are compared to best fits using the standard (single-component) model (dash-dotted line) and to the orientation model (full line). The cholesterol to surfactant ratio was* 0.172*. The diffusion times are* $\tau_d = 1.32 \pm 0.02$ *ms (standard model) and* $\tau_d = 0.901 \pm 0.008$ *ms (orientation model).*

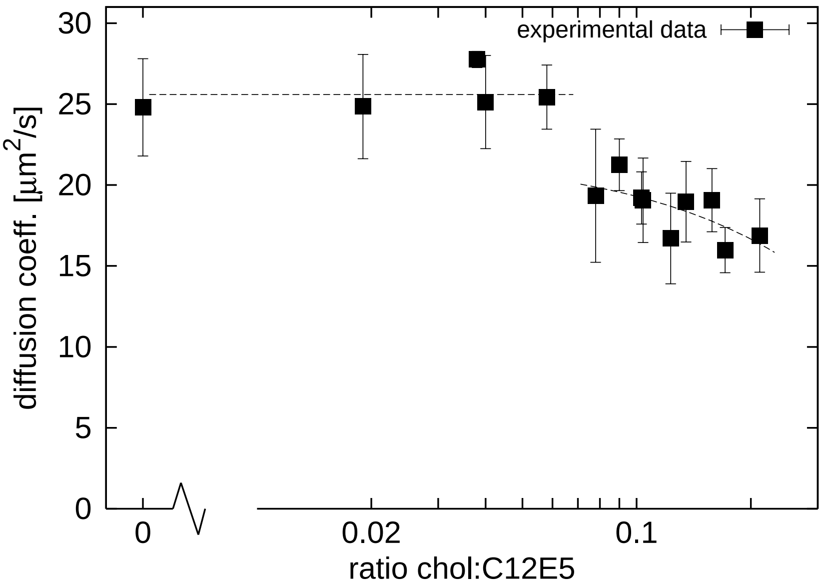

Figure 5-7. *Result for the diffusion coefficient D of R18 in the lamellar phase with* 60 *wt % surfactant. The Molar ratio of cholesterol to surfactant increases to the right. A reduction in molecular mobility is apparent at a ratio of* 0.08*. Error bars denote the standard deviation. Guidelines for the eyes are drawn dashed.*

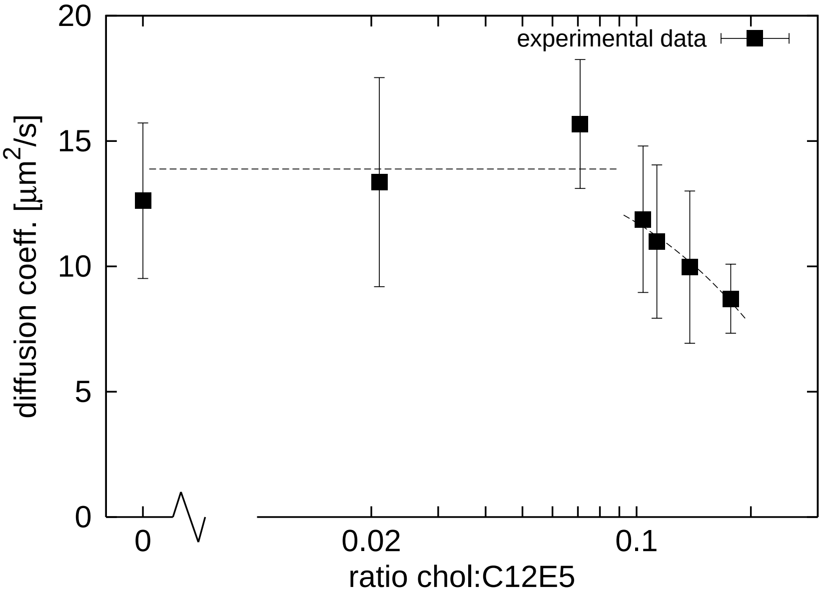

Figure 5-8. *Diffusion coefficients for the* 80 *wt % surfactant emulsion as a function of the cholesterol content.*

$C_{12}E_5$ wt %	phase	chol:$C_{12}E_5$ ratio	D(probe) [$\mu m^2/s$]	D(lipid)
20	micellar	–	5.4	–
60	lamellar	0	26	34
60	lamellar	≈ 0.2	16	21
80	lamellar	0	14	19
80	lamellar	≈ 0.2	9	12

Table 5.2. *Overview of diffusion coefficients D in $C_{12}E_5$/water/cholesterol emulsions determined from the orientation model.*

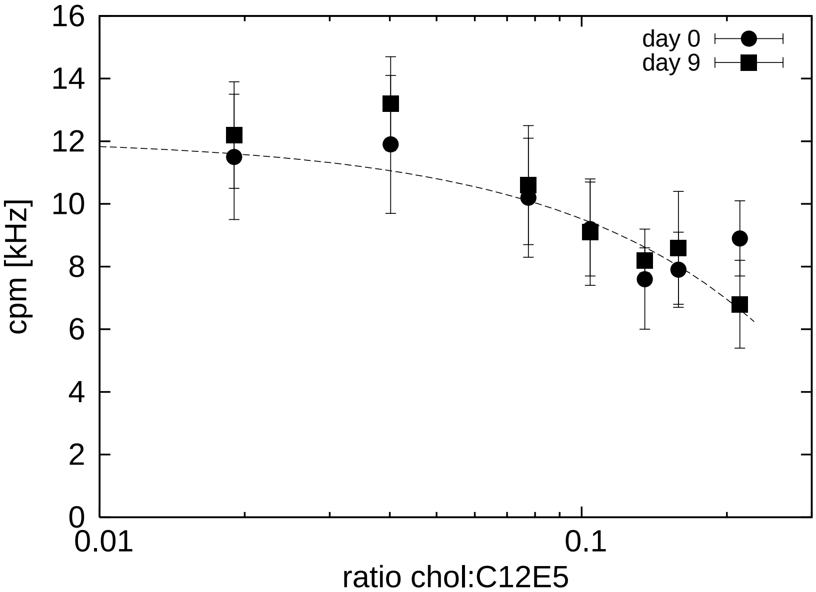

Figure 5-9. *Counts/molecule value (cpm) as a function of cholesterol content from the same sample on two different days. The brightness is reduced by increasing cholesterol content.*

5.4 Discussion

In the micellar phase (at 20 wt % lipid concentration), the observed correlation function is consistent with a model of freely diffusing micelles with a length of the order of $180\,\mathrm{nm}$ and a given axis ratio of 40:1. This size might be an overestimate, since the interaction between the micelles should result in a smaller diffusion constant than for micelles at low concentrations. Using this value, an upper limit of 0.14 as the total volume fraction of micelles in the solution can be given. Here, the volume reduction of the micellar solution of about 7 % was already taken into account. The lamellar system does not show free, three-dimensional diffusion. The correlation curves rather suggest that the Brownian motion of the probe molecules is restricted to the lamellar bilayers. The orientation model used for the analysis of the correlation function takes into account an average over many bilayer orientations and yields plausible fitting results.

The measured diffusion coefficients are generally higher than in DMPC membranes at equal temperature [75]. This is attributed to a higher rigidity of DMPC membranes. Regarding the influence of cholesterol, we can conclude that a cholesterol addition above a fraction of 0.08 in the $C_{12}E_5$ bilayer reduces the molecular mobility in the chosen surfactant/water emulsion. Because of the small observation volume in FCS, it is justified to claim that the structural changes of the molecular order take place on a scale below the focus diameter of $0.5\ \mu\mathrm{m}$. This reduction is a consequence of stronger molecular interaction induced by the presence of cholesterol molecules. Comparing this effect with observations in DLPC, the reduction of D by $30\ \%$ is slightly smaller than in DLPC where reductions by $\approx 50\ \%$ were observed at the same cholesterol fraction [76]. The reason might be a tighter packing of cholesterol molecules in double chain amphiphiles.

It is known that cholesterol interacts with alkyl chains. There are reports that cholesterol increases the fluidity in the center of DMPC membranes while decreasing it near the polar headgroup region [77]. A dependency on the length and asymmetry of the alkyl chains was also found [78]. In the present case, cholesterol has about 2/3 the length of a $C_{12}E_5$ molecule. Its rigid steroid ring is thought to restrain the free rotational motion of about 5-6 segments of the surrounding lipid molecules. Compared to biomembranes with lipids being asymmetric and longer, cholesterol may be incorporated differently. Nevertheless, the measurements show a similar influence of cholesterol on diffusion. Apparently, the fluorescent probes do not detect a higher fluidity of the inner alkyl groups, but rather the reduced mobility at the polar/unpolar interface.

Comparing the results to earlier measurements, it is striking, that in a majority of experimental studies cholesterol was found to decrease the diffusion coefficient in phosphatidylcholine membranes. Molecular Dynamics simulations support these findings. The structural influence of cholesterol seems to be independent of a possible phase transition though it might induce one in higher concentration. Thus, the structural influence of cholesterol on the molecular order in membranes seems to be a rather universal feature.

There are other effects in artificial membranes that possibly play a role in the correct description of molecular motion. It is conceivable that a wobbling or convective motion of the bilayers as a whole is important. As the lamellae are larger units – yet not immobile – this possibility must be taken into account. The time scale that these effects appear on should be much smaller than the one for diffusion. It was also reported that molecules diffusing in nanostructured liquids show effects of anomalous diffusion [79, 80, 81]. This can appear, for example, in the presence of coexisting gel and fluid phases. It can also be found in binary solutions of DMPC/DSPC, as recent studies using computer simulations and FCS experiments have indicated [82].

In conclusion, the results show a reduction of molecular mobility in a simple surfactant/water system induced by cholesterol at concentrations above $8\ \%$. The data helps to generalize the understanding of chemical interaction between cholesterol and lipids, and thus, the principle of the membrane order.

Chapter 6

Conclusions

In the foregoing chapters, the microscopic method Fluorescence Correlation Spectroscopy (FCS) was used to examine liquid flow and molecular diffusion in environments with different geometries. The small observation volume of the microscope was placed at defined positions inside a microchannel. The velocity of the water stream could be examined by observing fluorescent molecules in low concentration. The flow profile was successfully measured in a cross section of the channel. Beforehand, the three-dimensional velocity distribution had been computed with a simulation software based on the Finite Element Method (FEM). The experimental results are consistent with the expected (quasi-)parabolic velocity profiles.
Then, the problem of diffusion-limited mixing in microdevices was approached. A Y-shaped mixing channel was designed and produced. The FCS method proved to be capable of detecting relative concentration differences with good precision inside the channels. Again, CFD simulations and the experimental measurements provided consistent results. The accuracy of the concentration measurements was not ideal but can be enhanced by several means. The goal of characterizing the mixing properties of this specific channel was reached.
Despite the intended biochemical application, the experiments in microchannels proceed on a decidedly physical starting point. The microfluidic simulations and experiments contribute to develop accommodated reaction channels for future use. Further experiments on realizing an enzymatic reaction inside the channel have been taken up. It is challenging to find the right conditions for reproducible reaction kinetics. Besides the physical point of view, questions of surface chemistry and other disciplines have to be taken into account as well.
In the biological sciences, there is a demand to examine processes in eukaryotic cells. These processes are often based on mechanisms with only few molecules involved. This requires to build an optical system with a high spatial resolution and the sensitivity to observe single molecule motion in a natural surrounding. By means of image analysis it could be demonstrated how the diffusion coefficient of a microsphere can be determined from fluorescent images. The principle can be transferred to single molecule detection. Provided that the sensitivity and frame rates are

chosen adequately, the diffusion coefficient can be determined precisely in a shorter time than in FCS. It is desirable to extract the maximum information content from the fluorescent images. Different techniques can be realized for the purpose of tracking a molecule trajectory. There is a fundamental difference between the software and the hardware approach. The software solution is based on image recognition of single fluorescent molecules. As long as the real time data are two-dimensional, this method is restricted to the plane. It has the advantage though, that many molecules can be tracked at the same time.

From the hardware side, there are two main ways to establish a tracking system. The first approach relies on mechanical tracking by moving the support of the sample. The second method needs control of the laser beam by fast re-adjustment of two mirrors. The principle is availed in laser scanning microscopy, yet with a fixed scanning scheme. Both ways share the fact that the molecule remains in the region of interest for as long as possible. The advantage is that the molecule is almost constantly excited during observation. This enables to measure real single molecules parameters. The disadvantage of a tracking system is, that it must be realized in three dimensions. This is a challenge for the optical and the mechanical detection system, which was pointed out in section 4.4.1. A mechanical tracking system can only track one molecule independently at a time. The use of quantum dots instead of fluorescent molecules offers a promising way to address the problem of photo degradation.

The chapter about surfactant/water emulsions can be regarded separately from the experiments in microstructures because it was an independent project. Yet, the experimental method and the interpretation of the data are based on the preceding fundamental facts. In the context of molecular motion, it is regarded as a straight forward way to focus on a physical property when going to smaller scales. The chapter deals with diffusion in systems forming nanostructures by self-assembly. It is shown that cholesterol as a third component has a structural influence on the molecular order. The bilayer structure leads to a behavior that can be described by two-dimensional diffusion in planes rather than free diffusion in solution. Additionally, a modified model equation for FCS was found that leads to better results for the corresponding diffusion coefficients. It will be useful in further studies of randomly oriented lamellar media.

In environments that exhibit an intrinsic molecular structure, additional phenomena come into effect. Perturbed motion of molecules is likely to be observed in material that contain an anisotropic molecular order. Especially, the effects of anomalous diffusion have gained interest recently. It is largely unknown to what extend these effects play a role in intracellular mechanisms. Fluorescence Recovery After Photobleaching (FRAP) has often been used to examine these phenomena. With FCS, anomalous diffusion can be observed e. g., by variation of the focus diameter [2].

Recently, new developments have lowered the resolution of optical microscopes down to $20\,\mathrm{nm}$ [1, 83]. The microscope makes use of an method named STED (STimulated Emission Depletion).

Higher resolution offers a way to depict cellular structures which were unaccessible otherwise. Other researchers have taken an effort to increase the focal volume. This allows to measure even lower concentration down to the pM range [84]. Depending on the application, both concepts expand the possibilites of fluorescence techniques. Apart from these advancements, it is still rewarding to continue working on methods for Single Molecule Detection and analysis.

Appendix A

List of manufacturers

- Chemicals
  octadecyl Rhodamine B (R18) – *Invitrogen* (Carlsbad, California)
  $C_{12}E_5$ – *SigmaAldrich* (St. Louis, Missouri)

- Detectors and photon counting
  beam analyzer LBA-7xxPC – *Spiricon* (Logan, Utah)
  CCD camera Cohu 4812 – *Cohu* (San Diego, California)
  correlator ALV-5000 – *ALV GmbH* (Langen, Germany)
  CMOS camera LogLux i5 CL – *Kamerawerk Dresden* (Dresden, Germany)
  multi channel scaler PMS 300 – *Becker und Hickl GmbH* (Berlin, Germany)
  photo diode SPCM-AQR 14 – *PerkinElmer* (Kirkland, Canada)
  photo diode SPCM-AQR 13 – *PerkinElmer* (Kirkland, Canada)
  frame grabber mvTITAN-CL – *MatrixVision* (Oppenweiler, Germany)

- Fluorimeter
  FluoroMax 2 – *Jobin Yvon Instruments S.A. Inc.* (New Jersey)

- Lasers
  Ar-Ion BeamLok 2080 – *Spectra Physics* (Mountain View, California)
  HeNe LGK 7786 P – *Lasos* (Jena, Germany)

- Liquid handling
  Gastight 1750 syringes – *Hamilton* (Reno, Nevada)
  syringe pump SP260p – *World Precision Instruments* (Sarasota, Florida)

- Mechanical stages and plates
  tubus system parts – *Linos* (Göttingen, Germany)
  linear stages – *Newport* (Irvine, California)

- Microscopes
  ConfoCor 2 – *Carl Zeiss* (Jena, Germany)

- Microfluidics
  photo masks – *GeSIM* (Großerkmannsdorf, Germany)
  etching, bonding and microfluidic connection – *Fraunhofer BioMOS* (Sankt Augustin, Germany)

- Objectives
  C-Apochromat $63\times$ 1.2 W – *Carl Zeiss* (Jena, Germany)
  Plan Neofluar $63\times$ 1.4 Oil – *Carl Zeiss* (Jena, Germany)
  Achromat $40\times$ 1.2 W – *Carl Zeiss* (Jena, Germany)

- Optical filters, lenses, dichroic mirrors
  dichroic mirror 540DRLPO2 – *Omega Optical* (Brattleboro, Vermont)
  filters – *AHF Analysetechnik* (Tübingen , Germany)
  neutral wedges – *Linos* (Göttingen, Germany)
  tubus lens $f = 164.5\,\mathrm{mm}$ – *Carl Zeiss* (Jena, Germany)

- Oscilloscope
  Wavemaster 6000 – *LeCroy* (Chestnut Ridge, New York)

- Positioning
  PZT sensor/servo module controller E-509.C3A – *PI Physik Instrumente GmbH & Co. KG* (Karlsruhe , Germany)
  piezo amplifier module E-503.00 – *PI Physik Instrumente GmbH & Co. KG* (Karlsruhe, Germany)
  display module E-516.i3 – *PI Physik Instrumente GmbH & Co. KG* (Karlsruhe, Germany)
  PIFOC P-721 focus nanopositioner – *PI Physik Instrumente GmbH & Co. KG* (Karlsruhe, Germany)

- Software
  GAMBIT (grid model) – Fluent Inc. (Lebanon, New Hampshire)
  FLUENT (CFD simulation) – Fluent Inc. (Lebanon, New Hampshire)
  MPlayer version 1.0rc1-4.0.2 – MPlayer Team, *http://www.mplayerhq.hu*

Appendix B

Publications and conference contributions

1. Pieper, Thorsten ; Svetlana Markova ; Masataka Kinjo ; Dieter Suter ; Effect of cholesterol on diffusion in surfactant bilayers ; submitted ; 2007

2. Pieper, Thorsten ; Svetlana Markova ; Masataka Kinjo ; Dieter Suter ; Comparative study on the stabilizing effect of cholesterol on lamellar bilayers ; poster award ; EABS & BSJ 2006 Naha (Japan) ; 2006

3. Pieper, Thorsten ; Benjamin Greiner ; Harald P. Mathis ; From 2D to 3D Molecule Tracking ; poster presentation ; 4th International Workshop on Scanning Probe Microscopy Berlin ; 2003

4. Pieper, Thorsten ; Benjamin Greiner ; Harald P. Mathis ; 3D Molecule Tracking ; poster presentation ; Bunsen Tagung Kiel ; 2003

5. Pieper, Thorsten ; Benjamin Greiner ; Harald P. Mathis ; 2D Molecule Tracking ; short talk ; annual DPG conference Dresden ; 2003

6. Mathis, Harald P. ; Benjamin Greiner ; Thorsten Pieper ; Spatially Resolved Realtime Single Molecule Detection for Protein Dynamic Investigations ; poster presentation ; 295. WE Heraeus Seminar Bad Honnef ; 2003

Selbständigkeitserklärung

Hiermit erkläre ich, die vorliegende Dissertation selbstständig und ohne unerlaubte fremde Hilfe angefertigt zu haben und mich dabei keiner anderen als der von mir ausdrücklich bezeichneten Quellen und Hilfen bedient habe. Ebenfalls sind alle von anderen Personen bereitgestellten Materialien oder erbrachten Dienstleistungen als solche gekennzeichnet. Die Dissertation wurde in der jetzigen oder einer ähnlichen Form noch an keiner anderen Hochschule eingereicht und hat noch keinen sonstigen Prüfungszwecken gedient.

Bonn, im Juni 2007

Thorsten Pieper

Bibliography

[1] Stefan W. Hell. Towards fluorescence nanoscopy. *Nature biotechnology*, 21:1347–1355, 2003.

[2] Akiko Masuda, Kiminori Ushida, and Takayuki Okamoto. New Fluorescence Correlation Spectroscopy Enabling Direct Observation of Spatiotemporal Dependence of Diffusion Constants as an Evidence of Anomalous Transport in Extracellular Matrices. *Biophys. J.*, 88: 3584–3591, 2006.

[3] Marcel Leutenegger, Michael Goesch, Alexandre Perentes, Patrik Hoffmann, Olivier J.F. Martin, and Theo Lasser. Confining the sampling volume for fluorescence correlation spectroscopy using a sub-wavelength sized aperture. *Optics Express*, 14(2):956–969, 2006.

[4] Gi Hun Seong, Jinseok Heo, and Richard M. Crooks. Measurement of enzyme kinetics using a continuous-flow microfluidic system. *Analytical Chemistry*, 75:3161–3167, 2003.

[5] L.D. Landau and E.M. Lifshitz. *Hydrodynamik, Lehrbuch der Theoretischen Physik*, volume VI. Akademie Verlag, Berlin, 5th edition, 1991.

[6] Brian J. Ford. Brownian movement in clarkia pollen: a reprise of the first observations, 1992.

[7] Nam-Trung Nguyen and Steven T. Wereley. *Fundamentals and Applications of Microfluidics*, volume 1. Fluidic devices. Artech House, Inc., 685 Canton Street, Norwood, MA 02062, 2002.

[8] L.D. Landau and E.M. Lifshitz. *Statistical Physics Part 1, Course of Theoretical Physics*, volume 5. Butterworth Heinemann, Oxford, 3rd edition, 1980.

[9] Y. Chen, Joachim D. Müller, Peter T.C. So, and Enrico Gratton. The Photon Counting Histogram in Fluorescence Fluctuation Spectroscopy. *Biophys. J.*, 77:553–567, 1999.

[10] I.N. Bronstein and K.A. Semendjajew. *Taschenbuch der Mathematik*. Verlag Harri Deutsch, Thun und Frankfurt a. M., 24th edition, 1989.

[11] Gerd Wedler. *Lehrbuch der Physikalischen Chemie*. VCH Verlagsgesellschaft mbH, Weinheim, 3rd edition, 1987.

[12] John Crank. *The Mathematics of Diffusion*. Oxford University Press, Second edition, 1975.

[13] M. Ehrenberg and R. Rigler. Rotational brownian motion and fluorescence intensity fluctuations. *Chemical Physics*, 4:390–401, 1974.

[14] Mikael Jonströmer, Bengt Jönsson, and Björn Lindman. Self-Diffusion in Nonionic Surfactant-Water Systems. *J. Phys. C*, 95:3293–3300, 1991.

[15] Howard C. Berg. *Random Walks in Biology*. Princeton University Press, Expanded edition, 1993.

[16] Peter W. Atkins. *Physikalische Chemie*. Wiley-VCH Verlag GmbH, Weinheim, 3rd corrected edition, 2001.

[17] Ch. Zander, J. Enderlein, and R.A. Keller, editors. *Single Molecule Detection in Solution, Methods and Applications*. Wiley VCH, Berlin, 2002.

[18] Gordon M. Barrow. *Physikalische Chemie*, volume 3. Bohmann-Verlag, Heidelberg, Wien, 2nd edition, 1972.

[19] Joseph R. Lakowicz. *Topics in Fluorescence Spectroscopy*. Plenum Press, New York, 1991.

[20] Joseph W. Goodman. *Statistical Optics*. Wiley Classics Library Edition, 2000.

[21] C. Eggeling, J. Widengren, R. Rigler, and C.A.M. Seidel. *Applied Fluorescence in Chemistry, Biology and Medicine*, chapter Photostability of Fluorescent Dyes for Single-Molecule Spectroscopy: Mechanisms and Experimental Methods for Estimating Photobleaching in Aqueous Solution, pages 193–240. Springer, Berlin Heidelberg, 1999.

[22] Jerker Widengren, Uelo Mets, and Rudolf Rigler. Fluorescence correlation spectroscopy of triplet states in solution: A theoretical and experimental study. *J. of Phys. Chem.*, 1995.

[23] Christian Eggeling, Andreas Volkmer, and Claus A.M. Seidel. Molecular Photobleaching Kinetics of Rhodamine 6G by One- and Two-Photon Induced Confocal Fluorescence Microscopy. *ChemPhysChem*, 6:791–804, 2005.

[24] Elliot L. Elson. Fluorescence Correlation Spectroscopy. I. Conceptual Basis and Theory. *Biopolymers*, 13:1–27, 1974.

[25] Douglas Magde and Elliot L. Elson. Fluorescence Correlation Spectroscopy. II. An Experimental Realization. *Biopolymers*, 13:29–61, 1974.

[26] R. Rigler, U. Mets, J. Widengren, and P. Kask. Fluorescence correlation spectroscopy with high count rate and low background: analysis of translational diffusion. *Eur. Biophys. J.*, 22: 169–175, 1993.

[27] Samuel T. Hess and Watt W. Webb. Focal Volume Optics and Experimental Artifacts in Confocal Fluorescence Correlation Spectroscopy. *Biophys. J.*, 83:2317, 2002.

[28] J. Enderlein. Art and artefacts of fluorescence correlation spectroscopy. *Curr. Pharm. Biotechnology*, 5:155–161, 2004.

[29] Norbert Wiener. *Generalized Harmonic Analysis*. Massachusetts Institute of Technology, 1930.

[30] D.E. Koppel. Statistical accuracy in fluorescence correlation spectroscopy. *Physical Review A*, 10:1938–1945, 1974.

[31] T. Wohland, R. Rigler, and H. Vogel. The standard deviation in fluorescence correlation spectroscopy. *Biophys. J.*, 80:2987–2999, 2001.

[32] Peet Kask, Rolf Günther, and Peter Axhausen. Statistical accuracy in fluorescence fluctuation experiments. *Eur. Biophys. J.*, 25:163–169, 1997.

[33] Ulrich Meseth, Thorsten Wohland, Rudolf Rigler, and Horst Vogel. Resolution of fluorescence correlation measurements. *Biophys. J.*, 78:1619–1631, 1999.

[34] Saveez Saffarian and Elliot L. Elson. Statistical analysis of fluorescence correlation spectroscopy: The standard deviation and bias. *Biophys. J.*, 84:2030–2042, 2003.

[35] Hong Qian. On the statistics of fluorescence correlation spectroscopy. *Biophysical Chemistry*, 38:49–57, 1990.

[36] Hong Qian and Elliot L. Elson. Distribution of molecular aggregation by analysis of fluctuation moments. *Proc. Natl. Acad. Sci. USA*, 87:5479–5483, 1990.

[37] Klaus Schätzel. New concepts in correlator design. *Inst. Phys. Conf. Ser.*, 77(session 4), 1985.

[38] Goro Nishimura and Masataka Kinjo. Systematic error in fluorescence correlation measurements identified by a simple saturation model of fluorescence. *Analytical Chemistry*, 76(7): 1963–1970, 2004.

[39] Ch. Zander, J. Enderlein, and R.A. Keller, editors. *Single Molecule Detection in Solution, Methods and Applications*, chapter Conceptual Basis of Fluorescence Correlation Spectroscopy and Related Techniques as Tools in Bioscience, pages 69–119. Wiley VCH, Berlin, 2002.

[40] Michael Goesch, Hans Blom, Johan Holm, Toni Heino, and Rudolf Rigler. Hydrodynamic Flow Profiling in Microchannel Structures by Single Molecule Fluorescence Spectroscopy. *Anal. Chem.*, 72:3260–3265, 2000.

[41] W.H. Press. *Numerical Recipes*. Cambridge University Press.

[42] Harald P. Mathis. *Beugungsbegrenzte und raum-zeitlich aufgelöste Einzelmoleküldetektion von DNA und tRNA in Siliziummikrostrukturen*. PhD thesis, Universität Jena, Jena, 2000.

[43] Matthias Weiss, Hitoshi Hashimoto, and Tommy Nilsson. Anomalous Protein Diffusion in Living Cells as Seen by Fluorescence Correlation Spectroscopy. *J. Chem. Phys.*, 84:4043–4052, 2003.

[44] M. Minsky. Memoir on inventing the confocal scanning microscope. *Scanning*, 10:128–138, 1988.

[45] Volker Inden. Ein Verfahren zur Nanopositionierung von Partikeln in Mikrosystemen. Master's thesis, Rheinische Fachhochschule Köln, 2005.

[46] Th. Schmidt, G.J. Schütz, W. Baumgartner, H.J. Gruber, and H. Schindler. Imaging of single molecule diffusion. *Proc. Natl. Acad. Sci. USA*, 93:2926–2929, 1996.

[47] Kai Lueghausen. Definition einer Schnittstelle zur Datenerfassung in der Moleküldetektion. Master's thesis, Rheinische Fachhochschule Köln, 2005.

[48] author not specified. Applications Manual Zeiss LSM 510 – ConfoCor2, 05 2001.

[49] Ken B. Greiner, Manish Deshpande, John R. Gilbert, Rustem F. Ismagilov, Abraham D. Stroock, and George M. Whitesides. Design Analysis and 3D Measurement of Diffusive Broadening in a Y-mixer.

[50] Andrea Wagner. Simulationen im Mikrokosmos mit der CFD-Software Fluent. Technical report, Fraunhofer SCAI, 2005.

[51] Xiao-Hong Xu and Edward S. Yeung. Direct measurement of single-molecule diffusion and photodecomposition in free solution. *Science*, 275:1106–1109, 1997.

[52] Lucas P. Watkins and Haw Yang. Information Bounds and Optimal Analysis of Dynamic Single Molecule Measurements. *Biophys. J.*, 86:4015–4029, 2004.

[53] Benjamin Greiner. *Die Einzelmolekülverteilung in Fluoreszenz-Fluktuationsexperimenten*. PhD thesis, Universität Ulm, 2007.

[54] V. Hessel, S. Hardt, H. Löwe, and F. Schönfeld. Laminar mixing in different interdigital micromixers: I. Experimental characterization. *AIChE*, 49:566–577, 2003.

[55] S. Hardt and F. Schönfeld. Laminar mixing in different interdigital micromixers: II. Numerical simulations. *AIChE*, 49:578, 2003.

[56] Abraham D. Stroock, Stephan K.W. Dertinger, Armand Ajdari, Igor Mezić, Howard A. Stone, and George M. Whitesides. Chaotic mixer for microchannels. *Science*, 295:647–651, 2002.

[57] D. Lumma, A. Best, A. Gansen, F. Feuillebois, J. O. Rädler, and O. I. Vinogradova. Flow profile near a wall measured by double-focus fluorescence cross-correlation. *Physical Review E*, 67:056313, 2003.

[58] C. D. Meinhart, S. T. Wereley, and J. G. Santiago. PIV measurements of a microchannel flow. *Experiments in Fluids*, 27:414–419, 1999.

[59] H P Mathis, G Kalusche, B Wagner, and J S McCaskill. Steps towards spatially resolved single molecule detection in solution. *Bioimaging*, 5:116–128, 1997.

[60] A. Pralle, M. Prummer, E.-L. Florin, E.H.K. Stelzer, and J.K.H. Hörber. Three-dimensional high-resolution particle tracking for optical tweezers by forward scattered light. *MICROSCOPY RESEARCH AND TECHNIQUE*, 44:378–386, 1999.

[61] Kana Mizutani, Kazuhiro Oiwa, Hitoshi Sakakibara, Tomoko Masaike, and Takayuki Nishizaka. Three-dimensional imaging of microtubule sliding generated by molecular motors ; Poster presentation. *EABS&BSJ 2006 conference in Naha (Japan)*, 2006.

[62] Gerald W. Feigenson and Jeffrey T. Buboltz. Ternary Phase Diagram of Dipalmitoyl-PC/Dilauroyl-PC/Cholesterol: Nanoscopic Domain Formation Driven by Cholesterol. *Biophys. J.*, 80:2775–2788, 2001.

[63] Mark Tarshish, Michael Salman, and Shlomo Rottem. Cholesterol is required for the fusion of single unilamellar vesicles with Mycoplasma capricolum. *Biophys. J.*, 64:709–715, 1993.

[64] Sophie Raffy and Justin Teissie. Control of Lipid Membrane Stability by Cholesterol Content. *Biophys. J.*, 76:2072–2080, 2004.

[65] D. John Mitchell, Gordon J.T. Tiddy, Loraine Waring, Theresa Bostock, and Malcolm P. McDonald. Phase behaviour of polyoxyethylene surfactants with water. Mesophase structures and partial miscibility (cloud points). *J. Chem. Soc., Faraday Trans. 1*, 79:975–1000, 1983.

[66] E.Z. Radlinska, T. Gulik-Krzywicki, F. Lafuma, D. Langevin, W. Urbach, C.E. Williams, and R. Ober. Modification of the Lamellar Phase in $C_{12}E_5$/Water System by a Random Hydrophilic-Hydrophobic Polyelectrolyte. *Journal of Physics II France*, 7:1393–1416, 1997.

[67] S.K. Ghosh, S. Komura, J. Matsuba, H. Seto, T. Takeda, and M. Hikosaka. Structural changes and interaction parameters in amphiphilic system $C_{12}E_5$/water/*n*-octane. *Progr Colloid Polym Science*, 106:91–97, 1997.

[68] Paul D.T. Huibers, Victor S. Lobanov, Alan R. Katritzky, Dinah O. Shah, and Mati Karelson. Prediction of Critical Micelle Concentration Using a Quantitative Structure-Property Relationship Approach. 1. Nonionic Surfactants. *Langmuir*, 12:1462–1470, 1996.

[69] C. Stubenrauch, S. Burauer, R. Strey, and C. Schmidt. A new approach to lamellar phases (L_α) in water - non-ionic surfactant systems. *Liquid Crystals*, 31:39–53, 2004.

[70] H.J. Galla, W. Hartmann, U. Theilen, and E. Sackmann. On Two-Dimensional Passive Random Walk in Lipid Bilayers and Fluid Pathways in Biomembranes. *J. Membrane Biology*, 48:215–236, 1979.

[71] S. Paasch, F. Schambil, and M.J. Schwuger. Rheological Properties of Lamellar Lyotropic Liquid. *Langmuir*, 5:1344–1346, 1989.

[72] G. D'Arrigo and G. Briganti. Viscoelastic behavior of aqueous solutions of a polyoxyethylene-nonionic-amphiphile surfactant. *Physical Review E*, 58:713–723, Jul 1998. doi: 10.1103/PhysRevE.58.713.

[73] J. Schulte, S. Enders, and K. Quitzsch. Rheological studies of aqueous alkylpolyglucoside surfactant solutions. *Colloid and Polym Sci*, 277:827–836, 1999.

[74] K. Hamano, N. Kuwahara, T. Koyama, and S. Harada. Critical behaviors in the two-phase region of a micellar solution. *Physical Review A*, 32:3168–3171, 1985.

[75] Greger Orädd, Göran Lindblom, and Philip W Westerman. Lateral diffusion of cholesterol and dimyristoylphosphatidylcholine in a lipid bilayer measured by pulsed field gradient NMR spectroscopy. *Biophys. J.*, 83:2702–2704, 2002.

[76] Jonas Korlach, Petra Schwille, Watt W. Webb, and Gerald W. Feigenson. Characterization of lipid bilayer phases by confocal microscopy and fluorescence correlation spectroscopy. *PNAS*, 96:8461–8466, 1999.

[77] Jun-Jie Yin and Witold K. Subczynski. Effects of Lutein and Cholesterol on Alkyl Chain Bending in Lipid Bilayers: A Pulse Electron Spin Resonance Spin Labeling Study. *Biophys. J.*, 71:832–839, 1996.

[78] Lubin Chena, Michael L. Johnson, and Rodney L. Biltonen. A Macroscopic Description of Lipid Bilayer Phase Transitions of Mixed-Chain Phosphatidylcholines: Chain-Length and Chain-Asymmetry Dependence. *Biophys. J.*, 80:254–270, 2001.

[79] G.J. Schütz, H. Schindler, and Th. Schmidt. Single-Molecule Microscopy On Model Membranes Reveals Anomalous Diffusion. *Biophys. J.*, 73:1073–1080, 1997.

[80] Petra Schwille, Jonas Korlach, and Watt W. Webb. Fluorescence Correlation Spectroscopy With Single-Molecule Sensitivity on Cell and Model Membranes. *Cytometry*, 36:176–182, 1999.

[81] Arne Gennerich and Detlev Schild. Anisotropic Diffusion in Mitral Cell Dendrites Revealed by Fluorescence Correlation Spectroscopy. *Biophys. J.*, 83:510–522, 2002.

[82] Agnieszka E. Hac, Heiko M. Seeger, Matthias Fidorra, and Thomas Heimburg. Diffusion in Two-Component Lipid Membranes - A Fluorescence Correlation Spectroscopy and Monte Carlo Simulation Study. *Biophys. J.*, 88:317–333, 2005.

[83] Lars Kastrup, Hans Blom, Christian Eggeling, and Stefan W. Hell. Fluorescence Fluctuation Spectroscopy in Subdiffraction Focal Volumes. *Physical Review Letters*, 94:178104, 2005.

[84] Tsuyoshi Sonehara, Takashi Anazawa, and Kenko Uchida. Improvement of Biomolecule Quantification Precision and Use of a Single-Element Aspheric Objective Lens in Fluorescence Correlation Spectroscopy. *Anal. Chem.*, 78:8395–8405, 2006.